Optimal Wavefronts and Subwavelength Structures: Computer-Aided Design for Optics and Acoustics

by

Yoon Kyung (Eunnie) Lee

Submitted to the Department of Mechanical Engineering
in partial fulfillment of the requirements for the degree of

Doctor of Philosophy

at the

MASSACHUSETTS INSTITUTE OF TECHNOLOGY

June 2017

Signature redacted

Author .....
Department of Mechanical Engineering
May 4, 2017

Signature redacted

Certified by .....
Nicholas X. Fang
Associate Professor of Mechanical Engineering
Thesis Supervisor

Signature redacted

Certified by .....
Steven G. Johnson
Professor of Applied Mathematics
Thesis Supervisor

Signature redacted

Accepted by .....
Rohan Abeyaratne
Chairman, Department Committee on Graduate Theses

Optimal Wavefronts and Subwavelength Structures: Computer-Aided Design for Optics and Acoustics

by

Yoon Kyung (Eunnie) Lee

Submitted to the Department of Mechanical Engineering
on May 4, 2017, in partial fulfillment of the
requirements for the degree of
Doctor of Philosophy

Abstract

The aim of the research presented in this thesis is to design optimal wavefronts and subwavelength structures that enhance mechanical effects on the nanoscale, focusing on three types of devices: holographic optical tweezers, broadband solar absorbers, and acoustic waveguides. Much of the work presented is obtained using open source software tools.

Advances in spatial wave modulation and nanomaterial fabrication technologies have created many new degrees of freedom for engineering wave-matter interaction. When exploring so many parameters, a large number of full-wave scattering problems must be solved efficiently – calling for a more targeted design approach. We address this challenge by offering computer-automated design frameworks that effectively combine the best computational software developed in physics, numerical analysis, and inverse design.

Part I presents computational inverse design methods for structured illumination in holographic optical tweezers. Wave optimization is highly nonconvex by nature, and possesses many local optima due to interference and resonance. By combining a compact Bessel basis and a fast boundary element method, we achieve a 20-fold enhancement in torque per intensity, over a standard circular-polarized illumination, on a model plasmonic nanoparticle.

Part II presents mode analysis and numerical parameter-testing strategies for periodic subwavelength structures in optics and acoustics. We first summarize the design and experimental characterization results of a photonic crystal solar absorber with wide-angle spectral selectivity. Next, we discuss a multiscale acoustic model of a phononic crystal with strong spatial dispersion.

We are optimistic that our computational frameworks for wavefronts and subwavelength structures can be generalized and applied to other design problems, such as metamaterials, 3d manufacturing, and 3d imaging.

Thesis Supervisor: Nicholas X. Fang
Title: Associate Professor of Mechanical Engineering

Thesis Supervisor: Steven G. Johnson
Title: Professor of Applied Mathematics

Publications

1. Y. E. Lee, O. D. Miller, M. T. H. Reid, S. G. Johnson and N. X. Fang, "Computational Inverse Design of Non-Intuitive Illumination Patterns to Maximize Optical Force or Torque," Optics Express, Vol. 25(6): 6757 (2017)

2. N. Nemati, Y. E. Lee, D. Lafarge, A. Duclos, and N. X. Fang, "Nonlocal Dynamics of Dissipative Phononic Fluids," Phys. Rev. B., Accepted for publication on 10 May 2017

3. M. T. Klug, N. D. Courchesne, Y. E. Lee, J. Qi, D. S. Yun, N. Heldman, P. T. Hammond, N. X. Fang, and A. M. Belcher, "Mediated Growth of Zincous Shells on Gold Nanoparticles by Free-Base Amino Acids," under review (2017)

4. J. Y. Lu, S. H. Nam, K. Wilke, A. Raza, Y. E. Lee, A. AlGhaferi, N. X. Fang, and T. Zhang, "Localized Surface Plasmon-Enhanced Ultrathin Film Broadband Nanoporous Absorbers," Advanced Optical Materials, Vol. 4 (2016)

5. Y. E. Lee, K. H. Fung, D. Jin, and N. X. Fang, "Optical torque from enhanced scattering by multipolar plasmonic resonance," Nanophotonics, Vol. 3(6): 343-440 (2014)

6. J. B. Chou, Y. X. Yeng, Y. E. Lee, A. Lenert, V. Rinnerbauer, I. Celanovic, M. Soljačić, N. X. Fang, E. N. Wang, and S.-G. Kim, "Enabling Ideal Selective Solar Absorption with 2D Metallic Dielectric Photonic Crystals," Advanced Materials, Vol. 26 (2014)

Acknowledgments

Working with my two brilliant and considerate advisors, Prof. Nicholas Xuanlai Fang and Prof. Steven Glenn Johnson, has been an empowering and humbling experience. Nick and Steven are two of the most happy, hardworking, and awe-inspiring human beings I've ever met. I'm very thankful for the time and attention they have invested in me, guiding my intellectual energy to "propagate" far out of my comfort zone and "resonate" with exciting problems, until I could finally solve them.

When I came to MIT in 2011, I was broadly interested in the physics of light, sound, and composite materials. So I met with ten professors in five departments specializing in relevant fields, but was troubled about having to narrow my interests down to a single discipline or technique. Luckily, Prof. Ned Thomas, a senior faculty in the Department of Material Science, encouraged me to speak with a new faculty in Mechanical Engineering whose broad interests seemed to overlap with my own. That new faculty was Nick.

I immediately joined Nick's group after our first open-ended research discussion. I remember how he shared his passions about exploring light and sound for particle manipulation and advanced manufacturing. Since then, Nick has been a wonderful mentor and a role model for me. He has fully supported every research endeavor I proposed and undertook, trusting me even when I lost faith in myself. He nudged me to spend more time on the fundamentals and to prioritize efficiently – very persistently, week after week and year after year. I always gained fresh energy and forward momentum from our frequent meetings.

Perhaps most remarkably, he never seemed to care much about remaining within his own comfort zone, nor did he ever force me to conform to pre-set norms or artificial knowledge boundaries in academia. He taught me to think without restraints, appreciate constructive criticism, and persevere until the completion of each task. This gave me tremendous courage and comfort during the ups and downs of PhD.

After passing my doctoral qualifying exam, I began investing more time thinking about two big trends in technology. First, computer intelligence was rapidly automating jobs previously reserved for humans. Running a code overnight could outperform months of expert labor. This was terrifying yet also quite thrilling. I wanted to explore this direction during PhD – to combine intuition-driven and data-driven approaches to wave engineering design. Second, there were increasing legal conflicts over scientific information and aggregate online data; and I was curious about the delicate balance between public sharing and private monetization of new knowledge.

I approached Steven in 2014, seeking his guidance on both of these issues. He soon became my co-advisor with Nick's generous approval, and taught me to collaborate with scientists in the free software community. He also trained me to use algorithms, equations, and verbal logic more carefully. His dedication to public sharing of scientific knowledge inspired me in so many ways. I often wondered if Steven's unusual cheerfulness was the cause of his unusual selflessness or vice versa. So he made me feel strangely optimistic about humankind, even though I always received difficult problems to solve when I visited him. "Eunnie, it's actually quite doable if you write it like this! (starts typing a long problem) Next time you can show me ... "

As I journey beyond MIT, I will keep in my mind and heart what Nick and Steven have always shown me. I will strive to honor their teaching and kindness as I pave my own path at the interface of technology and law.

Next, I'd like to thank my thesis reader, Prof. George Barbastathis, for his advice and insights on holography and optics during our long and intense committee meetings. I also thank Prof. Ken Oye of MIT Political Science for his guidance as my advisor in the Graduate Certificate Program in Science, Technology, and Policy, through which I could further explore the legal division between intellectual property and intellectual commons in the software industry.

I thank my research mentors and teammates, especially Prof. Owen Miller, Dr. Homer Reid, Prof. Kin Hung Fung, Dr. Jeff Chou, Dr. Dafei Jin, Dr. Navid Nemati, and Dr. Matt Klug. They have been incredible colleagues, and I was lucky to work closely with them during my doctoral studies. I also thank Prof. Sang-Gook Kim,

Prof. Denis Lafarge, Prof. Evelyn wang, Prof. Marin Soljacic, Dr. Ivan Celanovic, and Prof. TieJun Zhang for their input on collaborative publications. I thank NSF and AFOSR MURI for funding support.

I am grateful to Prof. Seth Lloyd, Prof. Cullen Buie, and Prof. Irmgard Bischofberger for giving me the opportunity to work with them as their teaching assistant. I thank my career mentors Prof. Millie Dresselhaus and Prof. Bill Bonvillian for their life advice and encouragements. I thank my writing mentor Dr. Rebecca Thorndike-Breeze, personal trainer Betty Lou[1], and career counselors Lily Zhang and Jake Livengood at MIT Career Development Office. I thank the awesome and caring administrators in our department: Chevalley Duhart, Irina Gaziyeva, Leslie Regan, Joan Kravit, and Una Sheehan.

I sincerely thank my officemates and groupmates in Nanophotonics and 3D Nanomanufacturing Group, and in Nanostructures and Computation Group. I thank my friends and colleagues who shared their hopes, struggles, and silly moments with me during the past six years. I met many of them in the following groups: Graduate Women at MIT (GWAMIT), Optical Society of America (OSA/SPIE), Science Policy Initiative (SPI), Graduate Association of Mechanical Engineers (GAME), Korean Graduate Student Associations, Ashdown Community, Eastgate Community, and Samsung Scholarship. I also thank my teachers and friends I met before graduate school, who let me remain close to their hearts even though I lived oceans apart.

I thank my open-minded and loving parents, Prof. Kangseog Lee and Prof. Bokhee Im, my wise and considerate sister Yoon Ju Lee, and my supportive extended family and family in law, who always replenished strength and warmth in my core.

And lastly, I thank my love, Dr. Kyungheon "Special K" Lee, for his blessed presence in my daily life. He is kind and understanding to all living things, including his busy and bumbling wife. He is also a great engineer and a remarkable team leader both at work and home. I look forward to our continued journey together.

[1]Gender-specific prefixes are omitted in this thesis.

Contents

List of Figures

List of Tables

Chapter 1

Introduction

1.1 Motivation and Background

From steam engines to wind turbines to solar panels, engineers have been developing new and improved systems that store *energy*, perform *work*, or transfer *heat* in increasingly resourceful and sophisticated ways. We can group such engineering systems by their primary mode of energy transfer. In the size range from hundreds of micrometers down to a few nanometers,[1] energy transfer is often best mediated by *waves* – such as electromagnetic radiation [1, 2, 3] and mechanical vibration [4] Figure 1.1.1 illustrates the frequency spectrum for sound and electromagnetic waves, highlighting the different industrial applications in each frequency domain.

The aim of this thesis is to provide computer-aided design and analysis tools for mechanical systems that use waves as their primary mode of energy transfer. Specifically, we focus on simulating optimal wavefronts and subwavelength structures that enhance mechanical effects on the nanoscale. The systems analyzed in this thesis include: holographic optical tweezers in Chapter 3, photonic crystal solar absorbers in Chapter 4, and phononic crystal acoustic waveguides in Chapter 5. Each project and its respective chapter is illustrated in Figure 1.1.2.

Advances in nanoparticle engineering [5, 6, 7, 8, 9, 10, 11], meta-structures [12, 13, 14], and spatial wave modulation [15, 16, 17, 18, 19, 20, 21, 22] have created many

[1] $1\mu\text{m}=10^{-6}\text{m}$, $1\text{nm}=10^{-9}\text{m}$.

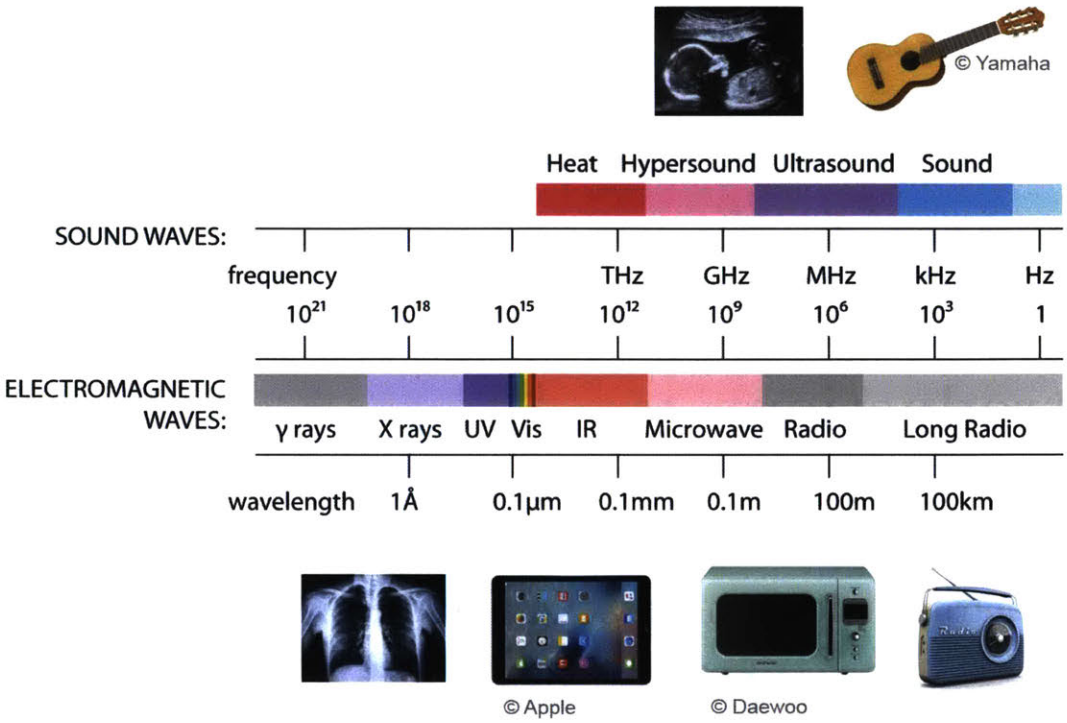

Figure 1.1.1: Frequency Spectrum for electromagnetic and sound waves.

new degrees of freedom for engineering wave-matter interaction. When exploring so many parameters, a large number of full-wave scattering problems must be solved efficiently. For example, if we want to test ten different parameters that each have five options, we need to run $5^{10} = 9,765,625$ simulations to examine every possible design candidate. This is often prohibitively time-consuming: A single three-dimensional (3D) full-wave simulation can easily take a few hours, especially if nontraditional wavefronts or subwavelength structures need to be modeled with high fidelity. In order to explore so many degrees of design freedom efficiently, we need a more targeted numerical design approach. Moreover, wave optimization is highly nonconvex by nature, and possesses many local optima due to interference and resonance. Thus convex optimization techniques cannot be simply applied [23].

We address this challenge by offering computer-automated design frameworks that effectively combine the best computational software developed in physics, numerical analysis, and inverse design. Much of the work presented is obtained using *free and open source* software tools available online [24, 25, 26, 27]. These tools allow us to

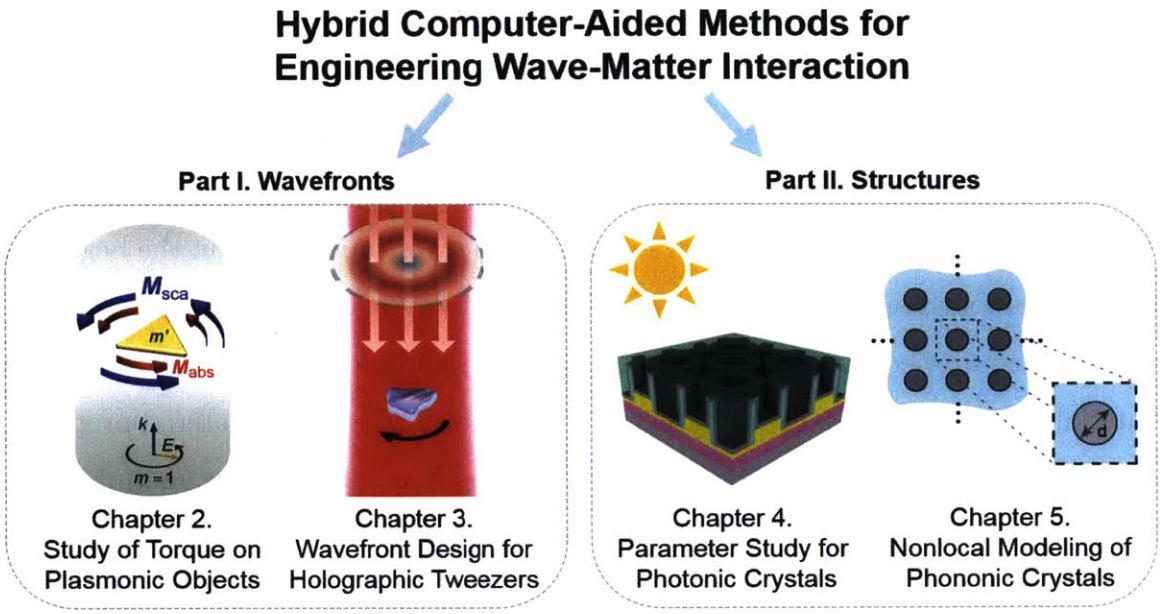

Figure 1.1.2: Overview of wavefronts and subwavelength structures studied in the thesis.

construct multi-component numerical schemes efficiently by modifying and improving upon high-quality source codes that are released with free and open source software licenses. In our experience, the availability and transparency of the source codes greatly reduce guesswork and repetition during development and debugging, and facilitate effective collaborations. We mainly use `C++` as our programming language, along with `Python/Julia` and `MATLAB`. When appropriate, we also use proprietary simulation engines [28] for large-volume computations.

Our work pushes to open the design space in wave engineering through efficiently exploring high-dimensional design parameter spaces via large-scale computational optimization. We are optimistic that our computational frameworks for wavefronts and subwavelength structures can be generalized and applied to other design problems, such as metamaterials, 3d manufacturing, and 3d imaging.

1.1.1 Mathematical Similarities in Engineering Light and Sound

On the microscopic level, electric and magnetic waves are governed by different physical laws. Electromagnetic waves are oscillations of electric and magnetic fields generated

by charged particles. Electromagnetic waves do not require a material medium and can radiate through vacuum. The relevant material properties for light waves are electric permittivity ϵ and magnetic permeability μ, which determine the phase velocity in the medium. Full-wave solutions to electromagnetic scattering problems on the microscopic level require solving the full Maxwell's equations. This is summarized in the beginning of my Master's thesis [29] based on [1]. Mechanical waves, on the other hand, cannot exist in vacuum because they propagate by momentarily deforming and restoring a material substance, which can be either solid or fluid. The relevant material properties are density ρ and compressibility χ, as well as elastic modulus, shear modulus, and viscosity, depending on the medium. As in the case for electromagnetic waves, these material properties determine the phase velocity in the medium. Full-wave solutions to acoustic scattering problems on the microscopic level require solving coupled thermal fluidic equations, as summarized in [30, 4] and in Chapter 5.

Yet on the macroscopic level in the long-wavelength limit, the propagation of electromagnetic and acoustic waves can be simplified in a similar way: We can homogenize, or average over a finite volume of interest, the complicated microscopic system dynamics and characterize each medium using its dispersion relation based on the material response of the constituent media. Sometimes the relevant material properties are easily available, as in Chapters 2 and 3 [31]. Other times they have to be measured experimentally, as in Chapter 4, or obtained through multiscale computation, as in Chapter 5. Analytical and computational methods for wave engineering thus share a great deal of mathematical similarity on the homogenized scale.

1.1.2 Numerical Methods for Wave Scattering Problems

Wave scattering problems can be simplified greatly if the wavelength is much longer or shorter than the characteristic geometric feature of the scatterer. When the size of the characteristic feature is much smaller than the wavelength, the intricate geometries become negligible. Also, when the feature is much larger than the wavelength, the intricate oscillations of the waves become negligible and we can simplify the waves as rays (as in ray optics and ray acoustics). Between these two extremes, we need to

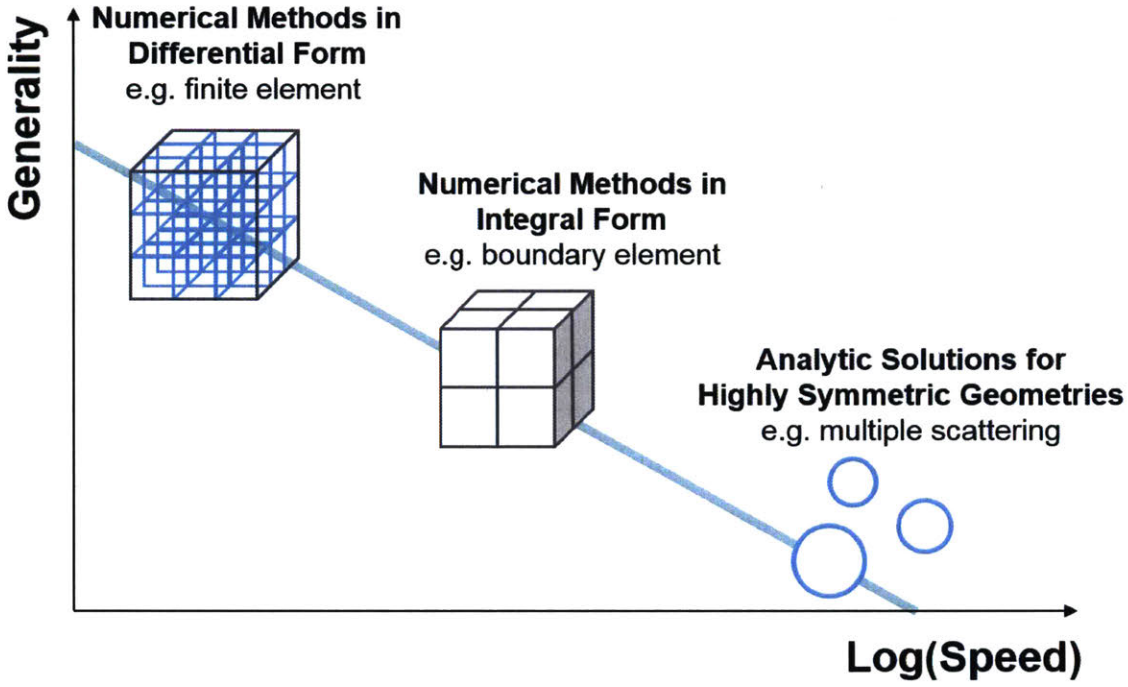

Figure 1.1.3: Illustration of the tradeoff between the speed and generality of numerical PDE solvers. Differential methods discretize the entire geometry and are therefore slowest yet most general (top left). Integral methods discretize the boundaries rather than the entire domain, and hence increase speed while decreasing generality for complicated physical problems (middle). Semi-analytic methods are very fast but are only available for highly symmetric geometries such as spheres (bottom right). The graph is purely conceptual rather than quantitative.

solve the governing partial differential equations (PDE's) in their full forms.

The *speed* and *generality* of various numerical PDE solvers are illustrated in Figure 1.1.3. First, differential solvers for PDE discretize the entire problem geometry and solve the governing PDE's on the mesh. If the given scattering problem is 3D, the mesh is also 3D. Such methods include finite difference time domain (FDTD) [32, 33] used in Chapters 2 and 4, and finite element method (FEM) [26, 34] used in Chapter 5. Differential PDE solvers are computationally expensive but are by far the most general method that can be applied to systems with complicated geometries and material compositions.

Next, integral methods, including the boundary element method (BEM) [35, 36, 25] used in Chapter 3, solve the integral form of the PDE on the material boundaries rather than in the entire domain, and hence increase speed while decreasing generality for complicated physics and boundary situations.

Lastly, semi-analytic methods, such as multiple scattering [37, 38, 39, 27] used in Chapter 5, employ analytical solutions of Eq. (??). Semi-analytic methods are very fast, but are only available for highly symmetrical geometries such as flat layers, spheres, and cylinders.

1.1.3 Matrix-based Formalism and the Dispersion Equation

It is often useful to formulate the partial differential equations describing a wave scattering system into a matrix form:

$$\boldsymbol{A}\mathbf{x} = \mathbf{b}, \tag{1.1.1}$$

where $\boldsymbol{A}$ is an $N \times N$ system matrix relating the input and output vectors $\mathbf{b}$ and $\mathbf{x}$, such as the incident and scattered fields. A similar formalism is used with a $N \sim 4000$ BEM Matrix in Chapter 3. This is useful when we are interested in engineering or measuring $\mathbf{b}$ and $\mathbf{x}$, such as in Chapters 2, 3, and 4.

We can also relate the scattering problem to an eigenvalue problem for the resonant modes of the system by setting $\mathbf{b} = 0$:

$$\boldsymbol{A}(\lambda)\mathbf{x} = 0, \tag{1.1.2}$$

where we include an explicit dependence on an "eigenvalue" λ , which is typically the frequency $\omega = 2\pi f$ or a wavevector component k, representing temporal or spatial oscillations, respectively. Here, $\mathbf{x}$ is the eigenvector, or the input vector that excites the intrinsic resonance of the system. If $\boldsymbol{A}(\lambda) = \boldsymbol{B} - \lambda\boldsymbol{C}$ for some matrices $\boldsymbol{B}$ and $\boldsymbol{C}$, this is simply a linear eigenvalue problem that can be solved by many standard methods [40]. However, in many practical cases $\boldsymbol{A}(\lambda)$ can depend in a more complicated way on λ. For example, a complicated ω-dependence might arise due to material dispersion [13]. When solving for the wavevector $\lambda = k$ at a fixed ω, typically $\boldsymbol{A}$ depends quadratically on k, a so-called "quadratic eigenvalue problem" that can be converted to a linear eigenvalue problem of twice the size [41].

For the general nonlinear eigenvalue problem (NEP) with an arbitrary (usually smooth) $\boldsymbol{A}(\lambda)$, there are many methods [42], including solving Eq. (1.1.2) directly (*e.g.,* by Newton's method) is a large system of nonlinear equations in $\mathbf{x}$ and λ, or by applying nonlinear solvers to a single scalar equation in the eigenvalue λ for the determinant of $\boldsymbol{A}$:

$$\det[\boldsymbol{A}(\lambda)] = 0.$$

In cases where one has a well defined wavevector k, including waveguides and periodic media [12], the relationship $\omega(k)$ is called the dispersion relation, which can be very complicated for an arbitrary periodic medium such as a photonic crystal for electromagnetism, studied in Chapter 4, or the phononic crystals considered for acoustic waves in Chapter 5.

In the long wavelength limit, as ω and k go to zero, however, matters simplify considerably: the wave doesn't "see" geometric features much smaller than the wavelength, but instead behaves as if it were traveling through an "average" homogeneous medium. This is called a *homogenization approximation* [43, 44, 45], and becomes exact in limit of infinite wavelength. In an isotropic homogeneous medium, the dispersion relation is

simply $\omega = c|k|$, or equivalently can be define the *dispersion equation*:

$$D(\omega, k) = \omega^2 - c^2|k|^2 = 0, \tag{1.1.3}$$

where c is the "phase velocity." In electromagnetism, the ratio c_0/c, where $c_0 \approx 3 \times 10^8$m/s is the speed of light in vacuum, is called the "effective index of refraction" of the homogenized material [1].

More generally, $c(\omega)$ may have a frequency dependence, even at long wavelengths (small k), corresponding to temporal material dispersion, also called "chromatic" dispersion [46, pp 14-24]: in the time domain, this gives a homogeneous material that does not respond instantaneously in time.

Even more generally, many authors have considered materials in which $c(\omega, k)$ also depends upon k. The simplest cases are ones in which $D(\omega, k)$ still depends quadratically on k but depends also on the direction: an anistropic medium, *e.g.,* described by an anisotropic permittivity ε in electromagnetism. More general dependencies on k, however, correspond to a *nonlocal,* or *spatially dispersive* medium, in which the response of the medium depends spatially on the input, via some convolution of the input [47, 48]. Nonlocal media can arise from physical materials, *e.g.,* via nonlocal charge transport in plasmonic materials at small length scales. Many authors have also attempted to extend the regime of validity of homogenization approximations to shorter wavelengths by defining an effective nonlocal medium c(ω,k) to give the correct dispersion relation [ref]. This is potentially problematic, because such a homogenized approximation may correctly reproduce the dispersion relation but fail to reproduce other behaviors of the exact materials, such as scattering from interfaces. Nevertheless, nonlocal homogenizations are interesting to explore, both from a numerical standpoint and because if they do approximately work they would give a much simpler way to understand complex media.

In this thesis, our numerical strategy is to choose and combine (i) an appropriate PDE solver to compute $\boldsymbol{A}(\omega)$ and (ii) an appropriate choice among Eqs. (1.1.1)-(1.1.3) for optimization or mode analysis, using a corresponding nonlinear solution algorithm.

1.2 Thesis Organization

As illustrated in Figure 1.1.2, Part I presents the design and analysis of holographic optical tweezers for nanoparticle manipulation, and Part II presents mode analysis of dissipative photonic crystals and phononic crystals.

Chapter 2 summarizes a geometric parameter study of optical angular momentum transfer from a circularly polarized plane wave to thin metal nanoparticles. [29, 49] Our FDTD analysis shows that higher-order multipolar plasmon modes can contribute to optical torque by efficiently converting the angular momentum mode of light to different states through resonant scattering. Torque induced by resonant scattering can contribute to 80% of the total optical torque in gold particles at multipolar resonance frequencies.

Chapter 3 presents how large-scale computational optimization [23, 50, 24] can be used to design superior and non-intuitive structured illumination patterns that maximize optical force or torque. By combining a compact cylindrical Bessel basis representation with a fast boundary element method and a standard derivative-free, local optimization algorithm, we demonstrate a 20-fold enhancement in optical torque per intensity over circularly polarized plane wave on a model plasmonic particle. We analyze the optimization results for 2000 random initial configurations, discuss the tradeoff between robustness and enhancement, and compare the different effects of multipolar plasmon resonances on enhancing force or torque.

Chapters 4 and 5 discuss dissipative and periodic subwavelength structures in optics and acoustics. Chapter 4 presents the numerical analysis for a broadband solar absorber, made of metallic-dielectric photonic crystal (MDPhC) structure developed and fabricated by Prof. Sang-Gook Kim's group at MIT. The surface of a solar panel can be intricately patterned and coated to receive as much sunlight as possible from all directions with minimal reflection. We present FDTD parameter study results and discuss the tunability and spectrum-selectivity of solar absorption.

Chapter 5 presents a multiscale numerical model for dissipative phononic crystals with strong nonlocality. The description is based on a nonlocal theory of sound

propagation proposed by Lafarge and Nemati. [51] We describe the nonlocal effective properties of a two-dimensional dissipative phononic crystal made of periodic arrays of rigid and motionless cylinders embedded in a viscothermal fluid such as air. We solve the nonlocal dispersion equation to find the least-attenuated mode in the phononic crystal, and compare our nonlocal scheme with the multiple scattering method. While the multiple scattering method is limited to very simple geometries only, our generalized method based on FEM is applicable to arbitrary phononic unit cell geometries.

Part I

Holographic Illumination for Nanoparticle Manipulation

Chapter 2

Optical Torque from Enhanced Scattering by Plasmon Resonance

This chapter is based on: Y. E. Lee, K. H. Fung, D. Jin, and N. X. Fang, "Optical torque from enhanced scattering by multipolar plasmonic resonance," Nanophotonics, Vol. 3(6): 343-440 (2014).

2.1 Introduction

Optical force arises when the linear momentum carried by light is transferred to matter through both absorption and scattering [52, 53]. When absorption dominates, each photon absorbed by the medium transfers a finite quanta of linear momentum $\hbar\mathbf{k}$ [1, 54], where $\hbar$ is the reduced Planck's constant and $\mathbf{k}$ is the wavevector of the incoming light. When scattering dominates, on the other hand, the total transferred linear momentum from each photon is determined by the difference of the wavevectors before and after scattering $\mathbf{k} - \mathbf{k}'$ [55]. The transfer of momentum through scattering is therefore not necessarily directly proportional to the number of photons scattered, which is the fundamental reason why it is possible to realize unconventional ways to transfer linear momentum from light to matter such as the recent example of an optical 'pulling' force [56, 57, 58].

Investigations on optical manipulation [59, 60] have been extended to the control

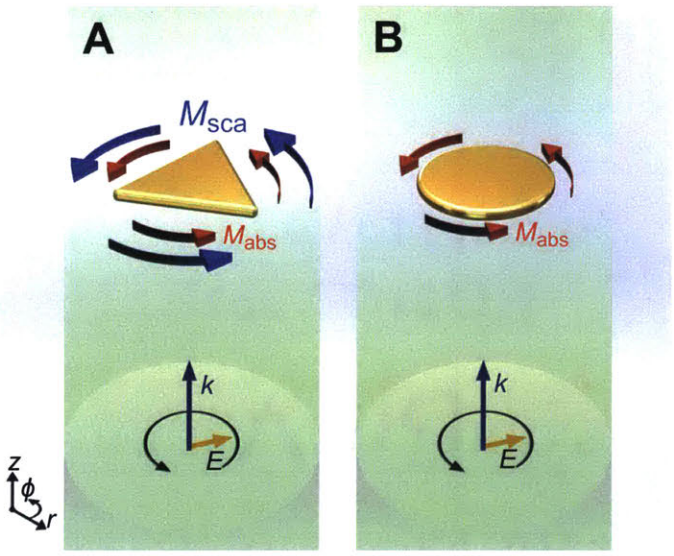

Figure 2.1.1: Two different mechanisms of optical torque generation mediated by absorption and scattering. A circularly polarized plane wave, denoted by the wavevector $\mathbf{k}$ and the electric field $\mathbf{E}$, is normally incident on two gold nanoparticles at plasmon resonance. $\mathbf{M}_{\text{sca}}$ and $\mathbf{M}_{\text{abs}}$ are the optical torque generated from scattering and absorption, respectively. (a) The incident light can exert torque on a triangular particle through both scattering and absorption. (b) In the case of a circular particle, scattering cannot contribute to an optical torque.

of optical torque and optical angular momentum [61, 62]. It has been well known that light carries both spin angular momentum [63, 64] and orbital angular momentum [65, 66]. Both can be used to rotate small particles. While the optical torque from absorption is proportional to the number of photons absorbed, torque from scattering can be modified with greater freedom as in the case of linear force. The essential requirement to create torque predominantly from scattering is that the scattered light should be made to exhibit a twist in the azimuthal direction, meaning that the angular momentum carried by the scattered field should be different from that of the incident field. This has been widely explored using microscale dielectric particles that have negligible absorption under stable optical trapping conditions [67]. One way to produce the necessary twist is to shine a carefully aligned beam that carries orbital angular momentum [68]. On the other hand, when the incident light carries only spin angular momentum or has no angular momentum to begin with, the twist needs to be provided by the optical response of the object; for example, the intrinsic

[69, 70, 71] and mimicked [72] anisotropy of the material, as well as the asymmetry of the structure, such as chirality or structural windmill effects [73, 74, 75, 76]. It has also been theoretically predicted that light can exert "negative optical torque" on aggregates of dielectric microspheres [77].

In contrast, the manipulation of subwavelength particles remains a more challenging issue: dielectric nanoparticles have negligibly small optical responses, and absorptive nanoparticles experience radiation pressure and thermal effects that often predominate the strength of conventional optical traps [78, 79]. Despite such restraints, researchers have developed various ways to produce optical torque on the nano-scale: the principles in creating structurally asymmetric metallic rotors [80, 81] have been scaled down to the nano-scale by enhancing the optical response of subwavelength particles through the excitation of surface plasmon resonance [82, 13]. Researchers have also demonstrated KHz-rate spinning of gold nanospheres in water by the absorptive transfer of spin angular momentum from circularly polarized light [83]. surface plasmon resonance has also been widely used in designing nano-scale optical elements, inside systems for the spatial modulation of light such as optical nano-tweezers [84, 85, 86, 87, 88], optical antennas [89, 90], and OAM-mediating metasurfaces [91, 92]. In fact, the contributions from absorption and scattering are often left undistinguished in the discussion of SP-enhanced mechanical effects. To our knowledge, there have been no systematic studies so far on the optical torque that is particularly associated with the scattering of light under plasmon resonance.

This article presents the study on how light scattering at plasmon resonance can provide an additional channel for the control of optical torque, in addition to the commonly acknowledged mechanism of absorption. Our numerical calculations are based on simple non-chiral geometries, via exciting the first few orders of multipolar surface plasmon resonance. In the literature, the phenomena of multipolar surface plasmon resonance of metallic nanoparticles have been widely reported for various symmetry-breaking geometries [93, 94, 95, 96, 97, 98], including the flat triangular nanoprisms [99, 100, 101] used in this work. We show that the angular momentum carried by the scattered field depends greatly on the azimuthal charge distribution on

the plasmonic surface, which is governed by the order of the multipolar surface plasmon resonance. This scattering-dominant mechanism of torque generation is distinctly different from the conventional means of absorption-dominant torque generation. The efficiency of angular momentum transfer is analyzed with respect to variations in size and rotational symmetry.

2.2 Method

Broken rotational symmetry fundamentally provides the selection rule not only for the emergence of multipolar resonance in plasmonic particles, but also for the possible channels of optical angular momentum conversion through light-matter interaction. We propose how structures supporting multipolar resonance can be designed to produce torque by dictating the azimuthal diffraction order of the scattered field.

Suppose that light carrying an azimuthal angular momentum of $\mathbf{J} = \hbar m\hat{\mathbf{z}}$ is normally incident on an optical system. In the cylindrical $(\hat{\mathbf{r}}, \hat{\boldsymbol{\varphi}}, \hat{\mathbf{z}})$ coordinates, the azimuthal field direction follows $e^{im\varphi}$, where m denotes the total azimuthal order number. The optical system supports a discrete N-fold rotational symmetry in $\hat{\boldsymbol{\varphi}}$, *i.e.*, the optical properties of the system are identical with respect to a rotation of an angular period of $2\pi/N$. After the process of scattering, the azimuthal distribution of the scattered field can change to $e^{im'\varphi}$, where m' is the total output azimuthal order of the scattered field that can be expressed as [102, 103]

$$m' = m + jN, \ (j = 0, \pm 1, \pm 2, \cdots) \tag{2.2.1}$$

in which j is an integer representing the angular diffraction order. The change in the azimuthal order number is a result of light diffraction, and therefore can be expressed by an angular grating rule. Eq. (2.2.1) can be interpreted as the angular counterpart of the linear grating equation $k' = k + jK, \ (j = 0, \pm 1, \pm 2, \cdots)$, where $k = |\mathbf{k}|$ represents the linear momentum of the photon in the direction of the wavevector, and K is the added lattice momentum when the optical properties of the system are identical with

respect to a translation by a linear period (pitch) of $2\pi/K$.

While all light-matter interactions follows Eq. (2.2.1) in principle, the angular grating effect is negligible when there is no mechanism to couple the light into nonzero diffraction order j. Most optical systems that are larger than the wavelength lack a mechanism to selectively enhance a particular output mode, and the dominant response becomes $m = m'$ with a conserved azimuthal order.

On the other hand, multipolar surface plasmon resonance is inherently successful at converting the azimuthal phase distribution of the plasmonic nearfield into the azimuthal order m' that matches the order of the multipolar resonance. Using this fact, a plasmonic structure possessing discrete rotational symmetry would serve as an effective 'angular diffraction grating' that can selectively enhance the conversion into a certain output mode with m' by matching the wavelength of the surface plasmon mode with the characteristic length scale of the angular grating.

A gold triangle depicted in Figure 2.1.1(a) is a simple example of an angular grating possessing 3-fold discrete rotational symmetry. We choose to investigate the results when the incident electric field is a RCP circularly polarized plane wave, described as

$$\mathbf{E}(r, \varphi, z) = E_0[\hat{\mathbf{r}} + i\hat{\boldsymbol{\varphi}}]e^{im\varphi}e^{ikz},$$

with $m = +1$ for right-handed circular polarization (RCP). Left-handed circular polarization (LCP) can be written as

$$\mathbf{E}(r, \varphi, z) = E_0[\hat{\mathbf{r}} - i\hat{\boldsymbol{\varphi}}]e^{im\varphi}e^{ikz},$$

with $m = -1$. Recall that any plane wave can be expressed as a weighted sum of two orthogonal circular polarization with a phase offset of $\pi/2$. Throughout this chapter, an RCP plane wave incidence is assumed without the loss of generality.

After interacting with the gold nanoparticle, the scattered electric field of total azimuthal order m' can be expressed as

$$\mathbf{E}'(r, \varphi, z) = [E_r(r, z)\hat{\mathbf{r}} + E_\varphi(r, z)\hat{\boldsymbol{\varphi}} + E_z(r, z)\hat{\mathbf{z}}]e^{im'\varphi}.$$

The resultant azimuthal order number m' is dictated by Eq. (2.2.1), which is $m' = m + 3j$ for 3-fold symmetry, where j is an integer. Using RCP incidence, the azimuthal order can be changed into values, including $m' = -2$, which represents a quadrupole azimuthal mode with an opposite direction of rotation, henceforth denoted as the negative quadrupole mode. Eq. (2.2.1) governs the possible orders of multipolar surface plasmon resonance that can be excited by a normally incident plane wave, which shows the natural connection between multipolar surface plasmon resonance and the possible channels of optical angular momentum transfer. Due to this change in the azimuthal distribution of the scattered field, the triangular particle is expected to experience a torque from scattering, as well as absorption. In Figure 2.1.1(a), the circular arrows represent the existence of torque contribution from not only absorption (red) but also from scattering (blue).

In contrast, a circular disk illustrated in Figure 2.1.1(b) bears continuous rotational symmetry. Mathematically, one may treat the disk to have $N \to \infty$, and so any non-zero diffraction order will require $m' \to \infty$, which is practically always decoupled from the incoming light. The circular disk fails to modify the azimuthal order of the scattered field. Therefore we predict that no scattering torque would arise for a circular disk, as illustrated in Figure 2.1.1(b).

As is well-known, the mechanical effects delivered by photons onto an object can be characterized via inspecting the photonic momentum flux around the object. For a mechanically fixed object exposed to a steady incident flux, the time-averaged total torque can be obtained from an area integral of the time-averaged Maxwell Stress Tensor (MST) $\overleftrightarrow{\mathbf{T}}$ over an arbitrary closed surface S surrounding the object:

$$\mathbf{M}_{\text{tot}} = \oint_S (\mathbf{r} \times \overleftrightarrow{\mathbf{T}}) \cdot \mathrm{d}\mathbf{A} = \mathbf{M}_{\text{abs}} + \mathbf{M}_{\text{sca}}. \tag{2.2.2}$$

In general, $\mathbf{M}_{\text{tot}}$ can be separated into the absorption part $\mathbf{M}_{\text{abs}}$, and the scattering part $\mathbf{M}_{\text{sca}}$, as discussed further below. The component of the MST reads

$$T_{\alpha\beta} = E_\alpha D_\beta + B_\alpha H_\beta - \frac{1}{2}\delta_{\alpha\beta}(\mathbf{E} \cdot \mathbf{D} + \mathbf{B} \cdot \mathbf{H}), \tag{2.2.3}$$

where $\mathbf{E}$, $\mathbf{D}$, $\mathbf{B}$ and $\mathbf{H}$ are the electric field, the electric displacement field, the magnetic flux density, and the magnetic field, respectively. A pair of indices α and β denotes a particular component of momentum flux that points along the α-axis and crosses the surface normal to the β-axis.

The distinction between the torque contributions from absorption and scattering can be made by acknowledging the fact that absorptive torque is proportional to the number of photons absorbed. For the part of the incoming photons that are eventually absorbed by the object, the corresponding optical torque can be calculated from [104]

$$\mathbf{M}_{\text{abs}} = \frac{C_{\text{abs}} I_{\text{inc}}}{\omega} m\hat{\mathbf{z}}. \tag{2.2.4}$$

2.2.4Here, $C_{\text{abs}}(\lambda) = P_{\text{abs}}/I_{\text{inc}}$ is the absorption cross section, in which P_{abs} is the power absorbed by the object and I_{inc} is the incident intensity. The number of absorbed photons per unit time is $P_{\text{abs}}/\hbar\omega$. In all of the calculations, the incident intensity I_{inc} is normalized to be 1. Physically, absorption is caused by material dissipation and is embedded into the calculation through the imaginary part of the dielectric function $\text{Im}\,[\varepsilon(\lambda)]$.

Since the value of the total optical torque can be numerically obtained through Eq. (2.2.2), the scattering contribution is calculated to be $\mathbf{M}_{\text{sca}} = \mathbf{M}_{\text{tot}} - \mathbf{M}_{\text{abs}}$. It is worthwhile to emphasize again that scattering torque cannot be calculated from a simple expression like Eq. (2.2.4), because the torque from scattering is not simply proportional to C_{sca}. The scattering cross section does not capture how the angular momentum of the scattered photons redistributes after scattering. A naive calculation can cause an over- or under-estimation of torque.

All of the numerical results presented in this letter is calculated using the finite-difference time-domain (FDTD) method [33, 28]. Without loss of generality, the metal used in this chapter is gold (with permittivity [31] given in Appendix A), the dielectric medium is air (with refractive index $n = 1$), and incident light is modeled as a broadband pulse that is analyzed as a collection of monochromatic incidence. Linear scattering is assumed, meaning that the angular frequency ω of the photon does not

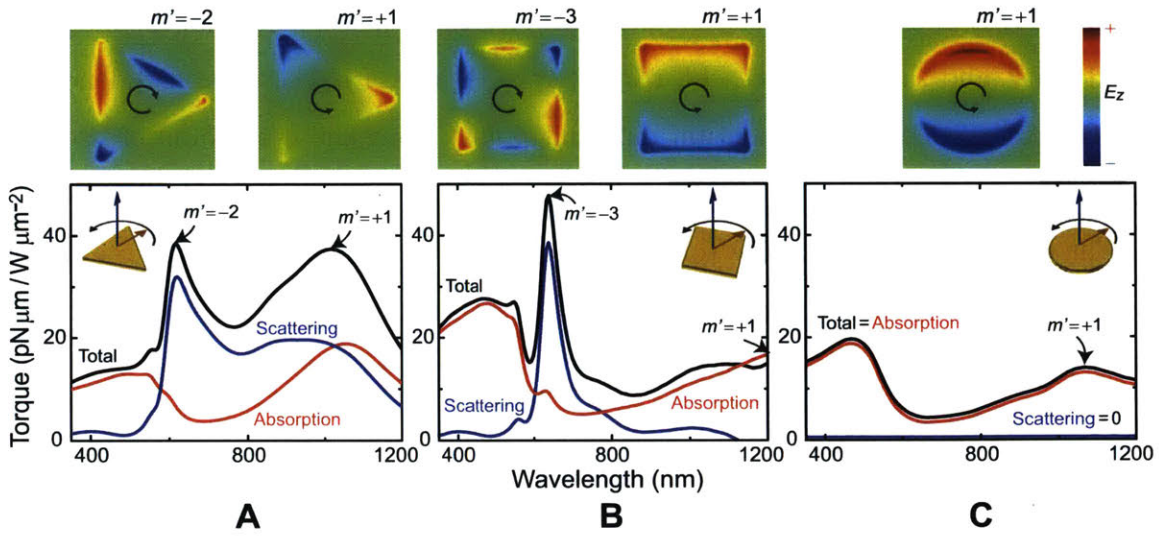

Figure 2.2.1: Calculated torque spectra for plasmonic particles excited at different orders of multipolar resonance. The total torque (black line) equals the summation of the scattering (blue) and absorption (red) contributions. Multipolar resonance peaks are labeled with the corresponding azimuthal order number m'. The corresponding electric field snapshot for each peak is plotted above, with black circular arrows denoting the direction in which the field pattern rotates. (a) The triangular particle possessing 3-fold symmetry supports a dipole mode ($m' = 1$) and a negative quadrupole mode ($m' = -2$). (b) The square particle possessing 4-fold symmetry supports a dipole mode and a negative hexapole mode ($m' = -3$). (c) In contrast, the circular particle only supports a dipole mode, and no torque is generated from scattering. All three particles have the same lateral characteristic length of 400nm and thickness 40nm.

change in the process of scattering.

2.3 Results and Discussion

The numerically obtained torque spectra are plotted in Figure 2.2.1. The results are compared between three representative geometries possessing different orders of rotational symmetry: N =3, 4, and ∞. The material and the incident illumination are identical for all three cases, following the setup of Figure 2.1.1. The characteristic lateral size and the thickness are identically set to be 400 nm and 40nm, respectively.

Figure 2.2.1(a) shows the torque spectrum for a triangular plate with 3-fold discrete rotational symmetry. A clear enhancement of scattering torque (blue) is observed at

the wavelength of the negative quadrupole mode ($m' = -2$). The distribution of the charges on the metal surface is represented by the colored electric field profiles plotted 4nm above the surface. The scattered quadrupole field rotates in the opposite direction from the incident field, because the possible orders after conversion is dictated by Eq. (2.2.1). As a result, an unusually large, scattering-dominant mechanical torque is created.

Figure 2.2.1(b) shows the consistent response of a square plate with 4-fold discrete rotational symmetry, which shows that the scattering torque is distinctly enhanced at the wavelength of the negative hexapole mode ($m' = -3$). Absorptive torque (red), on the other hand, does not exhibit sharp peaks, and shows a remarkable similarity between the three distinct geometries.

In stark contrast, the scattering torque is zero for the case of Figure 2.2.1(c) for the case of a circular disk with continuous rotational symmetry. No multipolar conversion is observed for the case of $N = \infty$. Since the azimuthal distribution of the scattered field resembles that of the incidence, scattering fails to create any torque.

The scattering contribution of torque by objects possessing discrete rotational symmetry originates from the constructive interference of the diffracted light. For subwavelength dielectric structures, the angular momentum conversion and hence torque generation via the scattering mechanism is quite small. However, the situation is rather different in metallic structures, where the conversion efficiency can be selectively enhanced by the corresponding order of multipolar surface plasmon resonance.

Traditionally, absorption has been regarded as the predominant mechanism of optical torque generation on plasmonic particles, especially when the transfer of spin angular momentum is concerned. Our results show that this is not always true. Scattering can become the predominant mechanism of torque generation, provided that the structure supports a conversion of azimuthal order between the incident and the scattered fields. Although in principle the scattered light with a converted azimuthal angular momentum cannot propagate to the far field, such a conversion is still capable of applying a significant torque onto the object in the near field.

To quantify the relative strength of scattering torque in the process, we define a

dimensionless conversion ratio η as

$$\eta = \frac{G_{\text{sca}}/\hbar m}{P_{\text{ext}}/\hbar\omega}. \tag{2.3.1}$$

In the numerator, G_{sca} is the total angular momentum per unit time carried away by the scattered field, $\hbar m$ is the angular momentum of each incoming photon. In the denominator, P_{ext} is the extinction power and $\hbar\omega$ is the energy of each extinguished photon. η can be either positive or negative. (See Appendix A Figure A.2.1 for the plot of extinction.)

In Figure 2.3.1, we show the calculated spectra of η for the three particles analyzed in Figure 2.2.1. (black) The colored lines represent the effect of particle size. According to Eq. (2.3.1), the value of η is equal to 1 in the absence of conversion. This is observed for all of the lines in the vicinity of λ =900nm, which falls into the dipole resonance regime. η converges to a constant very close to unity as the wavelengths become larger.

In contrast, the conversion ratios for the three geometries follow a clearly different trend in the wavelength range 400nm-800nm. In Figure 2.3.1(a), the black line corresponds to the dimensions of the particles in value of η dips down below zero when the negative quadrupole mode is excited. This indicates that the scattered field may carry an angular momentum in the opposite direction to that of the incident angular momentum, *i.e.*, $\eta < 0$. Under this circumstance, the object can experience an extraordinarily large torque. Figure 2.3.1(b) shows a similar trend, and the dips correspond to the negative hexapole mode of the square particle. The magnitude of the dip of the square particle is generally much smaller than that of the triangular particle, indicating a lower efficiency of angular momentum conversion. This is directly related to the quality of the surface plasmon resonance, which falls as the multipolar order increases. The size of torque depends not only on the efficiency of conversion but also on the size of the scatterer. In fact, the amount of torque is very sensitive to particle size, which explains why the size of torque is larger for the square in Figure 2.2.1, although the conversion is less efficient compared to the triangle.

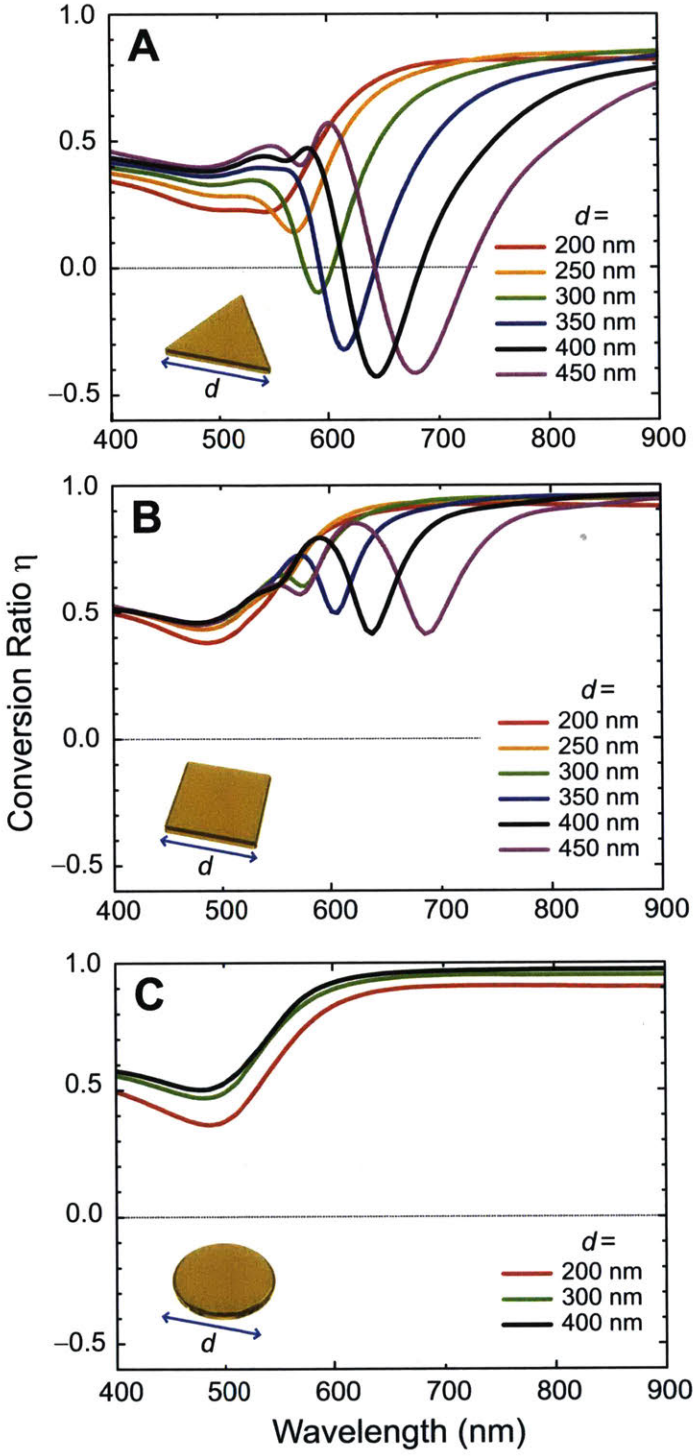

Figure 2.3.1: The angular momentum conversion ratio. The strength of angular momentum conversion is governed by the quality of multipolar plasmon resonance. The size parameter d is varied in each spectrum around the optimum size. (a) The triangular particle shows a dip in the conversion ratio at the negative quadrupole mode ($m' = -2$). (b) The square particle shows a dip at the negative hexapole mode ($m' = -3$). (c) The circular particle shows no multipolar conversion dip.

For the circular disk in Figure 2.3.1(c), η does not contain any feature of resonant angular momentum conversion. The graph shows the baseline that represents the angular momentum altered by the absorption of gold. This absorptive baseline is very similar for all of the results presented in Figure 2.3.1, regardless of their size or rotational symmetry. Since η quantifies the efficiency of angular momentum conversion between the incident and the scattered fields, the similarity in the absorptive baseline shows the limit for absorptive torque enhancement.

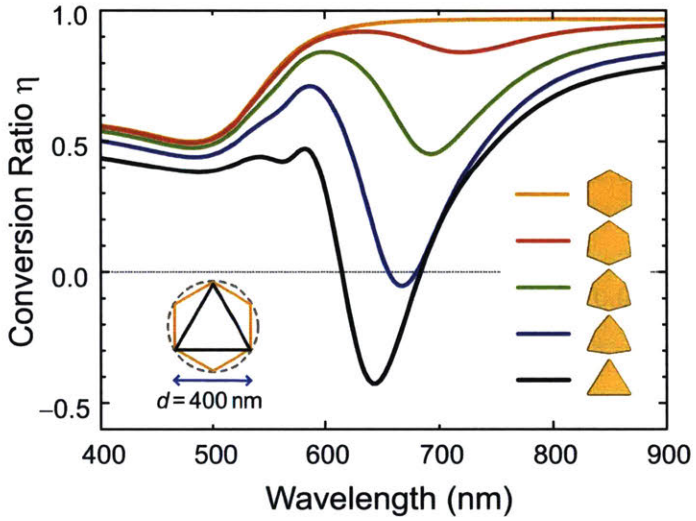

Figure 2.3.2: The importance of broken rotational symmetry in angular momentum conversion. The conversion ratio is plotted while a 6-fold hexagonal particle is gradually changed to a 3-fold triangular particle. η of the hexagon (yellow line) is almost indistinguishable from that of a circular particle (refer to Figure 2.3.1). The efficiency of the negative conversion is enhanced by breaking the 6-fold symmetry, thereby creating a larger change in the optical angular momentum after scattering.

In each graph, the colored lines show the optimal size for reaching the best conversion efficiency. The optimum size can be estimated by comparing the incident wavelength with the circumferential length of the particle ($d \sim \lambda$). While the qualitative behavior is insensitive to small size variations, the relative size of the dips represents the difference in the quality of the multipolar surface plasmon resonance. When the particle size is made much smaller or much larger than λ, the metallic particle can no longer support the high-quality multipolar surface plasmon modes, and the torque from scattering will be lost.

The importance of broken rotational symmetry can be explicitly appreciated in Figure 2.3.2. We show how η varies when continuous symmetry is gradually broken, from 6-fold symmetry to a 3-fold symmetry. The change in the conversion ratio dip is indeed very sensitive to the symmetry of the geometry. In this series of geometry being studied, the lower the order of discrete rotational symmetry is, the more remarkable the resonant torque enhancement can be.

2.4 Conclusion

In this chapter, we model representative nanoparticles that scatter, absorb, and radiate light in various directions in space and analyze how radiation force or torque relates to multipolar plasmon resonance. The numerical simulations suggest that the SP-enhanced scattering can lead to a negative angular momentum conversion ratio, and hence produce an extraordinarily large torque. We show that torque induced by resonant scattering can contribute to 80% of the total optical torque in gold particles at multipolar resonance frequencies.

While this chapter discusses the concept of angular momentum transfer between photons and a flat nanostructure in the cylindrical coordinates, we foresee that this approach can be generalized to three dimensional geometries in the near future. Our finding may lead to useful applications in the field of light-mediated mechanical manipulation as well as spatial light manipulation using metamaterial elements.

Chapter 3

Computational Inverse Design of Non-intuitive Illumination Patterns to Maximize Optical Force or Torque

This chapter is based on: Y. E. Lee, O. D. Miller, M. T. H. Reid, S. G. Johnson and N. X. Fang, "Computational Inverse Design of Non-Intuitive Illumination Patterns to Maximize Optical Force or Torque," Optics Express, Vol. 25(6): 6757 (2017).

3.1 Introduction

The enhanced torque results presented in Chapter 2 motivated us to further investigate how to maximize such unconventional optical forces or torques by varying the incident fields, from simple circular polarized plane waves to spatially modulated holographic illumination. Here we show how large-scale computational optimization [23, 50, 24] can be used to design superior and non-intuitive structured illumination patterns that achieve 20-fold enhancements (for fixed incident-field intensity) of the optical torque on sub-micron particles, demonstrating the utility of an optimal design approach for the many nanoscience applications that rely on optical actuation of nanoparticles [60, 105, 106].

Recent advances in nanoparticle engineering [5, 7] and holographic beam-generation

via spatial light modulators (SLMs) [15, 16, 17, 19] and other phase-manipulation techniques [107, 20, 21, 22] have created many new degrees of freedom for engineering light-particle interactions beyond traditional optical tweezers.

Structured illumination broadly refers to a technique in which a spatially modulated laser field pattern is projected onto the sample. In 3D imaging, researchers project known patterns with different spatial frequencies and record the deformed image after striking the object surfaces. [108, 109] This allows vision systems such as 3D scanners to calculate the depth and shape of the objects. In particle manipulation, structured illumination is used to produce light fields that carry specific distributions of optical momentum and angular momentum, to be efficiently transferred to the given material object.

Enhanced and unusual optical forces and torques can be engineered by designing material objects [110, 81, 83, 70, 111] and/or structured illumination, with the latter including "tractor beams" [57, 58] and beams carrying optical angular momentum [67, 103, 77, 112]. These increased degrees of freedom pose an interesting design challenge: for a given target object, what is the optimal illumination pattern to produce the strongest optical force or torque? While a small number of Gaussian beam parameters can be manually calibrated for optimal performance using manual trial-and-error [113], an arbitrary 3D vector field requires a more targeted approach. Moreover, optimization of a 3D vector field is highly nonconvex by nature, and possesses many local optima due to wave interference and resonance. When exploring so many parameters, a large number of scattering problems must be solved efficiently, which requires careful design of the optimization framework.

Research in computational optimization of optical actuation has focused on the design of new material geometries [114, 115] and on the improvement of multiplexed optical traps for microscale dielectric particles (holographic optical tweezers) [116, 117, 118, 119, 120, 121, 122]. However, no computational method has been available to design structured illumination for unconventional target objects that are nonspherical, lossy, or nanometer-scale, thereby requiring a costly full-wave numerical simulation for computing optical force and torque.

We present a compact and rapid computational framework to optimize structured illumination for the mechanical actuation of an arbitrary target object. We combine (i) a compact Bessel-basis representation (Sec. 3.2); (ii) a numerical solver based on boundary element method (BEM) that discretizes the surfaces of a 3D scattering problem to form a BEM matrix, and solves hundreds of thousands of incident-field configurations using the same matrix (Sec. 3.2); (iii) an appropriate optimization algorithm that exploits the smoothness of the nonconvex and nonlinear optimization problem (Sec. 3.2); and (iv) a suitable figure of merit (FOM) and optimization constraints (Sec. 3.2). As a result, we rapidly attain many-fold improvements in optical forces and torques over random field or plane wave illuminations (Sec. 3.3.1), and discuss the tradeoff between enhancement and robustness of optimization (Sec. 3.3.3). Furthermore, a given material object may have scattering resonances at various frequencies, and the choice of frequency for the incident field has several important implications. When comparing interactions with two different resonances, we were able to distinguish the impact of the change in the resonant field pattern from the change in the resonance lifetime. Controlling for the change in lifetime, we found that torque seems to favor higher-order (*e.g.*, quadrupole) resonances with greater angular momentum, while force seems to favor lower-order (*e.g.*, dipole) resonance with greater field intensity within the particle (Sec. 3.3.2).

3.2 Method: Optimization Framework

A structured-illumination optimization aims to find the best 3D vector field, *i.e.*, the one that maximizes a desired FOM for a given scattering problem (see Figure 3.1.1). Our choice of the Bessel basis expansion is described in Sec. 3.2. Sec. 3.2 and 3.2 discuss the BEM solver and the optimization algorithm. Lastly, Sec. 3.2 explains force and torque FOMs and the corresponding optimization constraints. The entire numerical framework is implemented with `C++`.

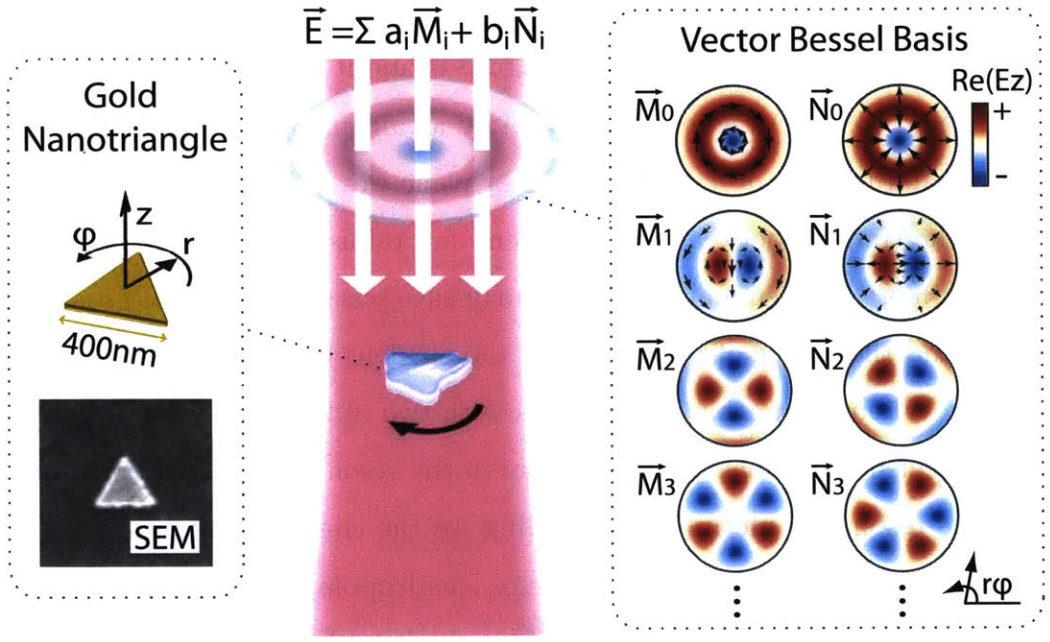

Figure 3.1.1: Schematic of a structured vector-field illumination, analytically represented with a vector Bessel basis. The right inset shows the distributions for electric field (color) and polarization (black arrows) of the vector Bessel basis. The illumination can be optimized to produce maximum mechanical force or torque on an example target particle. The gold nanotriangle in the left inset has edge length 400nm, thickness 40nm, and rounding diameter 30nm. The scanning electron microscope (SEM) image shows an experimental sample fabricated using electron-beam lithography. This demonstrates that such particles can be made, but all results presented here are purely computational.

Analytical Representation of Structured Illumination

The computational design of structured illumination requires a compact analytical representation of an arbitrary 3D vector field. The vector field will contain spatial variations in both intensity and phase, and must satisfy the vector wave equation [1]. The electric field can be represented using a basis expansion $\mathbf{E} = \sum_{i=0}^{N} c_i \boldsymbol{\phi}_i$, where the complex scalar coefficient c_i determines the relative intensity and phase of each mode $\boldsymbol{\phi}_i$.

The choice of coordinates and the basis functions $\boldsymbol{\phi}_i$ depends on the problem geometry. While the spherical coordinate system is a common choice in Mie scattering [38, 54], it requires a very large number of modes N to represent light propagating along a linear axis and potentially interacting with flat substrates or SLMs. The Cartesian coordinate system is also ill-suited because it requires large N to describe laser beams with a finite radius. We find that the cylindrical coordinate system [2, 18] is well suited, requiring a small number of modes to describe structured illumination with varying distributions of linear and angular momentum.

Among the wide menu of cylindrical basis functions (*e.g.*, Bessel, Laguerre-Gaussian, Hermite-Gaussian, and so forth) [18], we choose the Bessel basis [123, 124] for its compact analytical expression, derived from the scalar generating function

$$\psi_m(r, \varphi, z) = J_m(k_t r) \exp(im\varphi + ik_z z), \tag{3.2.1}$$

where J_m is the mth-order Bessel function, k_t is the transverse wavevector in $\hat{r}$, and k_z is the longitudinal wavevector in $\hat{z}$, satisfying $k_t^2 + k_z^2 = 2\pi/\lambda$. The ratio between k_t and k_z specifies the numerical aperture of the basis, $NA = \arctan(k_t/k_z)$. Higher NA represents greater transverse momentum that can increase optical torque. But the permissible range of NA is often dictated by experimental considerations, and the range of NA in the optimization can be set accordingly.

Taking spatial derivatives of Eq. (3.2.1) gives

$$\mathbf{M}_i = \nabla \times (\psi_i \mathbf{u}_z), \qquad \text{(azimuthal polarization)} \tag{3.2.2}$$

$$\mathbf{N}_i = \frac{1}{k} \nabla \times \mathbf{M}_i, \qquad \text{(radial polarization)} \tag{3.2.3}$$

where $\mathbf{u}_z$ is the unit vector in $\hat{z}$, and $\mathbf{M}_i$ and $\mathbf{N}_i$ are the ith bases for azimuthal and radial polarization, respectively (right inset of Figure 3.1.1). The incident electric field $\mathbf{E}_{\text{inc}}$ can be expressed as:

$$\mathbf{E}_{\text{inc}}(r, \phi, z) = \sum_{i=0}^{N} a_i \mathbf{M}_i + b_i \mathbf{N}_i, \tag{3.2.4}$$

where a_i and b_i are the complex scalar coefficients. Bessel basis produces the most compact expressions for $\mathbf{M}_i$ and $\mathbf{N}_i$ because the magnitude of ψ does not vary with z, reducing $\partial/\partial z$ terms in Eqs. (3.2.2) and (3.2.3).

We can use Eq. (3.2.4) to approximate a CP planewave configuration near the nanoparticle by setting $NA = 0.01°$ and $a_i,\ b_i = 0$, except for $a_1 = 1$. This approximation is used once in Figure 3.3.1 to start the optimization from a CP planewave. All other CP planewave results are computed without approximations, using $\mathbf{E}(r, \varphi, z) = [\mathbf{u}_r + i\mathbf{u}_\varphi] \exp(i\varphi + ikz)$ instead of Eq. (3.2.4).

Note that we intentionally decouple our optimization framework from the idiosyncratic differences in the spatial resolution of the SLMs. A wide variety of experimental methods (*e.g.*, superposed pitch-fork holograms) [15] can be used to generate beams expressed as Eq. (3.2.4), for a finite N and NA. We consider numerical apertures with opening angles $\leq 10°$ and 12 basis functions ($N = 5$).

Numerical Solver

The optimization process itself has no restrictions on the choice of the numerical solver, so the biggest consideration is the computational cost: the smaller the the better. We choose the Boundary Element Method (BEM) [35, 36] for several reasons. In comparison to other scattering methodologies such as the finite-difference or finite-

element methods, BEM is particularly well-suited to the type of large-scale optimization problem requiring a rapid update of the incident field for a given geometry and a given wavelength λ_{opt}.

$$\underbrace{\boldsymbol{M}}_{\substack{\text{fixed} \\ \text{BEM matrix}}} \quad \underbrace{\mathbf{c}}_{\substack{\text{output} \\ \text{current}}} = \underbrace{\mathbf{f}}_{\substack{\text{rapidly updated} \\ \text{input field}}} \tag{3.2.5}$$

In Eq. (3.2.5), the BEM matrix $\boldsymbol{M}$ remains fixed for a given geometry and frequency, while the column $\mathbf{f}$ representing the incident field is rapidly updated at each step of the optimization process. This allows hundreds of thousands of scattering configurations to be computed on the order of a few hours. In addition, BEM projects the 3D scattering problem onto a 2D surface mesh, thereby reducing the computation volume by a factor of $1/2000$ in the nanoparticle scattering problem we consider. Lastly, recent improvements [125] have significantly increased the speed with which optical force and torque can be computed in BEM.

Optimization Algorithm

Structured-illumination optimization is nonlinear and nonconvex, such that searching for a global optimum is prohibitively expensive. Therefore we choose a local algorithm with random starting points. We choose one of the simplest solutions available: constrained optimization by linear approximation (COBLYA) [50], a derivative-free algorithm that exploits the smoothness of the problem. An open-source implementation of COBYLA is available through NLopt [24].

The constructed numerical framework is graphically illustrated in Figure 3.2.1.

Figure of Merit and Optimization Constraints for Optical Force and Torque

We consider two types of optical actuation with respect to the object coordinate (left inset of Figure 3.1.1); the force F_z and torque T_z. In order to avoid the optimizer from increasing the brightness of the beam indefinitely, we choose to divide the force and

torque by the average incident-field intensity on the particle surface ($I_{\text{avg}} = \overline{|E_{\text{inc}}|^2}/2Z_0$, where Z_0 is the impedance of free space), which is easily computed in BEM. We choose the incident-field rather than the total-field intensity to avoid penalizing high extinction efficiency. I_{avg} is measured on the particle surface because we want to account for the portion of the beam that interacts with the target particle, rather than the entire beam. We choose nondimensionalized figures of merit:

$$\text{FOM}_F = \frac{F_z}{I_{\text{avg}}} \cdot \left(\frac{\pi c}{3\lambda^2}\right), \tag{3.2.6}$$

$$\text{FOM}_T = \frac{T_z}{I_{\text{avg}}} \cdot \left(\frac{4\pi^2 c}{3\lambda^3}\right), \tag{3.2.7}$$

where the constants in parentheses reflect ideal single-channel scattering. The largest [126, 127, 128] scattering cross-section into a single (spherical harmonic) channel is $3\lambda^2/2\pi$, which when multiplied by single-photon changes in linear ($2\hbar k$) and angular ($\hbar$) momentum per photon, divided by the photon energy ($\hbar\omega$), yields the constants in Eqs. (3.2.6) and (3.2.7).

Based on the geometry and material composition of the particle, force or torque in various directions can arise even when the incident field itself does not provide an imbalance in optical momentum. Optimization constraints can be added to suppress actuation in undesired directions. We suppress actuation in directions other than $\hat{z}$ using smooth constraints: $\left(|\mathbf{F}|^2 - F_z^2\right)/|\mathbf{F}|^2 \leq 0.01$ and $\left(|\mathbf{T}|^2 - T_z^2\right)/|\mathbf{T}|^2 \leq 0.01$, where the limiting value 0.01 is set to ensure that F_z and T_z exceed 99% of the force and torque magnitudes $|\mathbf{F}|$ and $|\mathbf{T}|$, respectively.

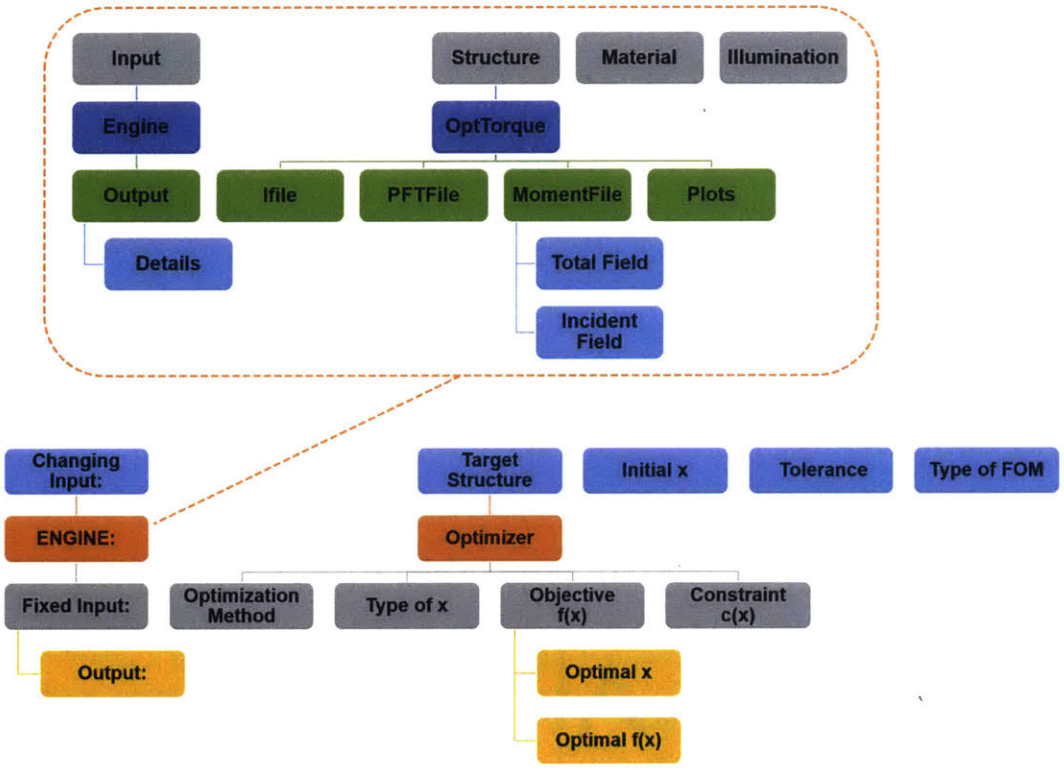

Figure 3.2.1: Overview of components comprising the numerical optimization framework. Top: numerical PDE solver based on BEM. Bottom: nonlinear optimizer that optimizes a parameter vector $\mathbf{x}$ to maximize the figure of merit $f(\mathbf{x})$ subject to constraint $c(\mathbf{x})$. The numerical PDE solver is included in the optimizer to compute the BEM matrix at every iteration.

3.3 Results and Discussion

We demonstrate our illumination-field optimization framework on the gold nanotriangle illustrated in Figure 3.1.1. Chapter 2 analyzes the optical force and torque on such a particle for circular polarized (CP) planewave illumination. CP planewave is a common incident-field choice [104, 129, 83, 70] for torque generation due to its intrinsic spin angular momentum, but we find in our computational optimization that highly optimized field patterns can show 20x improvement of FOM_T. The wavelength of illumination in each optimization, λ_{opt}, is chosen to correspond to the plasmon resonance wavelengths of the model particle.

Sec. 3.3.1 presents the distribution of 2000 local-optimization results and discusses the optimized field-patterns. Sec. 3.3.2 analyzes the wavelength-dependence of optical force and torque for optimized illuminations, based on the choice of λ_{opt}, and compares the results with the reference force and torque from CP planewave. Lastly, the tradeoff between robustness and enhancement is discussed in Sec. 3.3.3.

3.3.1 Illumination-field Optimization from 2000 Randomly Selected Initial Configurations

The illumination-field design space is nonconvex and littered with local optima, due primarily to wave-optical interference effects. We survey this broader design space by restarting our local-optimization algorithm 2000 times with randomly selected initial configurations that are constructed using Eq. (3.2.4), where the complex coefficients a_i and b_i are uniform random numbers bounded by $|a_i|, |b_i| \leq 1$. The results are summarized in Figures 3.3.1 and 3.3.2 at $\lambda_{\mathrm{opt}} = 1028\mathrm{nm}$ (dipole resonance) and 625nm (quadrupole resonance), respectively. At both wavelengths, we find that more than 50% of local optimization from random starting points can achieve over 5x enhancement of FOM_T compared to CP planewave reference, and that the optimized field patterns contain various combinations of Bessel-basis modes without a systematic convergence to one over the others. The distributions are plotted in log-scale to increase the visibility of small bins.

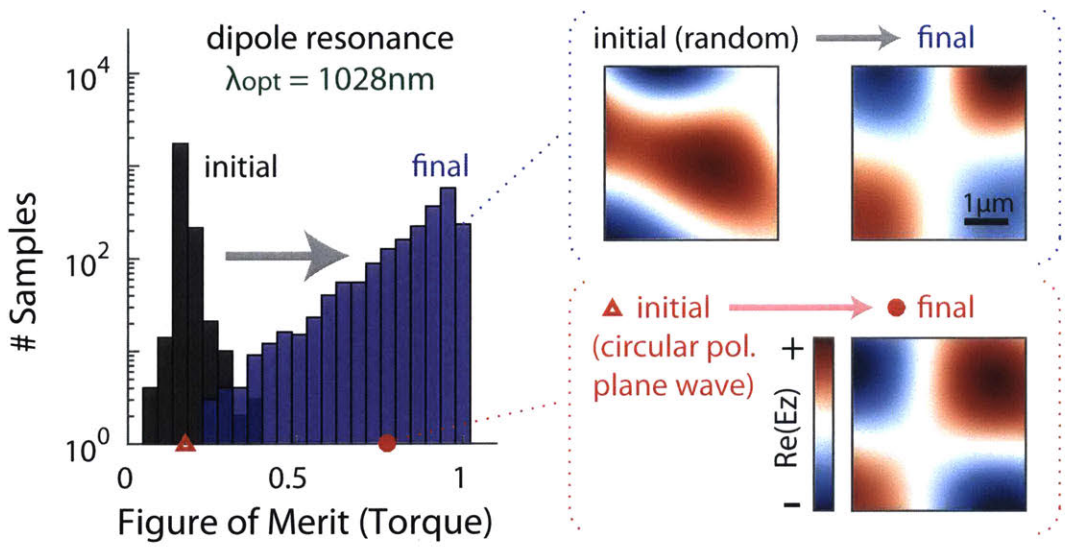

Figure 3.3.1: Distribution of FOM for 2000 randomly chosen incident field configurations at 1028nm, before (black) and after (blue) optimization. Red marks on the x-axis indicate the initial (triangle) and final (circle) FOM when the optimization starts from a circularly polarized plane wave. Representative incident fields are plotted in the right.

In Figure 3.3.1, the median FOM_T at 0.913 is very close to the best FOM_T at 1.01 and the distribution is predominantly concentrated to the right: the 4 rightmost bars represent 69% of all samples, which all achieve over 5x enhancement of FOM_T compared to CP planewave reference at 0.169 (marked with a red triangle). The insets show the optimization results from two different starting points – random field (top) and CP planewave (bottom) – that reach similar optimized field patterns. We also observe that a variety of other patterns, dominated by different combinations of Bessel-basis modes, can produce a nearly identical or superior FOM.

In Figure 3.3.2, the final FOM_T distribution is more dispersed between the median at 3.934 and the best at 10.94, which respectively achieve over 5x and 14x enhancement compared to CP planewave reference at 0.779. As in Figure 3.3.1, the results concentrate heavily around the median; however, in Figure 3.3.2 a small number of samples achieve a remarkable improvement above 14-fold. The top inset shows four different field patterns that produce a nearly identical FOM_T above the median, and the bottom inset shows the field-pattern with the highest FOM_T.

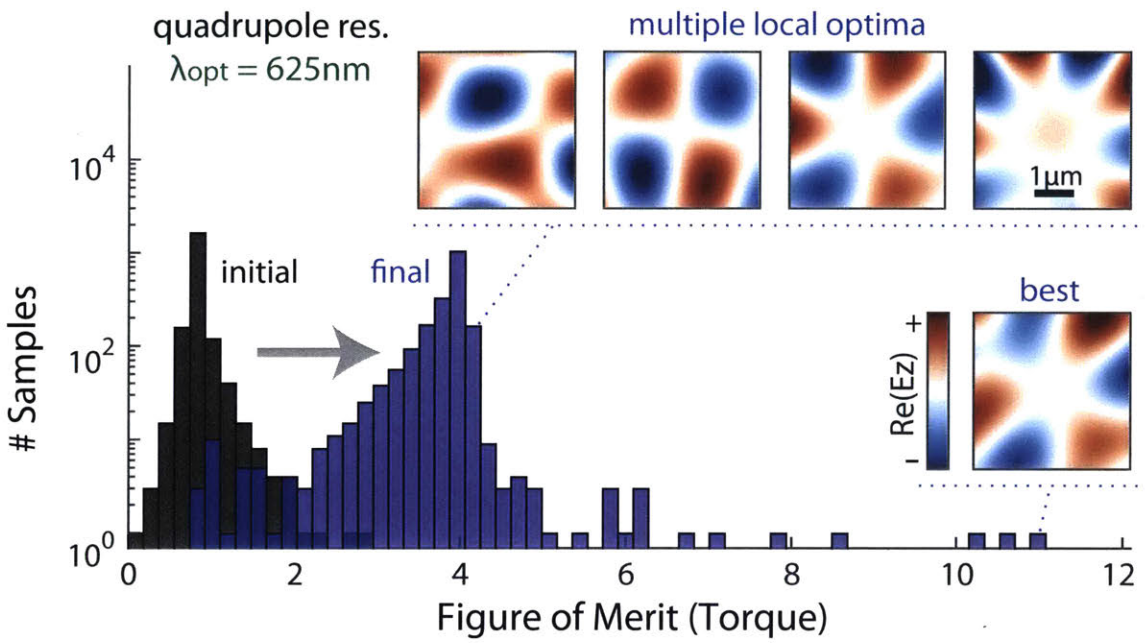

Figure 3.3.2: Distribution of FOM for 2000 randomly chosen incident field configurations at 625nm. Top inset shows four different field patterns with a near-identical FOM near the median, and the bottom inset shows the field with the best FOM.

The optimized coefficients for the best optimized illuminations at 1028nm and 625nm, plotted in Figures 3.3.1 and 3.3.2, are displayed in Tables 3.3.1 and 3.3.2, respectively. A comparison of all optimized field patterns at 1028nm and 625nm shows that the latter contains more higher-order Bessel-basis contributions. Moreover, the coefficients for the azimuthal mode $\mathbf{M}_i$ generally have a larger magnitude than the coefficients for the radial mode $\mathbf{N}_i$. We find that the radial modes do contribute to enhancing the optical torque, not through the direct first-order transfer of angular momentum, but possibly through second-order or higher order effects based on interference and resonance.

3.3.2 Dependence on Illumination Wavelength

We further investigate the influence of λ_{opt} by plotting optical force or torque per incident-field intensity I_{avg} as a function of illumination wavelength. In Figures 3.3.3(a) and 3.3.3(b), the reference planewave force spectrum (black dashed line) is identical in both plots, clearly dominated by a broad dipole resonance with smaller peaks at

Table 3.3.1: Vector Bessel basis coefficients for the best optimized illumination at $\lambda_{\text{opt}} = 1028\text{nm}$.

	a_i	b_i	$\lvert a_i \rvert$	$\lvert b_i \rvert$
$i = 0$	$0.0042 - 0.0076i$	$0.0115 - 0.0009i$	0.0087	0.0115
$i = 1$	$-0.0015 - 0.0030i$	$0.0014 - 0.0019i$	0.0033	0.0024
$i = 2$	$0.0225 - 0.8850i$	$-0.0095 + 0.1075i$	0.8853	0.1079
$i = 3$	$-0.0448 - 0.3629i$	$-0.0066 + 0.0376i$	0.3657	0.0381
$i = 4$	$0.1050 - 0.1177i$	$-0.0016 - 0.0409i$	0.1577	0.0409
$i = 5$	$-0.0363 - 0.8505i$	$-0.0611 - 0.0033i$	0.8512	0.0612

Table 3.3.2: Vector Bessel basis coefficients for the best optimized illumination at $\lambda_{\text{opt}} = 625\text{nm}$.

	a_i	b_i	$\lvert a_i \rvert$	$\lvert b_i \rvert$
$i = 0$	$-0.0134 + 0.0157i$	$-0.0020 - 0.0043i$	0.0207	0.0048
$i = 1$	$-0.0046 + 0.0041i$	$0.0032 - 0.0004i$	0.0062	0.0033
$i = 2$	$0.0033 + 0.0717i$	$0.0000 - 0.1100i$	0.0718	0.1100
$i = 3$	$-0.9441 + 0.7057i$	$-0.0222 + 0.7606i$	1.1787	0.7609
$i = 4$	$0.0994 + 0.1361i$	$0.0582 + 0.2958i$	0.1686	0.3015
$i = 5$	$-0.1726 + 0.9618i$	$-0.7185 - 0.0036i$	0.9772	0.7185

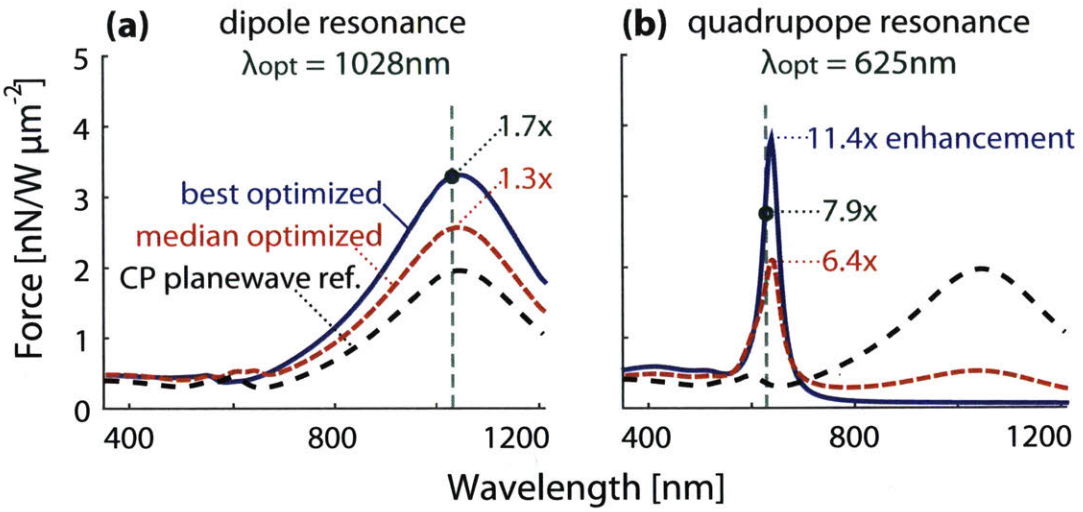

Figure 3.3.3: Force spectrum for two different target wavelengths; (a) 1028nm and (b) 625nm. The spectra for the best (blue line) and the median (red dashed line) optimized field configurations are each labeled with the factor of enhancement, with respect to CP planewave reference (black dashed line).

higher-order resonances. Through illumination-field optimization, we can enhance the force at the dipole mode while suppressing higher-order modes, as shown in Figure 3.3.3(a), and also enhance the force at the quadrupole mode while suppressing the dipole mode, as shown in Figure 3.3.3(b).

In Figures 3.3.4(a)-3.3.4(c), the reference planewave torque spectrum (black dashed line) is identical in all three plots and peaks at both dipole and quadrupole resonances with nearly equal heights, as explained in detail in Chapter 2. Illumination-field optimization at dipole resonance and off-resonance achieve a similar 6x-boost at the chosen λ_{opt} value without suppressing the quadrupole resonance. The optimized total fields in Figure 3.3.4(d) at 1028nm and 805nm both exhibit a 4π phase change around the circumference of the particle, resembling a quadrupole resonance.

In 3.3.4(c), on the other hand, the best optimization at quadrupole resonance achieves a remarkable 20x improvement while suppressing much of the dipole resonance; the median optimization also achieves 12x improvement while suppressing the dipole resonance to a lesser extent. The optimized total field in Figure 3.3.4(d) at 625nm shows a distinct, highly resonant distribution.

When comparing interactions with two different resonances, we were able to

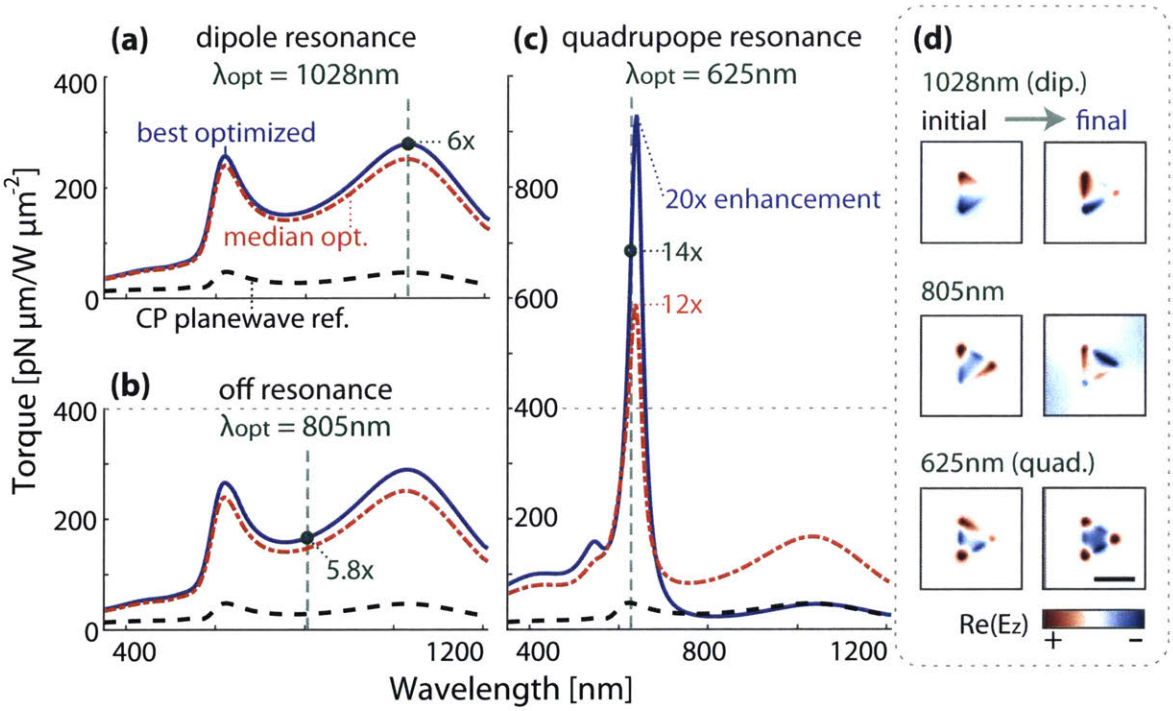

Figure 3.3.4: Torque spectrum for three different target wavelengths; (a) 1028nm, (b) 805nm, and (c) 625nm. The spectra for the best (blue line) and the median (red dashed line) optimized field configurations are each labeled with the factor of enhancement, with respect to CP planewave reference (black dashed line). (d) The total-field distributions of the initial random field (left) and the final optimized field (right) for the best optimized field configurations at the three target wavelengths. Scalebar is 400nm.

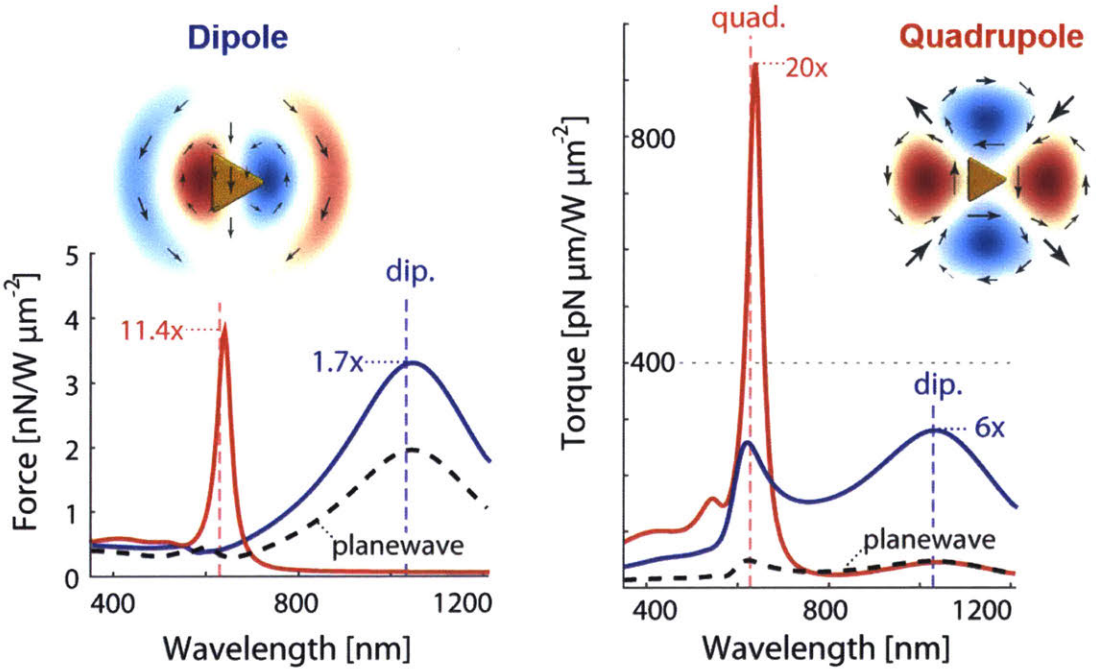

Figure 3.3.5: Comparison between force and torque optimization at dipole (blue) and quadrupole (red) modes. Left inset shows dipole field illustration with relatively higher center intensity, and right inset shows quadrupole field illustration with higher angular momentum.

distinguish the impact of the change in resonant field pattern from the change in the resonance lifetime. Controlling for the change in lifetime, we found that torque seems to favor higher-order (*e.g.*, quadrupole) resonances with greater angular momentum, while force (F_z), which closely correlates with extinction power, seems to favor lower-order (*e.g.*, dipole) resonance with greater field intensity within the particle. This is further shown in Figure 3.3.5. With the use of structured illumination, higher-order resonances can be excited more effectively, which contributes to higher optical torque after optimization.

Our numerical optimization framework allows a systematic search of the illumination-field design space to maximize force or torque on lossy, non-spherical particles with multipolar scattering channels. In addition, we think a rigorous analytical study of the fundamental upper bounds on opto-mechanical responses, similar to the analysis performed on light extinction [11, 130], would be useful in the future.

3.3.3 Robustness of Optimization

Experimental generation of the designed illumination via SLMs may suffer various types of manufacturing errors [131]. Figure 3.3.6 shows the tradeoff between enhancement and robustness to experimental errors. The fractional error is added to the beam using

$$\mathbf{E}_w = \sum_{i=0}^{m} (a_i + \delta_{ai})\mathbf{M}_i + (b_i + \delta_{bi})\mathbf{N}_i, \quad (|\delta| \leq w \cdot |a, b|_\infty), \tag{3.3.1}$$

where δ is a complex-valued random error bounded by the magnitude of the largest coefficient multiplied by the fractional weight $0 \leq w \leq 1$. Figure 3.3.6 shows the decrease in FOM_T as a function of w. At λ_{dip}, increasing w from 1% to 10% decreased the best FOM from 0.994 to 0.517, and the median FOM followed a similar trend. On the other hand, FOM_T of the best optimized field at λ_{quad} dropped from 8.624 to 1.433, and the median optimized field changed from 3.92 to 3.237. Figure 3.3.6 demonstrates a clear tradeoff between field enhancement and error tolerance, as one might expect due to the need to couple strongly to the underlying particle resonances. For the tolerance requirements of a given experimental setup, the approach we outline here could easily be adapted to a robust-optimization framework [132, 133] in which the expected variability is included and optimized against.

3.4 Conclusion

We present a numerical framework for computer optimization of structured illumination that maximizes optical force or torque on arbitrary scatterers, and show a 20-fold enhancement in optical torque per intensity on an example plasmonic nanoparticle, compared to a circularly polarized planewave. Previously, the major bottleneck has been the cumbersome computation. We overcome this bottleneck with a compact cylindrical Bessel basis and a fast boundary element method. We are optimistic that such computational framework for 3D vector fields can be generalized and applied to other design problems in opto-mechanics, nanophotonics, and 3D imaging.

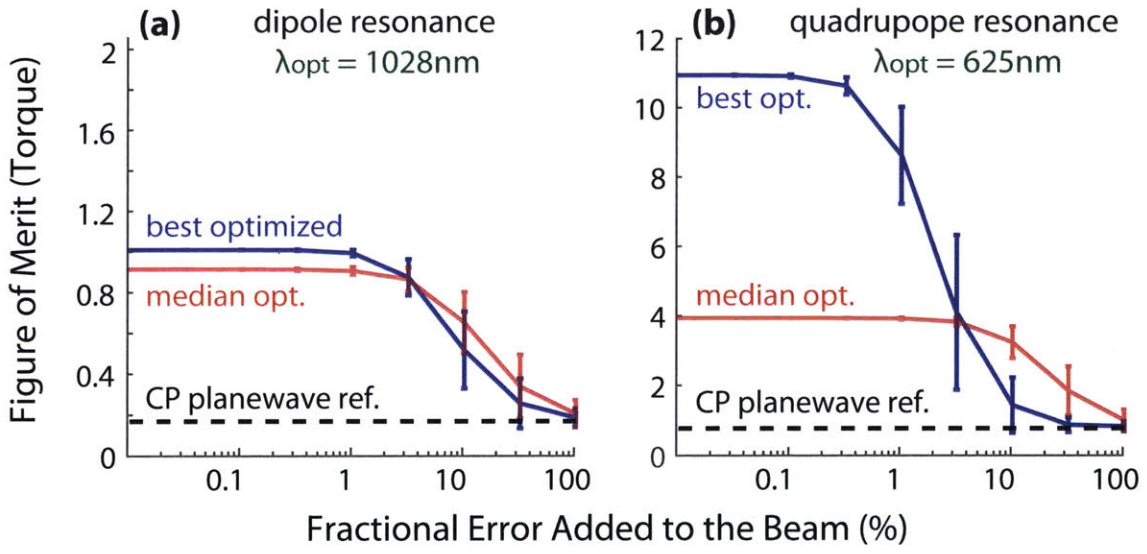

Figure 3.3.6: Robustness of the optimized incident fields, quantified by the decrease in FOM_T with respect to fractional random error added to the best (blue) and the median (red) optimized fields, at λ_{dip} (right) and λ_{quad} (left). The error bar represents the standard deviation for 100 samples.

Part II

Dissipative Periodic Structures for Optics and Acoustics

Chapter 4

Numerical Parameter Study for a Metallic-Dielectric Photonic Crystal (MDPhC) Broadband Solar Absorber

This chapter is based on the FDTD simulation results presented in: J. B. Chou, Y. X. Yeng, Y. E. Lee, A. Lenert, V. Rinnerbauer, I. Celanovic, M. Soljačić, N. X. Fang, E. N. Wang, and S.-G. Kim, "Enabling Ideal Selective Solar Absorption with 2D Metallic Dielectric Photonic Crystals," Advanced Materials, Vol. 26 (2014).

4.1 Introduction

The field of photonic crystals for electromagnetic waves has been widely investigated over the past three decades [134, 135, 136, 137, 138, 139]. Photonic crystals are periodic structures that mimic the properties of semiconductors to guide and trap light [12], configured so that electromagnetic wave propagation is suppressed for certain frequency bands due to destructive Bragg scattering. The concept of photonic crystals has been applied to a variety of engineering applications, such as waveguiding [140, 141, 142, 143], control of quantum emission and lasing [144, 145, 146], slow light [147, 148, 149], negative refraction [150, 151], nanoscale thermal control [136, 137, 138], and quantum information processing [152]. Periodicity L for photonic crystal structures

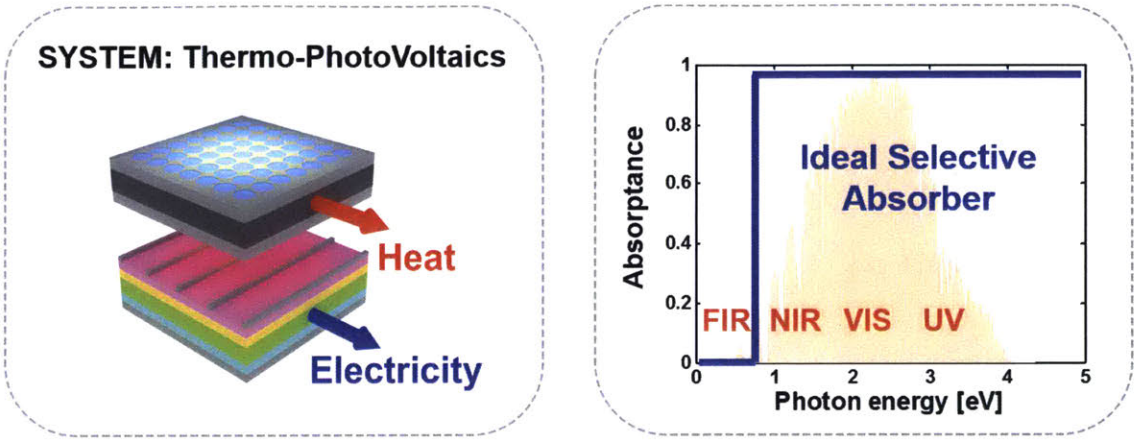

Figure 4.1.1: Left: A simplified schematic of a solar-thermophotovoltaic (STPV) system. The absorber layer (top) selectively absorbs the useful portion of the solar spectrum and emits it to the photo-voltaic cell (bottom). Right: the absorption spectrum of an ideal high-pass selective absorber (blue) is plotted on the solar spectrum (light pink filled). The low-energy far-infrared portion is totally reflected, while useful near-infrared, visible, and ultraviolet are totally absorbed.

typically ranges from hundreds of microns down to a tens of nanometers.

Researchers have explored a variety of material geometries for selective solar absorption [153]. Recent developments of metal based selective absorbers have demonstrated 1D, 2D, and 3D metallic photonic crystal structures capable of tailoring the absorption spectrum [136, 137, 154, 155, 156, 157, 158, 159, 160, 161, 162, 163, 164]. In addition to a desirable optical response, a good receiving surface of a STPV system needs high temperature reliability, omnidirectional absorption, and wafer-scale fabrication for mass scalability [165, 166, 167, 168].

In this chapter, we discuss the optical response of a metallic-dielectric photonic crystal (MDPhC). Micro-cavity photonic crystal structures have been previously developed by the group of Dr. Ivan Celanovic, Prof. Marin Soljačić, and Prof. John Joannopoulos [161, 165]. Subsequently, metal-dielectric and metal-semiconductor photonic crystal structures were developed and improved by Prof. Sang-Gook Kim's group [169, 167, 170]. The MDPhC serves as the receiving surface of a solar-thermophotovoltaic (STPV) energy conversion system [156, 161, 160, 135, 171] that converts sunlight into heat and electricity. As shown in Figure 4.1.1, we want to engineer a clear high-pass cutoff in the absorptance spectrum that selectively filters

out the low-energy photons below the cutoff frequency.

4.2 Method

FDTD Simulation and Material Modeling

Finite-difference time-domain (FDTD) simulations are performed to study the influence of the geometric parameters in Figure 4.2.1(b). As in Chapter 2, a commercial-grade FDTD solver was used to perform 3D discretization of the multi-material unit cell [28].

A Drude-Lorentz model of the metal was obtained by fitting room temperature measured reflection spectra of metallic Ru, deposited with atomic layer deposition (ALD). The dielectric $HfO_2$was modeled with a complex permittivity based on the measured HfO_2 sample, with a long wavelength index of $n=2.04$. Absorption in the HfO_2 was experimentally measured to be zero for photon energies 4.96 eV and below. The absorption spectra were simulated with a linear polarization plane wave at normal incidence. The Al_2O_3 was modeled as a lossless dielectric with refractive index $n=1.5$.

Optical Characterization

An ultraviolet-visible-near infrared (UV-VIS-NIR) spectrometer (Cary 500i) with spherical diffuse reflectance measurement accessory was used to measure the total absolute absorption spectra of the MDPhC, MAPhC, and flat Ru at an incidence of 3° with unpolarized light. For absorption measurements at infrared photon energies, a fourier transform infrared (FTIR) spectrometer was used with a commercial aluminium coated reference mirror.

We measure the absolute reflection using a commercial diffuse reference (Labsphere diffuse reflectance standard) with a readily known reflection spectrum. The FTIR spectrometer was used to measure the specular reflection from the wavelength range 1μm to 4μm. A commercial reference aluminum coated mirror (Thorlabs) was used as the reference with a readily known reflection spectrum at angles 30°, 45°, 50°, 60°,

and 70°. We used an unpolarized broadband optical source for all measurements.

Summary of Fabrication

The wafer-scale nanofabrication process for the experimental MDPhC sample in Figures 4.2.1(c)-4.2.1(f) is explained in detail in [168]. The entire fabrication has been performed by Dr. Jeff Chou in Prof. Sang-Gook Kim's group; my contribution was to set up and perform FDTD simulations, and assist in optical spectroscopy characterizations of the fabricated samples.

Here the fabrication steps are summarized briefly. The multilayered structure was fabricated using the sidewall lithography technique across a six inch wafer [172, 173, 174]; then a 80nm metal layer of ruthenium (Ru) was deposited with atomic layer deposition (ALD) for conformal deposition purposes. The dielectric filling of HfO_2 is also deposited via ALD, and excess HfO_2 is removed via chemical mechanical polishing (CMP). A layer of HfO_2 with a thickness of approximately t=25nm is left on top of the entire structure. HfO_2 is chosen due to its conformal deposition, high melting temperature, and transparency in the visible and infrared (IR) regime. Cross-sectional SEM images are obtained via focused ion beam (FIB) milling. The fabricated structure has been further developed and explored for other applications such as water splitting [175, 176, 177].

4.3 Results and Discussion

The wafer-scale fabricated MDPhC has a measured absorption of 85% for photon energies 0.7eV$<\hbar\omega<$5eV and an absorption below 10% for $\hbar\omega<$0.4eV. Angled measurements show existence of the cavity modes for angles up to 70° from normal. Furnace tests at 1000°C for 24 hours show a robust optical performance due to its fully encapsulated design which helps to retain the metal cavity shapes at high temperatures [169].

The MDPhC utilizes cut-off frequencies of cavity modes to tailor the absorption. Since the cut-off frequency is dependent on the geometry of the cavities, the absorption

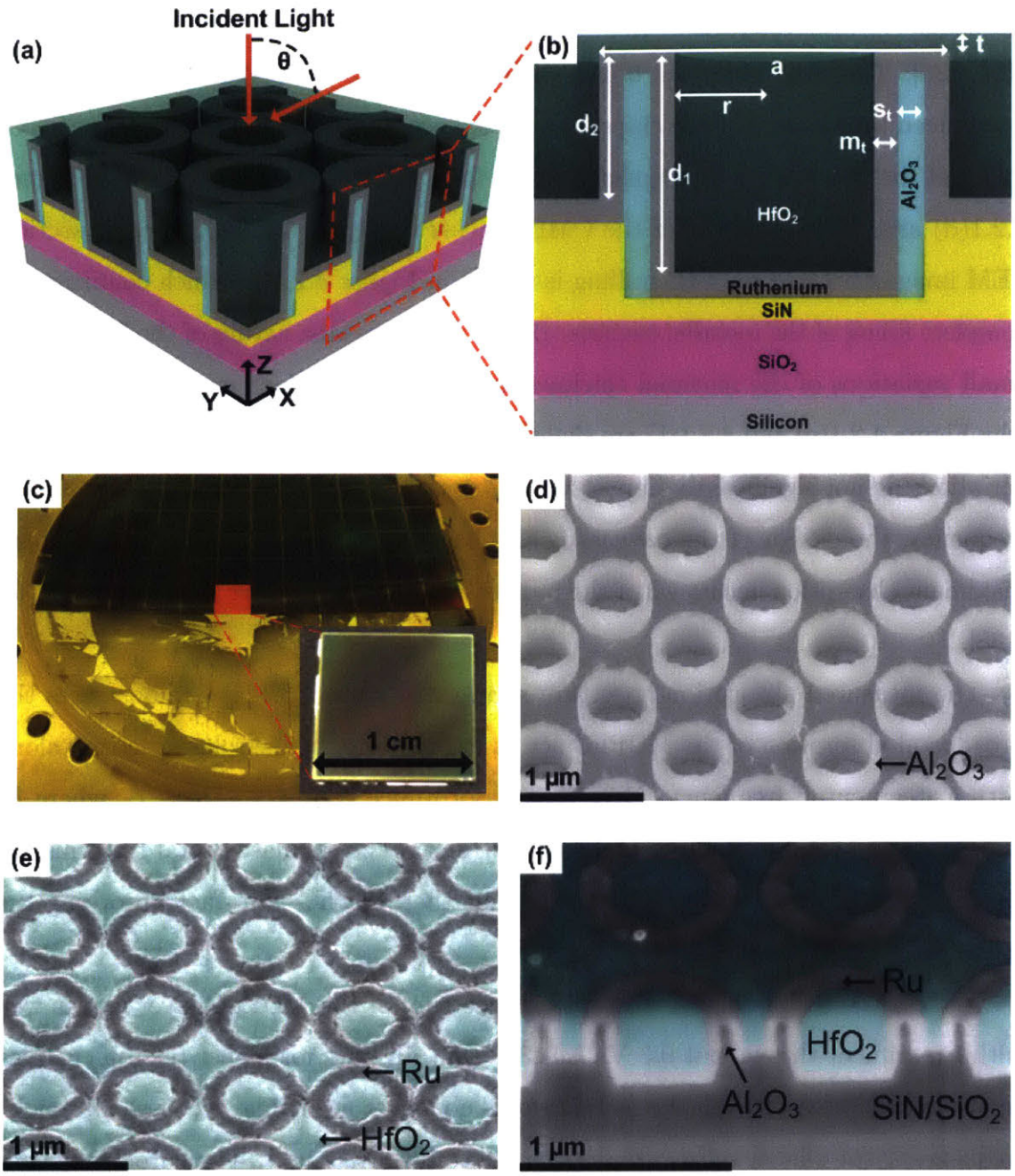

Figure 4.2.1: MDPhC images. (a) Schematic diagram of the MDPhC. (b) Schematic of the cross-section of the MDPhC with period a, cavity radius r, inner and outer cavity depths d_1, d_2, metal thickness m_t, Al_2O_3 thickness s_t, and thin-film antireflection coating thickness t. Measured dimensions are a=790nm, r=200nm, d_1=200nm, m_t=80nm, s_t=40nm, and t is estimated to be $t \approx 25$nm. HfO_2 is colored semi-transparent blue for clarity. (c) Photo of the fully fabricated 6 inch wafer. (d) SEM image of the 40 nm thick Al_2O_3 shells before metallization. (e) SEM image of the fully fabricated wafer surface, cut into 1cm×1cm squares. (f) SEM image of the sample cross-section taken at a 42° cut angle.

spectrum can be tuned by simply modifying the radius and depth of the cavities [161, 138]. The fully fabricated 6 inch wafer is shown in Figure 4.2.1(c), where it has been diced into 1 cm $\times$ 1 cm chips. An angled scanning electron microscope (SEM) image of the 70 nm thick Al_2O_3 shells before the metal is deposited is shown in Figure 4.2.1(d) and of the wafer after the CMP process in Figure 4.2.1(e). A cross section SEM image obtained via FIB milling is shown in Figure 4.2.1(f) which confirms the complete filling of the metallic cavities. Due to the large area nature of the fabrication, small variations of the material thicknesses are observed which explains the reason why Figure 4.2.1(e) and 4.2.1(f) are slightly different, however we find that these small variations do not significantly impact the absorption spectrum. Along with the cut-off frequency, the design of the cavities is also based on Q-matching formalism where maximum absorption occurs when the radiative and the absorptive Q values are equal [138].

The measured absorption spectrum shown in Figure 4.3.1(a) demonstrates the broadband absorption of the MDPhC across the majority of the solar spectrum along with a steep cutoff frequency. Note that absorptance is $\alpha_t = 1 - R_t - T_t$, where R_t and T_t are the total reflectance and transmittance. The simulated total transmission through the MDPhC is shown to verify that the MDPhC is in fact absorbing the majority of the input light.

In 4.3.1(a), the simulated absorption spectrum of the MDPhC layer agrees well with experiment throughout 0.3eV$<\hbar\omega<$3eV, but diverges for higher photon energies, where transmission through the metal layer is no longer negligible. At these ultraviolet frequencies, the silicon substrate absorbs the transmitted light. The cutoff frequency is located at mode M1 with $\hbar\omega$ =0.75eV. For infrared photon energies under 0.4eV, absorption is successfully supressed to be below 10%.

In comparison, the measured MAPhC spectrum is shown in Figure 4.3.1(b), which has a poorer absorption profile over the visible frequencies due to diffraction losses [161, 167]. The MAPhC has the same dimensions as the MDPhC, however the MAPhC does not have the HfO_2 filling. The cut-off frequency for the MAPhC shifted by a factor of 2.07 to 1.55 eV, which closely matches the measured index of the HfO_2 in

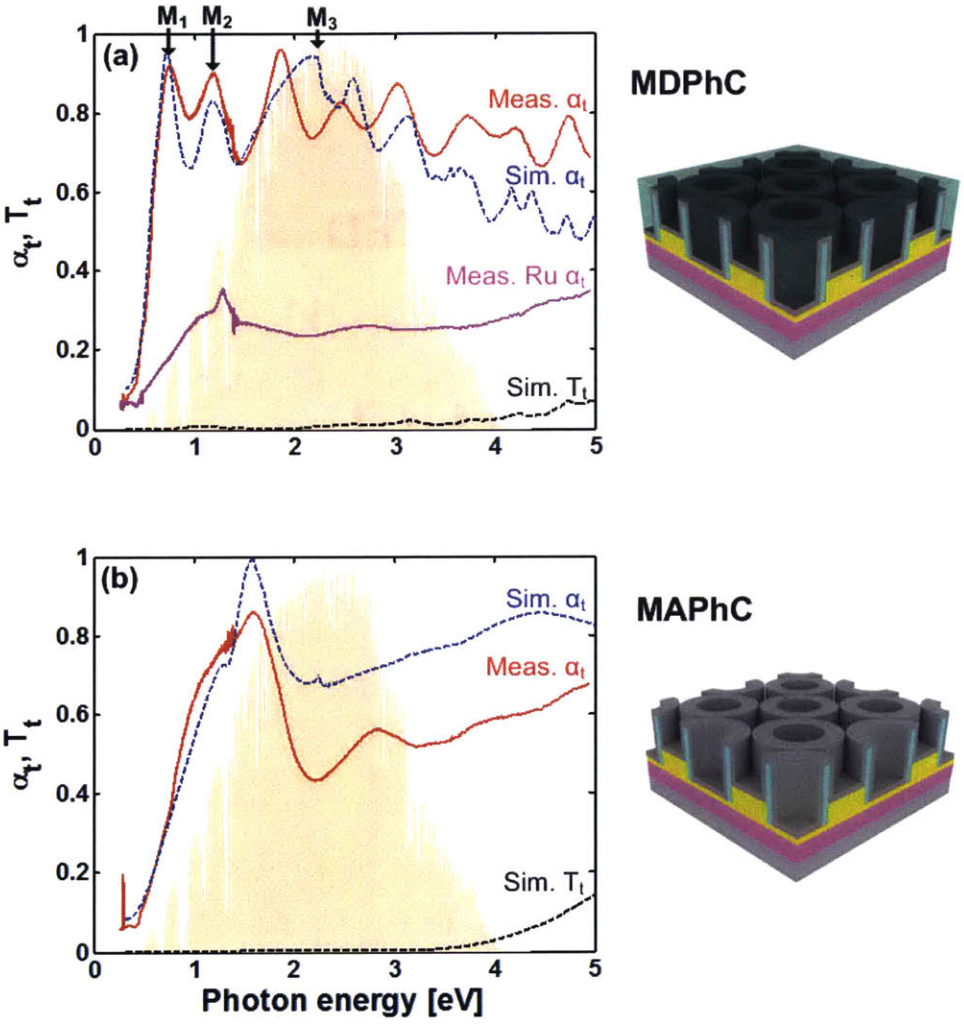

Figure 4.3.1: Measured (red) and simulated (blue dotted) absorption spectra for (a) dielectric-filled and (b) air-filled photonic crystals. An absorption measurement for flat metal (pink) is shown for reference. The first three modes of the simulated spectrum are labeled as M1, M2, and M3, respectively. The experimental measurements are provided by Dr. Jeff Chou.

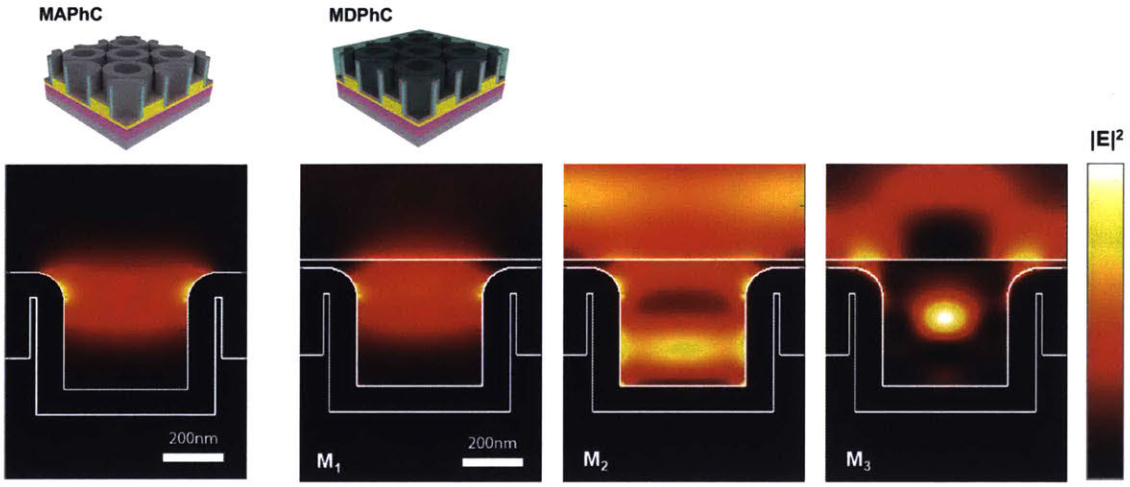

Figure 4.3.2: Simulated $|\mathbf{E}|^2$ field images for MDPhC and MAPhC absorptance peaks. Left: The MAPhC field image shows a standard cavity mode, which corresponds to the single peak in Figure 4.3.1(b). Right: The MDPhC field images correspond to M1, M2, and M3 in Figure 4.3.1(a).

the cavity. The FDTD simulated MAPhC absorption is also shown which agrees well in frequency, but has higher absorption values than measured. Mismatch between the simulation and experiment may be attributed to both the smooth cylindrical structure and perfect uniform geometry in the simulation that are not present in the actual device due to the large scale fabrication variation.

The broadband optical properties of the MDPhC in the visible regime are due to the combination of a high density of cavity modes and a thin-film coating layer. The dielectric filling essentially red-shifts the frequencies of the high order cavity modes to create a high density of states in the visible regime. Experimentally, this can be observed in the larger number of peaks in the measured MDPhC absorption spectrum in comparison to the MAPhC absorption spectrum in Figure 4.3.1. The first two modes, M1 and M2, are standard cavity modes, however, M3 ($\hbar\omega$ =2.21eV, $\lambda_3 = 560$nm) and higher-order modes support a hybrid cavity and surface plasmon polariton (SPP) mode.

The simulated E_x field images are shown in Figure 4.3.3 for the first five modes. The first two modes are standard cavity modes with to coupling to SPP modes. M3 and M4 show both cavity and SPP modes, where the SPP modes are propagating

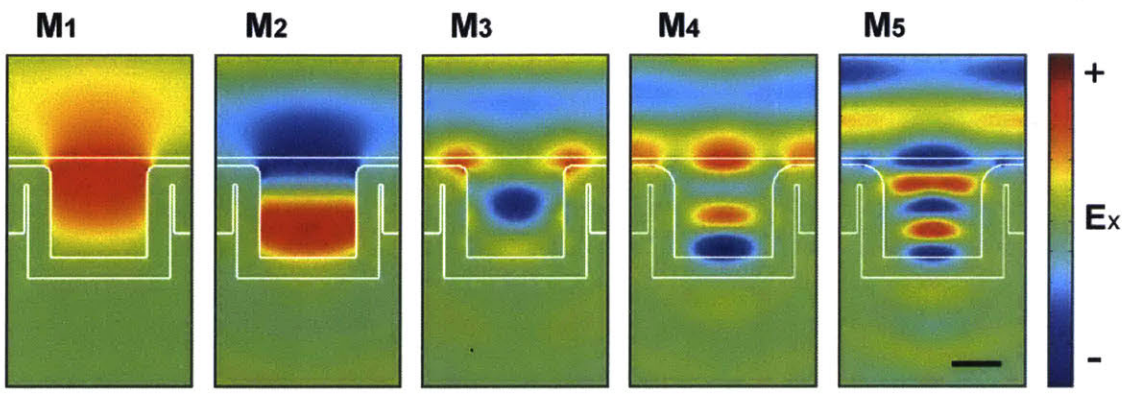

Figure 4.3.3: Simulated E_x field images of the first five modes in the MDPhC absorption spectrum. M1 and M2 are standard cavity modes with no coupling to SPP modes. M3, M4, and M5 are coupled cavity-SPP modes at peak photon energies $\hbar\omega = 2.21$eV, 2.55eV, and 3.17eV, respectively. Scalebar is 200nm.

along the vertical sidewalls of the cavity. M5 shows a high order cavity mode with little coupling to SPP modes. The higher order modes appear to be dominated by cavity modes and are what cause the high density of optical states in the visible regime. The coupling between cavity and SPP modes may also contribute to the increased absorption in the M3 mode [178].

The effect of metal thickness on the absorption spectrum of the MDPhC is shown in Figure 4.3.4, where the thicknesses of both metal (m_t) and Al_2O_3 (s_t) are varied to keep the inner radius r constant. For m_t greater than the skin depth, the absorption spectra remains relatively constant. In this regime, the thickness of the Al_2O_3 has no impact on the absorption spectra since the fields do not significantly penetrate the metal. Once the metal thickness is below the skin depth, as shown for , the transmission of the fields through the metal lowers the absorption spectra. In this regime, the thickness of the Al_2O_3 can alter the absorption spectra by allowing for modes within the Al_2O_3 to occur. However, the fabricated MDPhC presented in this communication has metal thickness greater than the skin depth, and as a result the Al_2O_3 thickness has little effect on the absorption spectrum. Therefore, although the Al_2O_3 thickness varies across the wafer by approximately 40 nm - 80 nm, due to non-uniform deposition and etching processes, this variation does not impact the absorption spectrum. Furthermore, variations in the metal thickness across the wafer

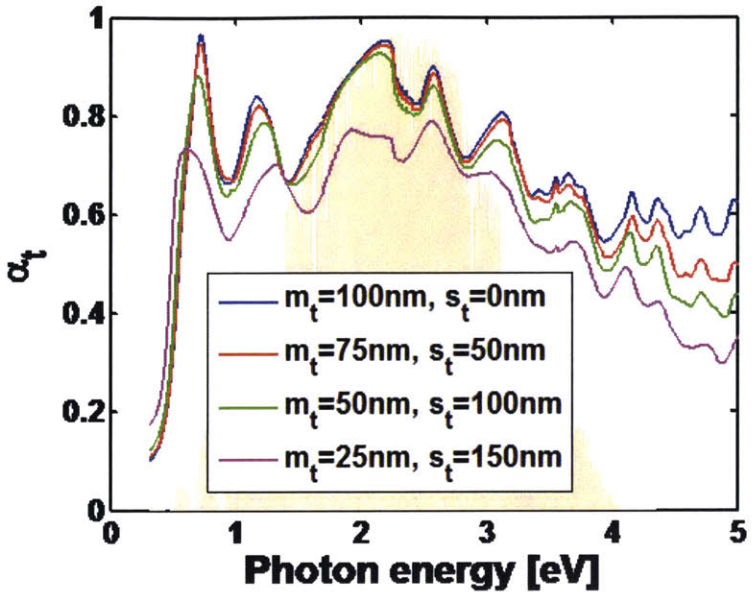

Figure 4.3.4: Simulated absorption spectra with varying metal thickness m_t, and Al_2O_3 thickness s_t. The inner radius r is held constant. Note that for m_t greater than the plasmonic skin depth, variations in both m_t and s_t have little impact on the absorption spectrum.

also do not have a significant impact on the absorption spectrum, since the minimum observed metal thicknesses is approximately 70 nm. In summary, as long as the metal thickness is greater than the skin depth, the absorption spectra is immune to small variations in metal or Al_2O_3 thicknesses. We comment that this analysis assumes that the inner radius, r, remains constant. If variations of the metal or Al_2O_3 thickness change the inner radius, r, then the frequency of the modes will red shift or blue shift depending on the direction of the change in r.

Figure 4.3.5 specifies the influence of a thin-film coating layer that suppresses reflection and tunes higher-order resonances to enhance absorption near the peak of the solar spectrum. A thin-film coating layer serves to minimize reflection at the top surface of the MDPhC by tuning the cavity-SPP hybrid resonance modes. Analytically, the thin film layer on a flat HfO_2 and ruthenium interface can be calculated by inserting the complex permittivity of the metal layer $\varepsilon_{\mathrm{Ru}}$ into the Fresnel reflection equation [179]. To suppress undesired reflection in the visible spectrum of $1.55\mathrm{eV}<\hbar\omega<3.1\mathrm{eV}$, with an average index of HfO_2 at in the visible regime of $n = 2.09$, we calculate thin

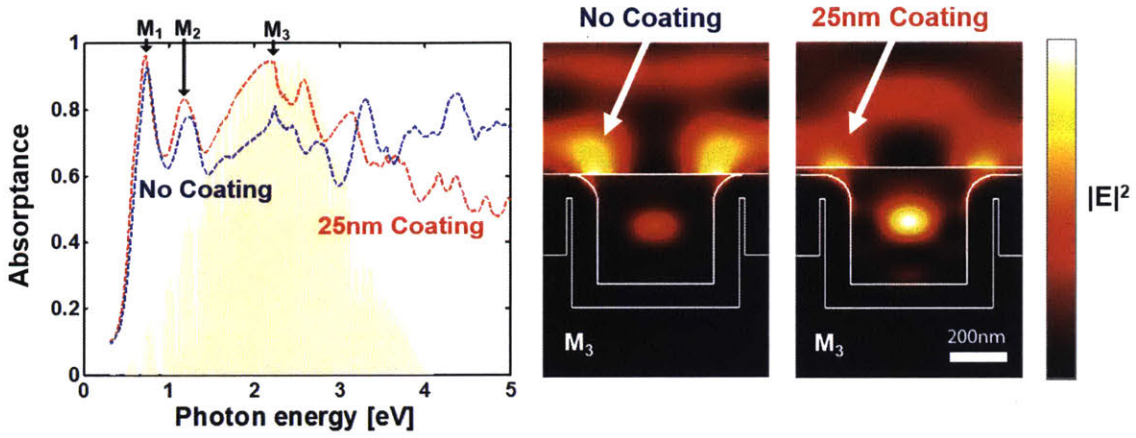

Figure 4.3.5: Simulated absorption spectra comparing MDPhCs with (red) and without (blue) thin-film coating. Corresponding electric field intensity profiles of M3 mode are shown on the right.

film layer thickness of 22nm to 75nm for a flat surface. Thus, if the proper thin-film antireflection coating layer thickness is designed to spectrally overlap with the high density of optical states, high, broadband absorption will occur.

Specifically, coupling into modes within infrared and visible photon energies are increased, most notably around M3, and higher-energy modes in the ultraviolet are suppressed. Figure 4.3.5 also shows the intensity plots of the M3 mode with and without the 25nm coating. We observe a clear reduction in the reflected intensity at the top metal surface, marked with white arrows due to destructive interference. Furthermore, integration of the FDTD simulated Poynting vector reveals that the thin-film coating layer causes 44% of the incident light power to be absorbed at the top metal surface for mode M3, whereas without an thin-film antireflection coating layer only 33% is absorbed.

4.4 Conclusion

This chapter summarizes the FDTD numerical analysis for a broadband solar absorber developed and described in [168]. The surface of a solar panel can be intricately patterned and coated to receive as much sunlight as possible from all directions with

minimal reflection. Through numerical parameter-studies, we discuss the tunability and spectrum-selectivity of the MDPhC optical response. We analyze that the broadband absorption is due to a high density of optical cavity modes overlapped with surface plasmon polariton modes, and highlight the importance of the thin film coating layer in tuning the hybrid resonances. The MDPhC structure may be designed with various alternative metals and dielectrics to suit any application's needs. With further optimization of the structure and materials, MDPhCs could play a critical role in the future of solar energy conversion.

Chapter 5

Nonlocal Dynamics of Dissipative Phononic Crystals

This chapter is based on: N. Nemati, Y. E. Lee, D. Lafarge, A. Duclos, and N. X. Fang, "Nonlocal dynamics of dissipative phononic fluids," Phys. Rev. B., Accepted for publication on 10 May 2017.

5.1 Introduction

The field of phononic crystals for acoustic and elastic waves [180, 181], analogous to photonic crystals for electromagnetic waves discussed in Chapter 4, has been widely investigated over the past two decades [182, 183, 184, 185]. Phononic crystals are periodic arrangement of inclusions embedded in a host material, configured so that mechanical wave propagation is suppressed for certain frequency bands due to destructive Bragg scattering. The inclusion and the host can be made of fluid or solid materials. The concept of phononic crystals has been applied to a variety of engineering applications, including sound isolation [186, 187, 188, 185], wave guiding [189, 182], nanoscale thermal control [184], and quantum information processing [190]. Depending on the structural size, phononic crystals can be engineered in audible frequencies (kHz) for sound proofing, to ultrasonic imaging (MHz), hypersound (GHz) in optomechanics, and thermal applications (THz) [184]. Periodicity L can range from

a few centimeters down to nanometers.

On the other hand, semi-periodic acoustic metamaterials support local resonances that influence the phase velocity of the wave, resulting in one or more negative effective medium parameters such as density ρ, compressibility χ, and elastic modulus Y. For acoustic metamaterials, λ is often several times larger than unit length L, and the design of unconventional material properties require an approproiate effective-medium theory.

Effective-medium theories aim at establishing simple macroscale equations that govern the effective dynamics of a composite medium on the scale of λ, which is greater than the characteristic length scale of the microstructure within the unit cell. Microscale information such as micro-topology, density and compressibilities of each constituent medium, and volume fraction of the inclusion are collectively encoded in a few effective parameters on the macroscale, where the medium is assumed to be homogeneous. These macroscale equations describe the field propagation and the constitutive relations for effective material properties such as effective density and compressibility.

Describing the effective properties of phononic crystals and acoustic metamaterials is generally restrictive: The long-wavelength resonant behaviors of acoustic metamaterials are often not captured, and the Bragg scattering in phononic crystals is commonly thought to escape a macroscopic description. Efforts have been made to capture local resonances in acoustic metamaterials with elastic materials by coherent potential approximation [191] that is based on minimizing scatterings in the long-wavelength limit. An improved scheme has been developed to obtain the effective properties of the same type of materials in a broader frequency-band, by matching the lowest-order scattering amplitudes that arise from the unit cell, with that of the homogenized material (metasolid) [45].

Nonlocal homogenization approaches were formulated to derive broadband effective electromagnetic parameters, by averaging the response of an appropriate distribution of sources [43], or by using coherent potential approximation method in the long-wavelength regime [192]. Although nonlocal effects in electromagnetic materials have

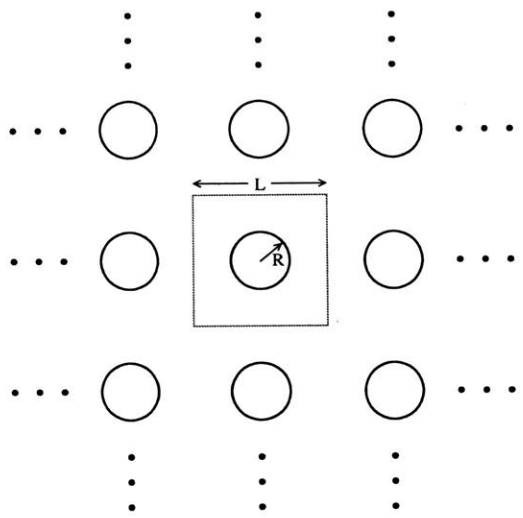

Figure 5.1.1: Schematic of a two-dimensional phononic crystal. Rigid cylinders are periodically embedded in a viscothermal fluid medium (*e.g.*, air).

usually been treated as a small correction needed when λ is small, these effects have been observed in the long-wavength regime as well, for both electromagnetic [48] and acoustic [193] metamaterials.

Here, we study the special case of heterogeneous two-phase media with a motionless non-deformable solid and a viscothermal fluid. The medium forms a connected fluid phase which supports wave propagation. In the long wavelength limit $\lambda \gg L$, the standard approach to compute its effective properties is based on the two-scale asymptotic method. We refer to this approach as the "local theory" [194, Appendix A] because the theory assumes no spatial dispersion [195, 196]. But local approach cannot describe the behavior of subwavelength composites that exhibit wavevector-dependent response. The local approach has been extended to describe fluid/solid media with Helmholtz structures, but at the cost of separating the fluid region into different portions, in which different asymptotic expansions and rescaling are performed [197, 193]. Such limited approaches cannot be generalized to more complex geometries. Furthermore, because the long-wavelength condition must be satisfied, the local approach fails to describe Bragg scattering in phononic crystals.

Therefore it is desirable to devise a macroscopic theory that allows for not only temporal but also spatial dispersion, which is generally applicable regardless of the

geometry and wavelength. This has been achieved by Lafarge and Nemati [51, 198] using an analogy with Maxwell's equation and nonlocal constitutive equations for electromagnetic waves. For solid/solid stationary-random composites or periodic random media, a general nonlocal form of the macroscopic equations has been proposed by Willis. [199] Within the same effective-medium formulation, effective parameters have been calculated by different techniques, in 1D [200], 2D [201], and 3D [202, 44]. Our nonlocal description of fluid/rigid media that we discuss here involves equations of the same form as those of Willis, but without the coupling terms. The absence of these coupling terms is due to the different ways of defining the macroscopic fields from microscopic fields, although both schemes have non-asymptotic character and employ ensemble-averaging concept.

We describe the 1D nonlocal dynamics of phononic crystals composed of two-dimensional periodic array of rigid cylinders in air (Figure 5.1.1), using the macroscopic equations of the nonlocal theory with an action-response homogenization method. We demonstrate that the nonlocal approach enables us to characterize the material through a complex density and compressibility of an effective fluid in a broadband regime including the high-frequency range $\lambda \simeq L$. We refer to this effective fluid as a *phononic fluid,* in contrast to metafluids, whose properties are based on local resonances. The validity and precision of the calculations are verified by comparing the results with a reference obtained using multiple scattering method incorporating viscothermal losses. To our knowledge, this is the first time that a dissipative phononic (sonic) crystal is precisely characterized by its effective properties in a large frequency range extending over Bragg's regime covering the entire first and second Brillouin zones. This is a breakthrough step towards bridging the macroscale and te microscale.

Sec. 5.2.1 recalls the microscopic governing equations for linear acoustics. Sec. 5.2.3 presents the local and nonlocal approaches of the macroscopic theory in a unified formulation. Sec. 5.2.4 and Sec. 5.2.5 review the action-response problems to achieve the effective-medium parameters for local and nonlocal computation, respectively. The multiple scattering method used as a reference is summarized in Appendix C. The results are presented in Sec. 5.4 and concluded in Sec. 5.5.

5.2 Theory

5.2.1 Microscopic Equations

In a heterogeneous rigid-boundary system, as the phononic crystal represented in Figure 5.1.1, the governing equations consist of bulk-fluid equations and boundary conditions. On the microscopic scale, the linear equations governing the dynamics of small-amplitude disturbances in a homogeneous viscothermal fluid come from linearized balance equations of mass, momentum and energy; the constitutive relations; and a general state equation of the fluid.

These governing equations describe the small deviations of thermodynamic pressure p, density ρ, temperature T, velocity $\boldsymbol{v}$, and entropy s, from their rest state p_0, ρ_0, T_0, $\boldsymbol{v}_0 = 0$, and s_0, up to the terms of first order. In the framework of classical irreversible thermodynamics [203, 204], the two constitutive relations are those of Stokes and Fourier.

$$\sigma'_{ij} = 2\eta\left(e_{ij} - \frac{1}{3}(\boldsymbol{\nabla}.\boldsymbol{v})\delta_{ij}\right) + \zeta(\boldsymbol{\nabla}.\boldsymbol{v})\delta_{ij} \tag{5.2.1a}$$

$$\boldsymbol{q} = -\kappa\boldsymbol{\nabla}T \tag{5.2.1b}$$

Stokes's law is a linear isotropic relation between the components of the viscous shear stress σ'_{ij}, and strain rate $e_{ij} = \frac{1}{2}(\partial_i v_j + \partial_j v_i)$, where δ_{ij} is the Kronecker symbol; and η and ζ are the first and second viscosity of the fluid. The Fourier's law of heat conduction is a corresponding relation between the heat flow $\boldsymbol{q}$ and the temperature gradient, with the coefficient of thermal conductivity κ.

Using Stokes's law of Eq. (5.2.1a), the conservation equations of mass, and momentum in the bulk fluid $\mathcal{V}^f$ for a fluid particle yields [30, 4]:

$$\frac{\partial b}{\partial t} + \boldsymbol{\nabla}\cdot\boldsymbol{v} = 0 \tag{5.2.2a}$$

$$\rho_0\frac{\partial \boldsymbol{v}}{\partial t} = -\boldsymbol{\nabla}p + \eta\boldsymbol{\nabla}^2\boldsymbol{v} + \left(\zeta + \frac{1}{3}\eta\right)\boldsymbol{\nabla}\left(\boldsymbol{\nabla}\cdot\boldsymbol{v}\right) \tag{5.2.2b}$$

where b is defined as $b \equiv \rho'/\rho_0$ and ρ' the density deviation. For convenience, we

denote the pressure deviation as well as the absolute pressure, by p.

We expand the thermodynamic equations of state $\rho = \rho(p, s)$ and $T = T(p, s)$ near the rest state up to the first term, using the following thermodynamic identities: $(\partial\rho/\partial s)_p = -\rho_0\beta_0/c_p$; $(\partial T/\partial p)^s = \beta_0 T_0/\rho_0 c_p$; $c_0^2 \equiv (\partial p/\partial\rho)^s$, where c_0 represents the adiabatic sound speed; where $\beta_0 \equiv \rho_0[\partial(1/\rho)/\partial T]_p$ and $c_p \equiv T_0(\partial s/\partial T)_p$ are the coefficient of thermal expansion and the specific heat at constant pressure evaluated at the fluid rest sate. Then we can write the state equations as the following.

$$\begin{aligned} \rho' &= (1/c_0^2)p - (\rho_0\beta_0 T_0/c_p)s' \\ T' &= (T_0\beta_0/\rho_0 c_p)p' + (T_0/c_p)s' \end{aligned} \tag{5.2.3}$$

Omitting s' in the latter equations leads to:

$$\gamma\chi_0 p = b + \beta_0\tau, \tag{5.2.4}$$

where $\chi_0 \equiv \rho_0^{-1}(\partial\rho/\partial p)^s$ is the coefficient of adiabatic compressibility at rest state, $\gamma \equiv c_p/c_v$ the relative specific heats at constant pressure and constant volume involved in the thermodynamic identity $\gamma - 1 = \beta_0^2 T_0/\rho_0 c_p$, and τ is a simpler notation for the excess temperature T'.

The linearized energy balance equation is reduced to the linear heat transfer equation [30, 4],

$$\rho_0 T_0 \frac{\partial s'}{\partial t} = \kappa\boldsymbol{\nabla}^2\tau, \tag{5.2.5}$$

which expresses the heat gained per unit volume using Fourier's law in Eq. (5.2.1b). Combining Eqs. (5.2.3) and (5.2.5) gives the following form of energy balance equation,

$$\rho_0 c_p \frac{\partial\tau}{\partial t} = \beta_0 T_0 \frac{\partial p}{\partial t} + \kappa\boldsymbol{\nabla}^2\tau, \tag{5.2.6}$$

which complements the governing equations in the bulk fluid Eqs. (5.2.2)-(5.2.4).

In the rigid solid region $\mathcal{V}^s$, energy balance equation is reduced to

$$\rho^s c_p^s \frac{\partial \tau^s}{\partial t} = \kappa^s \boldsymbol{\nabla}^2 \tau^s,$$

where ρ^s is the constant solid density, τ^s solid excess temperature, and κ^s solid coefficient of thermal conductivity.

On the fluid/solid interface $\partial\mathcal{V}$, we have the conditions of continuity of the excess temperature $\tau = \tau^s$ and the heat flux $\kappa\boldsymbol{\nabla}\tau = \kappa^s\boldsymbol{\nabla}\tau^s$. The coefficient of thermal conductivity of the solid is much larger than that of the fluid $\kappa^s \gg \kappa$, and the heat capacity at constant pressure of the solid part is much larger than that of the fluid part, *i.e.*, $(1-\phi)\rho^s c_p^s \gg \phi\rho_0 c_p$, where ϕ is the fluid filling fraction (porosity). So we disregard the fluid excess temperature at the boundaries. In addition, we also assume no-slip boundary condition. The boundary conditions for the velocity and excess temperature on $\partial\mathcal{V}$ are:

$$\boldsymbol{v} = \mathbf{0}, \qquad \tau = 0. \tag{5.2.7}$$

The microscopic governing equations for the field variables $\boldsymbol{v}$, b, p and τ are: Eqs. (5.2.2), (5.2.4), and (5.2.6), with boundary condition Eq. (5.2.7).

5.2.2 Effective Medium Approaches: Overview

We summarize the local and nonlocal macroscopic acoustics associated with a given macroscopically homogeneous fluid/rigid random medium. Then the local and nonlocal action-response problems are stated, which determine the effective-medium parameters. We consider that the medium occupies the whole space and is assumed to be macroscopically homogeneous in ensemble-averaged sense. We imagine that we are given infinite number of samples $\boldsymbol{\omega}$ of the medium from a probability space $\boldsymbol{\Omega}$, the ensemble of which defines the homogeneous macroscopic medium. In each realization $\boldsymbol{\omega}$, the medium is composed of two regions: the void (pore) region $\mathcal{V}^f(\boldsymbol{\omega})$ which is a connected region permeated by the fluid, and the complementary solid-phase region

$\mathcal{V}^s(\boldsymbol{\omega})$. The pore-wall region or fluid/(rigid) solid interface is denoted by $\partial\mathcal{V}(\boldsymbol{\omega})$. The characteristic function of the pore region is defined by the following.

$$I(\boldsymbol{r};\boldsymbol{\omega}) = \begin{cases} 1 & \boldsymbol{r} \in \mathcal{V}^f(\boldsymbol{\omega}) \\ 0 & \boldsymbol{r} \in \mathcal{V}^s(\boldsymbol{\omega}) \end{cases} \tag{5.2.8}$$

Microscopically, the fields are of the form $a(t, \boldsymbol{r}; \boldsymbol{\omega})$, and the dynamics of the system is governed by Eqs. (5.2.2)-(5.2.7) with $\mathcal{V}^f$, $\mathcal{V}^s$ and $\mathcal{V}$ replaced by $\mathcal{V}^f(\boldsymbol{\omega})$, $\mathcal{V}^s(\boldsymbol{\omega})$ and $\mathcal{V}(\boldsymbol{\omega})$, respectively. The ensemble-average operation at position $\boldsymbol{r}$ is denoted equivalently by $\langle..\rangle(\boldsymbol{r})$ or $\langle..(\boldsymbol{r})\rangle$, that gives the expectation value of the micro-field at the same position. For instance, $\langle I\rangle(\boldsymbol{r}) \equiv \langle I(\boldsymbol{r})\rangle$ is the porosity ϕ, giving the probability that the position $\boldsymbol{r}$ lies in the fluid, over an infinite number of realizations. Since we assume the solid motionless and thermally inert, all microscopic fields $a(t, \boldsymbol{r}; \boldsymbol{\omega})$ that specify the fluid motion in $\mathcal{V}^f(\boldsymbol{\omega})$, are set to be zero in the solid $\mathcal{V}^s(\boldsymbol{\omega})$. The macroscopic mean $A(t, \boldsymbol{r})$ of the field $a(t, \boldsymbol{r}; \boldsymbol{\omega})$ is defined through $A(t, \boldsymbol{r}) = \langle a(t, \boldsymbol{r}; \boldsymbol{\omega})\rangle$.

The random phononic crystal is the ensemble of realizations obtained by random translation of this reference configuration in the x and y direction. Thus $\boldsymbol{\omega}$ can be regarded here as (ω_x, ω_y) with ω_x and ω_y random variables uniformly and independently distributed in $[-L/2,\ L/2]$. The characteristic function of the pore region is then interpreted as $I(\boldsymbol{r};\boldsymbol{\omega}) = I(\boldsymbol{r} - \boldsymbol{\omega}) = 1$ if $\boldsymbol{r} - \boldsymbol{\omega}$ is in the fluid region, and equals 0 if $\boldsymbol{r} - \boldsymbol{\omega}$ is in the solid region of the reference configuration.

We analyze acoustic waves propagating perpendicular to the cylinders in the direction of principal x-axis, connecting the nearest neighbors in the lattice whose unit vector is $\boldsymbol{e}_x$.

We present the macroscopic nonlocal computation; for the sake of comparison, we also present the macroscopic equations of local theory in a Maxwellian form. Also, ensemble-average concept is employed for both nonlocal and local schemes. For the local theory, it is equivalent and straightforward to consider only one period of the sample averaged over a unit cell. This applies also to the nonlocal theory, as long as the wavelengths remain sufficiently large.

5.2.3 Local and Nonlocal Macroscopic Equations

The macroscopic or effective-medium equations in local and nonlocal approaches include field equations that are general and valid for all media, and constitutive relations involving effective parameters. These equations are written in analogy to Maxwell equations in electrodynamics.

The macroscopic condensation and velocity are defined as the direct ensemble-averages $B = \langle b \rangle$ and $\boldsymbol{V} = \langle \boldsymbol{v} \rangle$, where $\boldsymbol{V} \equiv V\boldsymbol{e}_x$ is unidirectional.

Since the velocity vanishes on the cylinder walls, the following direct commutation relation between averaging and divergence operators holds: $\langle \boldsymbol{\nabla} \cdot \boldsymbol{v} \rangle = \boldsymbol{\nabla} \cdot \langle \boldsymbol{v} \rangle = \boldsymbol{\nabla} \cdot \boldsymbol{V} = \partial V / \partial x$. To clarify this, we replace a, $\boldsymbol{\nabla} a$, $a\boldsymbol{\nabla}$ and $\boldsymbol{n}(\boldsymbol{r}';\boldsymbol{\omega})a(t,\boldsymbol{r}';\boldsymbol{\omega})$, with $\boldsymbol{v}$, $\boldsymbol{\nabla} \cdot \boldsymbol{v}$, $\boldsymbol{v} \cdot \boldsymbol{\nabla}$ and $\boldsymbol{n}(\boldsymbol{r}';\boldsymbol{\omega}) \cdot \boldsymbol{v}(t,\boldsymbol{r}';\boldsymbol{\omega})$ in Eqs. (51)-(53) of reference [51]. Note that the commutation relation requires only that the normal component of the velocity vanishes on $\partial\mathcal{V}(\boldsymbol{\omega})$, thus it holds also for an ideal fluid. Eq. (5.2.2a) is directly averaged to give:

$$\frac{\partial B}{\partial t} + \frac{\partial V}{\partial x} = 0. \tag{5.2.9}$$

This is the acoustic counterpart of the electromagnetic equation $\partial \boldsymbol{B}/\partial t + \boldsymbol{\nabla} \times \boldsymbol{E} = 0$. We refer to $\boldsymbol{V}$ and B as the "Lorentz" fields.

We rewrite the Navier-Stokes equation in Eq. (5.2.2b) as:

$$\rho_0 \frac{\partial \boldsymbol{v}}{\partial t} = -\chi_0^{-1} \boldsymbol{\nabla} b + \boldsymbol{j}, \tag{5.2.10}$$

where $\boldsymbol{j}$ is introduced as

$$\boldsymbol{j} = -\boldsymbol{\nabla} p + \chi_0^{-1} \boldsymbol{\nabla} b + \eta \boldsymbol{\nabla}^2 \boldsymbol{v} + \left(\zeta + \frac{1}{3}\eta\right) \boldsymbol{\nabla} (\boldsymbol{\nabla} \cdot \boldsymbol{v}). \tag{5.2.11}$$

By averaging, we get:

$$\rho_0 \frac{\partial \boldsymbol{V}}{\partial t} = -\chi_0^{-1} \boldsymbol{\nabla} B + \boldsymbol{J}, \tag{5.2.12}$$

where the expression

$$\boldsymbol{J} = \langle \boldsymbol{j} \rangle - \chi_0^{-1} \langle b \boldsymbol{\nabla} I \rangle \tag{5.2.13}$$

is obtained by using the commutation relation $\langle \nabla b \rangle - \nabla \langle b \rangle = - \langle b \nabla I \rangle$ (see Eqs. (51) and (53) in [51]). Eq. (5.2.12) is analogous to

$$\epsilon_0 \frac{\partial \boldsymbol{E}}{\partial t} = \mu_0^{-1} \nabla \times \boldsymbol{B} - \boldsymbol{J} \tag{5.2.14}$$

in the absence of external charges or electric currents, where ϵ_0 and μ_0 are the electric permittivity and magnetic permeability in vacuum. $\boldsymbol{J}$ is the electromagnetic current associated with the macroscopic motion of the particles, induced by the macroscopic electromagnetic field perturbation in the medium.

Following Lorentz [205], in macroscopic electromagnetic framework, this induced bulk current is formally decomposed into a temporal derivative and a spatial derivative term: $\boldsymbol{J} = \partial \boldsymbol{P}/\partial t + \nabla \times \boldsymbol{M}$, where $\boldsymbol{P}$ and $\boldsymbol{M}$ are electric and magnetic polarization, respectively. Substituting this into Eq. (5.2.14) yields $\partial \boldsymbol{D}/\partial t = \nabla \times \boldsymbol{H}$ with $\boldsymbol{D} = \epsilon_0 \boldsymbol{E} + \boldsymbol{P}$ and $\boldsymbol{H} = \chi_0^{-1} \boldsymbol{B} - \boldsymbol{M}$.

Similarly, in our acoustic context, we decompose the induced bulk force $\boldsymbol{J} = J \boldsymbol{e}_x$:

$$J = \frac{\partial P}{\partial t} + \frac{\partial M}{\partial x}. \tag{5.2.15}$$

We then substitute Eq. (5.2.15) into Eq. (5.2.12).

$$\frac{\partial D}{\partial t} = -\frac{\partial H}{\partial x} \tag{5.2.16}$$

$$\begin{aligned} D &= \rho_0 V - P \\ H &= \chi_0^{-1} B - M \end{aligned} \tag{5.2.17}$$

The fields D and H introduced here are the *effective acoustic momentum* and *effective acoustic pressure* on the macroscopic scale, respectively.

As in electromagnetism, we assume the existence of constitutive laws $P = \hat{\chi}_p V$ and $M = \hat{\chi}_m B$ that relate the polarizations P and M to the Lorentz fields V and B,

where $\hat{\chi}_p$ and $\hat{\chi}_m$ are convolution operators.

$$P(t,x) = \int_{-\infty}^{t} dt' \int dx' \chi_p(t-t', x-x') V(t', x')$$
$$M(t,x) = \int_{-\infty}^{t} dt' \int dx' \chi_m(t-t', x-x') B(t', x')$$

Then, we complete the field equations, Eqs. (5.2.9) and (5.2.16), by the following constitutive relations

$$D = \hat{\rho}\, V \tag{5.2.18}$$
$$H = \hat{\chi}^{-1}\, B$$

where $\hat{\rho} = \rho_0 \hat{I} - \hat{\chi}_p$ and $\hat{\chi}^{-1} = \chi_0^{-1} \hat{I} - \hat{\chi}_m$; and $\hat{I}$ is the identity operator. Explicitly, these are the *nonlocal constitutive equations*

$$D(t,x) = \int_{-\infty}^{t} dt' \int dx' \rho(t-t', x-x') V(t', x') \tag{5.2.19a}$$
$$H(t,x) = \int_{-\infty}^{t} dt' \int dx' \chi^{-1}(t-t', x-x') B(t', x') \tag{5.2.19b}$$

stating that the fields D and H at a given time t and position x depend on the fields V and B at all previous time and all points of the space.

Unlike the Lorentz fields, the electromagnetic fields $\boldsymbol{H}$, $\boldsymbol{D}$, $\boldsymbol{P}$ and $\boldsymbol{M}$, and acoustic fields H, D, P and M are *not* the direct average of corresponding microscale fields. In what follows these are called "Maxwell fields" to be distinguished with Lorentz fields.

The constitutive laws express the Maxwell fields in terms of the Lorentz fields. Eq. (5.2.19a) is written in the most general form. It is unnecessary to add an extra convolution term to the right hand side of Eq. (5.2.19a) to relate $D(t,x)$ to $B(t',x')$. Because the fields V and B are related by the field equation Eq. (5.2.9), the effect of such an additional term is already incorporated in Eq. (5.2.19a) that includes the temporal and spatial dispersion in a general manner. The second constitutive relation Eq. (5.2.19b) is also written in the most general form. Because of Eq. (5.2.9), there is no need to add an extra convolution term to the right hand side of Eq. (5.2.19b) to

relate $H(t, \boldsymbol{r})$ to $V(t', \boldsymbol{r}')$. Similar arguments can be found in [195], Sec. 103 in the context of electrodynamics.

We note that the additional terms, which are not required in our framework, are of the same nature as the Willis coupling terms [199], which relate acoustic mean momentum (here, D) to mean strain (here, B), and also relate acoustic mean stress (here, H) to mean velocity. That is, if we wanted to consider the Willis coupling terms in the structure of our equations, they would be set to zero.

The general equations Eqs. (5.2.19) in the Fourier space are written as

$$D(\omega, k) = \rho(\omega, k)\, V(\omega, k) \tag{5.2.20a}$$

$$H(\omega, k) = \chi^{-1}(\omega, k)\, B(\omega, k) \tag{5.2.20b}$$

provided that

$$\rho(t, x) = \int \frac{d\omega}{2\pi} \frac{dk}{2\pi}\, \rho(\omega, k)\, e^{-i\omega t + ikx},$$

$$\chi^{-1}(t, x) = \int \frac{d\omega}{2\pi} \frac{dk}{2\pi}\, \chi^{-1}(\omega, k)\, e^{-i\omega t + ikx}.$$

For homogeneous medium with respect to time and space, $D(\omega, k)$ is related to $V(\omega, k)$, and $H(\omega, k)$ is related to $B(\omega, k)$ for the same values of ω and k.

Now, while the Eqs. (5.2.11), (5.2.13), and (5.2.15) uniquely fix the induced density field J, they do not determine the related polarization fields P and M independently. The fields H and D are also still ambiguous. We need an additional condition to clarify the Maxwell fields. In reference [51], the field H is identified as the acoustic energy flux $\boldsymbol{S} = S\boldsymbol{e}_x = \langle p\boldsymbol{v} \rangle$ by the "Poynting-Schoch energetic relation:

$$\langle p\boldsymbol{v} \rangle = H \langle \boldsymbol{v} \rangle. \tag{5.2.22}$$

The vector $\boldsymbol{S} = H\boldsymbol{V}$ plays the role of an acoustic Poynting vector analogous to its counterpart in electromagnetism. Eq. (5.2.22) gives the relevant macroscopic part H in the microscale pressure field p. As p is the thermodynamic excess pressure, and

$p\boldsymbol{v}$ is interpreted as the acoustic energy flux, it may be viewed as a thermodynamic relation. Again, unlike the Lorentz fields, the Maxwell field H is generally not the direct average of the corresponding microscale field. In particular, H is not exactly the mean pressure in the fluid $\langle p \rangle / \phi$.

Indeed, M derives from H and B, using the second equation of Eq. (5.2.17); P derives from M and J, using Eq. (5.2.15); and finally, D derives from P and V, by the first equation of Eq. (5.2.17). The nonlocal relations Eq. (5.2.19) completed by Eq. (5.2.22) provide a coherent framework that fully accounts for both temporal and spatial dispersion.

As in electromagnetism, the spatial dispersion effects can be very small in the long-wavelength limit. In that case, the nonlocal constitutive relations can be practically indistinguishable from *local constitutive relations*, that are expressed as

$$D(t,x) = \int_{-\infty}^{t} dt' \rho(t-t')\, V(t',x), \tag{5.2.23a}$$

$$H(t,x) = \int_{-\infty}^{t} dt' \chi^{-1}(t-t')\, B(t',x). \tag{5.2.23b}$$

Temporal dispersion effects are taken into account, in the sense that D and H at a given (t,x) depend on the history of the fields V and B at the same position. The time invariance of the system results in the dependence of the density and bulk modulus kernels on the time-difference $t-t'$. Therefore, we can write Eqs. (5.2.23) in Fourier space

$$D(\omega,x) = \rho(\omega)\, V(\omega,x) \tag{5.2.24a}$$

$$H(\omega,x) = \chi^{-1}(\omega)\, B(\omega,x) \tag{5.2.24b}$$

provided that

$$\begin{aligned} \rho(t) &= \int \frac{d\omega}{2\pi}\, \rho(\omega)\, e^{-i\omega t}, \\ \chi^{-1}(t) &= \int \frac{d\omega}{2\pi}\, \chi^{-1}(\omega)\, e^{-i\omega t}. \end{aligned}$$

The above relations correspond to an approximate modeling in long-wavelength regime, which is meaningful to consider when the geometries are sufficiently simple, without the involvement of very different pore sizes. The local formalism assumes that divergence is zero in the limit $\lambda \gg L$.

$$\boldsymbol{\nabla}.\boldsymbol{v} = \mathbf{0} \tag{5.2.26}$$

Thus it cannot describe local resonance behaviors in the medium. If we remove the viscothermal losses and assume local behavior so that the fluid is incompressible on the pore scale in Eq. (5.2.26), then the response of the fluid to an excitation should be instantaneous. Thus, the density and compressibility kernels become proportional to the Dirac delta: $\rho(t-t') = \rho_0\alpha_\infty\delta(t-t')$ and $\chi^{-1}(t-t') = \chi_0^{-1}\delta(t-t')$, where the geometric constant $\alpha_\infty \geq 1$ is known as tortuosity [206], which describes an apparent increase in the inertia of the incompressible ideal fluid that is forced into the tortuous pore network. Therefore, in this case, no temporal dispersion manifests. This demonstrates that the dispersion within the limit of Eqs. (5.2.23) is wholly linked to the losses.

In presence of the losses, the simplifying assumption – that in the long-wavelength limit the fluid appears as incompressible on the microscale – enables the separation of viscous/inertial and thermal/elastic effects. Hence, according to local theory, the viscous and inertial effects are encoded in the frequency-dependent effective density $\rho(\omega)$ [206] and the thermal and elastic effects are described by the effective bulk modulus $\chi^{-1}(\omega)$ [194]. When the frequency is considered as a complex quantity because of fluid incompressibility, the poles and zeros of these functions are on the negative imaginary axis of the frequency [206, 207, 194]. On the real frequency axis this leads to monotonic variations of these functions, excluding in particular resonant

behaviors [208], and expressed by simple and robust models of $\rho(\omega)$ and $\chi^{-1}(\omega)$, in terms of certain geometrical parameters.

To elucidate further why the fluid incompressibility on the pore scale requires a simple material geometry, suppose that we want to estimate the order of magnitude of the fluid divergence $\boldsymbol{\nabla} \cdot \boldsymbol{v}$ on the microscopic level. Let v be a characteristic amplitude of the velocity. Since the geometry is assumed to be simple, the period L is also a valid estimate of the characteristic pore length. While, for a general compressible fluid motion, the magnitude of the micro-level divergence can be estimated as v/L, we know that in our system the correct order of the magnitude of this quantity should be v/λ. As the order of magnitude of v/λ relative to v/L is $\varepsilon(= L/\lambda)$, and the local asymptotic approach is in the limit $\varepsilon \to 0$, it is clear that the fluid moves in an incompressible manner on the pore scale in Eq. (5.2.26). Likewise, to estimate the order of magnitude of the fluid pressure gradient $\boldsymbol{\nabla} p$ on the microscopic level, let p be a characteristic amplitude of the pressure represented in the form of $p = P + \delta p$, where $P \equiv \langle p \rangle / \phi$ (not to be confused with polarization field with the same notation P) is the mean fluid pressure that varies on the macroscopic scale, and δp is a pressure deviation with zero mean value. Therefore, we have $\boldsymbol{\nabla} p \sim P/\lambda + \delta p/L$. If the fluid is compressible, $\delta p \sim P$, and $\boldsymbol{\nabla} p \sim P/L$, while in our system $\boldsymbol{\nabla} p \sim P/\lambda$. This means that $\delta p/L \sim P/\lambda$, i.e. the deviation amplitude δp compared to the mean value P is very small, of the order ε. Consequently, in the long-wavelength limit $\varepsilon \to 0$, there is no gradient for the pressure (and its time derivative); the pressure profile can be regarded as uniform on the pore scale:

$$\boldsymbol{\nabla} \left(\frac{\partial p}{\partial t} \right) = 0. \tag{5.2.27}$$

The above equation is used to obtain $\chi^{-1}(\omega)$ in local theory.

Finally we note that in local theory, p in Eq. (5.2.22) can be replaced by its mean value in the fluid $P = \langle p \rangle / \phi$ and extracted from the average operator because the pressure deviation is negligibly small ($\delta p \sim \varepsilon P \ll P$). This immediately leads, in this special case, to the identification $H = \langle p \rangle / \phi = P$.

We have interpreted the local constitutive relations as if there is not any difference between the cell period L and the characteristic pore lengths. Only with this feature, the application of the two-scale asymptotic homogenization method is justified. In general, when widely different characteristic pore lengths are present, the scale separation parameter ε becomes ill-defined owing to the arbitrariness in the choice of micro level characteristic length. In that case, Helmholtz structures exhibiting local resonances may appear in the medium, and the nonlocal description is required in general. Another case requiring the nonlocal description is when the long-wavelength condition $\lambda \gg L$ is no longer satisfied, meaning that the fluid motion is no longer divergence-free on the pore scale, and in particular, Bragg scattering may appear.

Contrary to the approximate local framework, the general relations allowing for spatial dispersion, provide at the same time, the correct and untruncated description of temporal dispersion. Particularly, in a lossless medium, the temporal dispersion effects do not completely disappear, that is, the fluid does not respond instantly to an excitation, due to its compressible motion on the pore scale.

In summary, we establish a closed form, uniquely defined system within both the local approach and the nonlocal approach, by formulating the definitions of the macroscopic Lorentz fields based on microscopic fields; the Lorentz and Maxwell fields Eqs. (5.2.9) and (5.2.16); the constitutive local relations Eq. (5.2.23) and nonlocal relations Eq. (5.2.19); and the Poynting thermodynamic relation of acoustic energy flux (5.2.22). Only the nonlocal system takes the full account of the microscopic equations, and therefore, applies without restrictions on geometries and frequencies. In the following, we present the recipes to obtain the local effective functions $\rho(\omega)$ and $\chi^{-1}(\omega)$ involved in Eqs. (5.2.24), and the nonlocal effective functions $\rho(\omega, k)$ and $\chi^{-1}(\omega, k)$ introduced in Eqs. (5.2.20), based on the knowledge of microscale properties.

5.2.4 Local Effective Medium Parameters

The procedure to obtain effective properties of the medium in local theory is based on two assumptions. The first is the long-wavelength limit $\lambda \gg L$. The second is that fluid motion is divergence-free on the microscopic level. We can directly write

the two independent action-response problems, the solution of which determines the frequency-dependent density and bulk modulus. Hereafter, we systematically omit Re() for convenience; fields expressed as $\mathrm{Re}(Ue^{-i\omega t})$ are simply written as $Ue^{-i\omega t}$.

To compute the local effective density $\rho(\omega)$ for a given real-value frequency, we consider the following action-response problem. A harmonic bulk force $\boldsymbol{F}(t) = \boldsymbol{F}_0 e^{-i\omega t}$ with constant unidirectional amplitude $\boldsymbol{F}_0 = F_0 \boldsymbol{e}_x$ is applied to the flui. This is equivalent to applying a uniform harmonic macroscopic pressure drop $-\boldsymbol{\nabla} P(t) = \boldsymbol{F}_0 e^{-i\omega t}$ to the fluid. Coherent with the assumption of the fluid incompressibility on the microscale, we need to solve the following system in each realization $\boldsymbol{\omega}$ (*i.e.*, each random positioning in space without rotation of the phononic crystal sketched in Figure 5.1.1) in $\mathcal{V}^f(\boldsymbol{\omega})$.

$$\boldsymbol{\nabla}.\boldsymbol{v} = 0 \tag{5.2.28a}$$

$$-i\omega\rho_0 \boldsymbol{v} = -\boldsymbol{\nabla} p + \eta \boldsymbol{\nabla}^2 \boldsymbol{v} + \boldsymbol{F}_0 \tag{5.2.28b}$$

On the boundary $\partial\mathcal{V}(\boldsymbol{\omega})$, we set

$$\boldsymbol{v} = 0 \tag{5.2.29}$$

where the $\boldsymbol{v}(t, \boldsymbol{r}; \boldsymbol{\omega}) = \boldsymbol{v}(\omega, \boldsymbol{r}; \boldsymbol{\omega}) e^{-i\omega t}$ and $p(t, \boldsymbol{r}; \boldsymbol{\omega}) = p(\omega, \boldsymbol{r}; \boldsymbol{\omega}) e^{-i\omega t}$. The local theory's characteristic assumption in Eq. (5.2.28a) leads to the Laplacian form of the viscous terms in Eq. (5.2.28b) and is consistent with $\boldsymbol{F}_0$ treated as a spatial constant. $\boldsymbol{F}_0$ and p correspond to $-\boldsymbol{\nabla} P$ and δp, respectively, in line with the discussion on the fluid incompressibility in local theory (Sec. 5.2.3). When we neglect spatial dispersion, we treat $\boldsymbol{F}_0$ as a spatial (pore) constant.

We can find unique amplitude fields $\boldsymbol{v}(\omega, \boldsymbol{r}; \boldsymbol{\omega})$ and $p(\omega, \boldsymbol{r}; \boldsymbol{\omega})$, that are solutions to Eqs. (5.2.28)-(5.2.29). These solutions are periodic with period L in x-direction. The equations Eqs. (5.2.28)-(5.2.29) in the reference configuration can be obtained by the aforementioned two-scale asymptotic homogenization method at the leading order of the asymptotic expansions [209, 210]. Averaging the response field $\boldsymbol{v}(\omega, \boldsymbol{r}; \boldsymbol{\omega})$ over

the realizations $\boldsymbol{\omega}$, the local density for the effective fluid is given by:

$$\rho(\omega) = -\frac{F_0}{i\omega\, V(\omega)}. \tag{5.2.30}$$

Owing to the construction of the ensemble, exactly the same mean value $V(\omega)$ is obtained by solving Eqs. (5.2.28)-(5.2.29) in one single realization, and then, volume averaging the response velocity in one unit cell. This is how all the numerical results are obtained.

To compute the local effective bulk modulus $\chi^{-1}(\omega)$ at a real ω, we apply an excitation in the form of a heating rate at constant pressure $\dot{Q}(t) = \dot{Q}_0 e^{-i\omega t}$, where $\dot{Q}_0$ is a constant, or equivalently the material is subject to a uniform time harmonic pressure, such that $\beta_0 T_0 \partial p/\partial t = \dot{Q}_0 e^{-i\omega t}$. This results in the following action-response problem for the amplitude of the excess temperature field $\tau(t, \boldsymbol{r}; \boldsymbol{\omega}) = \tau(\omega, \boldsymbol{r}; \boldsymbol{\omega}) e^{-i\omega t}$ in $\mathcal{V}^f(\boldsymbol{\omega})$.

$$-i\omega\rho_0 c_p \tau = \kappa \boldsymbol{\nabla}^2 \tau + \dot{Q}_0 \tag{5.2.31}$$

On the boundary $\partial\mathcal{V}(\boldsymbol{\omega})$, we set:

$$\tau = 0. \tag{5.2.32}$$

There is a unique amplitude field $\tau(\omega, \boldsymbol{r}; \boldsymbol{\omega})$ response solution to Eqs. (5.2.31)-(5.2.32), which is periodic in L. This action-response problem in the reference configuration can also be obtained at the leading order within the classical asymptotic homogenization [194]. It is based on the physical assumption that the pressure field is a slowly variable quantity that may be viewed in first approximation as equal to the mean pressure. This assumption is incorporated in Eq. (5.2.31) in the very fact that $\dot{Q}_0$ is taken as a spatial constant. In fact, $\dot{Q}_0$ embodies the term $\beta_0 T_0 \partial p/\partial t$ in the wave propagation problem, and it is consistent to treat $\dot{Q}_0$ as a spatial constant: as we saw earlier, the divergence-free nature of the motion leads to $\beta_0 T_0 \boldsymbol{\nabla}(\partial p/\partial t) = 0$ in Eq. (5.2.27). Once the solution field τ is found, the factor ρ' analogous to the previous ρ is given as $\rho'(\omega) = -\dot{Q}_0/i\omega T(\omega)$, where $T = \langle\tau\rangle$.

In local theory, ρ' and χ are related by $\chi(\omega) = \phi\chi_0 \left[\gamma - (\gamma - 1)\rho_0 c_p/\rho'(\omega)\right]$. Thus

the local bulk modulus for the effective-fluid medium is:

$$\chi^{-1}(\omega) = \phi^{-1}\chi_0^{-1}\left[\gamma + (\gamma - 1)\frac{i\omega\rho_0 c_p T(\omega)}{\dot{Q}_0}\right]^{-1}. \tag{5.2.33}$$

In the local effective fluid, for a given frequency ω, there is only one single normal mode that can propagate in the positive x direction. With this single mode is associated a local wavenumber $k_L(\omega)$ that verifies the following *local dispersion relation*

$$\omega^2 - \frac{1}{\rho(\omega)\chi(\omega)}k_L^2 = 0 \tag{5.2.34}$$

such that $\mathrm{Im}(k_l) > 0$. The frequency-dependent complex phase velocity $c(\omega)$ and the complex impedance $Z(\omega)$ are obtained as below.

$$\begin{aligned} c(\omega) &= \frac{\omega}{k_L(\omega)} \\ Z(\omega) &= \left[\rho(\omega)\ \chi^{-1}(\omega)\right]^{1/2} \end{aligned} \tag{5.2.35}$$

5.2.5 Nonlocal Effective Medium Parameters

The procedure to obtain effective properties of the medium in nonlocal computation can be viewed as a generalization of the preceding local action-response problems accounting for spatial dispersion. The Fourier coefficients $\rho(\omega, k)$ and $\chi^{-1}(\omega, k)$ in (5.2.21) are directly related to the macroscopic (averaged) response of the permeating fluid subjected to a single-component (ω, k) Fourier pressure term,

$$\mathcal{P}(t, x) = \mathcal{P}_0 e^{-i\omega t + ikx}, \tag{5.2.36}$$

added to the pressure either in the Navier-Stokes equation in Eq. (5.2.2b) to obtain the nonlocal effective density, or to the Fourier equation in Eq. (5.2.6), to obtain the nonlocal effective bulk modulus χ^{-1} [51].

If the perturbation term is added to Eq. (5.2.2b), the excitation performs inhomogeneous (variable in time and space) work per unit volume and time. The excitation

amplitude is written as: $\boldsymbol{F}_0 e^{-i\omega t+ikx} = -\nabla\mathcal{P}$. The governing equations in the fluid region $\mathcal{V}^f(\boldsymbol{\omega})$ can be written as below.

$$\frac{\partial b}{\partial t} + \nabla \cdot \boldsymbol{v} = 0 \tag{5.2.37a}$$

$$\rho_0 \frac{\partial \boldsymbol{v}}{\partial t} = -\nabla p + \eta \nabla^2 \boldsymbol{v} + \left(\zeta + \tfrac{1}{3}\eta\right) \nabla \left(\nabla \cdot \boldsymbol{v}\right) \quad \underbrace{+\boldsymbol{F}_0 e^{-i\omega t+ikx}}_{\text{to obtain effective } \rho(\omega,k)} \tag{5.2.37b}$$

$$\rho_0 c_p \frac{\partial \tau}{\partial t} = \beta_0 T_0 \frac{\partial p}{\partial t} + \kappa \nabla^2 \tau \tag{5.2.37c}$$

$$\gamma \chi_0 p = b + \beta_0 \tau \tag{5.2.37d}$$

On the fluid/solid interfaceIf the perterbation term is added to Eq. (5.2.6), the excitation pumps an inhomogeneous amount of heat per unit volume and time. The excitation amplitude is written as: $\dot{Q}_0 e^{-i\omega t+ikx} = \beta_0 T_0 (\partial\mathcal{P}/\partial t)$.

$$\frac{\partial b}{\partial t} + \nabla \cdot \boldsymbol{v} = 0 \tag{5.2.38a}$$

$$\rho_0 \frac{\partial \boldsymbol{v}}{\partial t} = -\nabla p + \eta \nabla^2 \boldsymbol{v} + \left(\zeta + \tfrac{1}{3}\eta\right) \nabla \left(\nabla \cdot \boldsymbol{v}\right) \tag{5.2.38b}$$

$$\rho_0 c_p \frac{\partial \tau}{\partial t} = \beta_0 T_0 \frac{\partial p}{\partial t} + \kappa \nabla^2 \tau \quad \underbrace{+\dot{Q}_0 e^{-i\omega t+ikx}}_{\text{to obtain effective } \chi^{-1}(\omega,k)} \tag{5.2.38c}$$

$$\gamma \chi_0 p = b + \beta_0 \tau \tag{5.2.38d}$$

On the fluid/solid interfaceThe boundary condition for both action-response problems are:

$$\boldsymbol{v} = 0, \tag{5.2.39}$$

$$\tau = 0. \tag{5.2.40}$$

It is important to emphasize that the excitation variables ω and k are set as independent variables here. The solutions to the above systems for the response fields p, b, τ, and $\boldsymbol{v}$ take the form $p(t, \boldsymbol{r}; \boldsymbol{\omega}) = p(\omega, k, \boldsymbol{r}; \boldsymbol{\omega}) e^{-i\omega t+ikx}$ and so on. The amplitudes are periodic functions of x and are proportional to the excitation amplitude

$\mathcal{P}_0$. However, these solutions are not unique in the sense that the period can be chosen as any integer multiple of the irreducible period L. In what follows we exclude this ambiguity by requiring the amplitudes of the solutions to be periodic with L.

Once the two sets of action-response systems are solved independently, we use the fundamental relation in Eq. (5.2.22) to write

$$\mathtt{P}\langle \boldsymbol{v} \rangle = \langle p\boldsymbol{v} \rangle,$$

where the macroscopic part of the pressure response $p(t, \boldsymbol{r}; \boldsymbol{\omega})$ is:

$$\mathtt{P}(t, x) = \mathtt{P}(\omega, k) e^{-i\omega t + ikx},$$

whose amplitude is determined by $\mathtt{P}(\omega, k) = \{\langle p(\omega, k, \boldsymbol{r}; \boldsymbol{\omega}) \boldsymbol{v}(\omega, k, \boldsymbol{r}; \boldsymbol{\omega}) \rangle . \boldsymbol{e}_x\} / V(\omega, k)$.

To compute the *nonlocal density of the phononic fluid* $\rho(\omega, k)$, we use the Fourier transform of Eq. (5.2.16). We apply Eq. (5.2.20a) and postulate that the addition of the two parts $\mathtt{P}$ and $\mathcal{P}_0$ establishes the field H.

$$\rho(\omega, k) = \frac{k}{\omega V(\omega, k)} \left[\mathtt{P}(\omega, k) + \mathcal{P}_0\right] \tag{5.2.41}$$

Owing to the construction of the ensemble, exactly the same mean values $V(\omega, k)$ and $\mathtt{P}(\omega, k)$ are obtained by solving Eqs. (5.2.37)-(5.2.39) in one single realization and then applying the averages $\langle\ \rangle$ by volume integration in the chosen periodic unit cell. In order to get the response fields $p(\omega, k, \boldsymbol{r})$ and $\boldsymbol{v}(\omega, k, \boldsymbol{r})$, we explicitly solve the PDEs relating the amplitude fields in the reference unit cell.

To compute the *nonlocal bulk modulus of the phononic fluid* $\chi^{-1}(\omega, k)$, we use the Fourier transform of Eq. (5.2.19b). As before, we express H as the sum of $\mathtt{P}$ and $\mathcal{P}_0$.

$$\mathtt{P}(\omega, k) + \mathcal{P}_0 = \chi^{-1}(\omega, k) B(\omega, k)$$

Here, the field B has yet to be identified based on microscale dynamics. We postulate that it is composed of two parts, $B = \mathtt{B} + \mathcal{B}_0$. $\mathtt{B}(\omega, k) \equiv \langle b(\omega, k, \boldsymbol{r}; \boldsymbol{\omega}) \rangle$ is the non-

isothermal response part that originates in the field $b(t, \boldsymbol{r}; \boldsymbol{\omega}) = b(\omega, k, \boldsymbol{r}; \boldsymbol{\omega}) e^{-i\omega t + ikx}$ of the action-response problem Eqs. (5.2.37)-(5.2.39). $\mathcal{B}_0$ is an isothermal constant contribution, that can be directly written by averaging the isothermal term $\gamma\chi_0\mathcal{P}_0$; $\mathcal{B}_0 \equiv \langle \gamma\chi_0\mathcal{P}_0 \rangle = \phi\gamma\chi_0\mathcal{P}_0$, where ϕ is the porosity. This formulation of B has been suggested in [51].

$$\chi^{-1}(\omega, k) = \frac{1}{\mathrm{B}(\omega, k) + \mathcal{B}_0} \left[\mathrm{P}(\omega, k) + \mathcal{P}_0\right] \tag{5.2.42}$$

As before, averaging the amplitudes $v(\omega, k, \boldsymbol{r}; \boldsymbol{\omega})$, $b(\omega, k, \boldsymbol{r}; \boldsymbol{\omega})$, or $pv(\omega, k, \boldsymbol{r}; \boldsymbol{\omega})$ can be performed equivalently over a single unit-cell.

Contrary to the case of local theory, several normal mode solutions might exist because we include spatial dispersion with fields varying as $e^{-i\omega t + ikx}$. We denote each normal mode wavefector as $k_n(\omega)$, for $n = 1, 2, \cdots$. The dispersion equation is also generalized to account for nonlocality:

$$\omega^2 - \frac{k_n^2}{\rho_n(\omega, k_n)\chi_n(\omega, k_n)} = 0. \tag{5.2.43}$$

Furthermore, each wavenumber k_n are associated with a frequency-dependent density and bulk-modulus, such that

$$\begin{aligned} \rho_n(\omega) &= \rho_n[\omega, k_n(\omega)], \\ \chi_n^{-1}(\omega) &= \chi_n^{-1}[\omega, k_n(\omega)]. \end{aligned}$$

Therefore, the phase velocity and impedance of the normal mode n are written as

$$\begin{aligned} c_n(\omega) &= \frac{\omega}{k_n(\omega)}, \\ Z(\omega) &= \left[\rho_n(\omega)\, \chi_n^{-1}(\omega)\right]^{1/2}. \end{aligned} \tag{5.2.44}$$

Here we focus solely on the least attenuated mode $n = 1$ and its associated effective parameters. The results produced by the local and nonlocal theories and respective upscaling procedures are illustrated in Sec. 5.4. They are evaluated by performing an independent direct computation of the complex wavenumber or the phase velocity of

the least attenuated Bloch wave propagating in the reference phononic crystal.

5.3 Numerical Method

5.3.1 2D Finite Element Method for Microscopic Action-Response Problems

To obtain the effective medium parameters according to local and nonlocal theory, we use the finite element method (FEM) [34] to discretize the given unit cell geometry and solve the governing action-response equations for a given ω and k. For the local theory, we solve Eqs. (5.2.28)-(5.2.29) and Eqs. (5.2.31)-(5.2.32) using FEM. For the nonlocal theory, we solve Eqs. (5.2.37) and Eqs. (5.2.38) using FEM. These nonlocal equations in their explicit forms are available in Appendix C. We perform FEM computations using FreeFem++ [26], an open-source PDE solver. The weak form of the equations to be solved is firstly needed in order to implement the FEM simulations through this solver. Adaptive meshing was employed to deal with strong field variations in the medium. This way, we numerically compute $\rho(\omega, k)$ and $\chi^{-1}(\omega, k)$ at each ω and k.

5.3.2 Relationship to Nonlinear Eigenvalue Problems

Below, we show that solving this effective-medium model closely reproduces the dispersion relation. In fact, this method appears to be closely related to the techniques used for solving general eigenvalue problems, and appears to have a similar computational cost.

Eqs. (5.2.37)-(5.2.38) can be abstractly written in the form

$$\frac{\partial \boldsymbol{\psi}}{\partial t} = \boldsymbol{M}\boldsymbol{\psi} - \mathbf{f},$$

where $\boldsymbol{\psi}$ is a vector including $(b, \boldsymbol{v}, \tau)$, where p is eliminated via Eq. (5.2.37d). $\boldsymbol{M}$ is a differential operator, including all of the spatial derivatives and coefficients, and $\mathbf{f}$ is the forcing term from Eq. (5.2.36). In the frequency domain, this becomes a

"Helmholtz-like" equation as below.

$$\boldsymbol{A}\boldsymbol{\psi} = (\boldsymbol{M} + i\omega)\boldsymbol{\psi} = \mathbf{f} \tag{5.3.1}$$

Our effective medium technique corresponds to solving $\boldsymbol{A}\boldsymbol{\psi} = \mathbf{f}$ for two different forcing terms $\boldsymbol{F_0}$ and $\dot{Q}_0$, performing some integrals to find the effective media ρ in Eq. (5.2.41) and χ^{-1} in Eq. (5.2.42), in order to solve our scalar root-finding problem for the nonlocal dispersion equation in Eq. (5.2.43).

In contrast, a direct eigenvalue problem corresponds to solving $\det\boldsymbol{A}(\omega, k)$=0 for ω or k as described in Section 1.1.3. For frequency-independent materials, this is in fact a linear eigenvalue problem for ω or a quadratic eigenvalue problem for k, which can be converted into a linear eigenvalue problem of twice the size [41]. Nevertheless, it is still challenging because the problem is non-Hermitian, and many linear-eigenvalue solvers will involve repeatedly solving $\boldsymbol{A}\boldsymbol{\psi} = \mathbf{f}$ [40]. In fact, one popular type of method for both linear [211] and nonlinear [212, 213, 214] eigenvalue problems involves a very similar approach of integrating solutions to $\boldsymbol{A}\boldsymbol{\psi} = \mathbf{f}$ around a contour in the complex λ (ω or k) plane. This approach has been applied to eigenvalue problems in acoustics [215]. This is because the scalar quantity $g(\omega, k) =< \mathbf{f}, \boldsymbol{A}^{-1}\mathbf{f} >$ diverges (has a pole) whenever (ω, k) satisfy the exact dispersion relation, and therefore contour-integration methods can be applied to find these poles within a given contour. And once a solution $\omega(k)$ is found, it can be "tracked" as k varies via Newton's method and similar techniques.

5.3.3 Nonlinear Root-finding Methods: Newton-Raphson Method and Complex Contour Integration

We solve the nonlinear dispersion equations primarily using the Newton-Raphson method [216]. Implementation and usage of the Newton's method is straightforward, but the method requires a good initial guess to converge to a solution. A high-quality initial guess may be available from physical intuition for certain symple formalisms, but this is not always the case. When an appropriate initla guess for the Newton-Raphson

method is not available, we use the complex contour integration to provide the intial guess [217, 218]. This step is often crucial, especially to find multiple higher-order resonance modes.

For each mode $k_n(\omega)$ across a frequency range of interst, the dispersion equation is analytic as a function of ω. Once we obtain a good initial guess at the starting frqeuency ω_0 in the range of interest and find a converged solution at ω_0, we can update the initial guess of the subsequent frequency point to equal the converged solution from the preceding frequency point. This improves the quality of the initial guess compared to performing costly complex contour integration at every frequency point.

5.4 Results and Discussions

We present the results produced by local theory, nonlocal computation, and multiple scattering (direct Bloch-wave approach) – each describing the propagation of the least attenuated mode in 2D phononic crystals made of a square lattice of rigid cylinders embedded in air. We compute the effective macroscopic parameters for the least attenuated wave based on local and nonlocal theories, and compare the frequency-dependent phase velocity c, density ρ, bulk modulus $K = \chi^{-1}$, and impedance Z.

The geometry of the unit cell in Figure 5.1.1 is briefly summarized. The periodicity is $L = 10$ μm. The porosity is $\phi = 0.9$, and the radius of the cylinders $R = L[(1-\phi)/\pi]^{\frac{1}{2}}$ is 1.78 μm. These dimensions have been chosen for proof of concept, rather than for a particular experimental investigation. The present system is simple, highly symmetric, and does not exhibit any local resonance, in order to verify the multiscale model with readily available multiple scattering references. Therefore we expect the local theory to be valid for long-wavelength ($\lambda \gg L$) frequencies. The nonlocal approach is expected to be valid over the entire frequency band, without any constraint. The fluid properties for all computations are indicated in Table 5.4.1 [219].

The reference values to check our results are computed using the direct Bloch-wave approach as a reference as summarized in Appendix C. This direct approach provides,

Table 5.4.1: Fluid properties of air used in all computations

Parameter	Units	Value
adiabatic density ρ_0	kg/m^3	1.2
temperature T_0	K	293
sound velocity c_0	m/s	343
viscosity η	kg/ms	1.8×10^{-5}
sheer modulus ζ	kg/ms	0.6η (ignored in multiple scattering)
conductance κ	W/mK	2.6×10^{-2}
adiabatic compressibility χ_0	1/Pa	7.1×10^{-6}
specific heat capacity c_p	J/kgK	1005
ratio of specific heat $\gamma = c_p/c_v$	unitless	1.4

in principle, the dispersive Bloch wavenumber without defining effective constitutive parameters. One of the objectives of the present theoretical analysis is to describe both viscous and thermal losses precisely from the basic microscale equations, in effective-medium approaches, as well as in direct Bloch-wave approach. Air produces meaningful viscous, as well as thermal, losses. The general thermodynamic identity $\gamma - 1 = \beta_0^2 T_0/\rho_0 c_p$, shows that the deviation of γ from unity is a second order effect on the thermal expansion coefficient β_0. For a gas, like air, $\beta_0 \simeq 1/T_0$ is nonnegligible and γ is 1.4. Here, because $\gamma - 1$ is of order one, thermal losses can be comparable to viscous losses. Indeed, the thickness of the thermal boundary layer $\delta_t = (2\kappa/\rho_0 c_p \omega)^{\frac{1}{2}}$ is on the same order as the thickness of viscous boundary layer $\delta_v = (2\eta/\rho_0\omega)^{\frac{1}{2}}$. For a liquid, like water, β_0 is close to zero and γ is very close to 1. In this case, the values of the adiabatic bulk modulus $\chi^{-1}_{0(adiab)}$ and isothermal bulk modulus $\chi^{-1}_{0(isoth)}$ are very close to each other since $\chi^{-1}_{0(adiab)} = \gamma\chi^{-1}_{0(isoth)}$. Therefore, thermal exchanges have practically no effects.

The impact of the dissipation on the results can be shown in a more pronounced way, when the size of the cell is decreased, and thereby the viscous and thermal losses are enhanced in the medium. We note that for a given value of the normalized frequency $\Omega \equiv k_0 L/\pi = \omega L/c_0\pi$, where k_0 is the wavenumber in air, decreasing the size of the structure by a factor of a decreases the thickness of boundary layers by

only $\sqrt{a}$. Therefore, at a given normalized frequency Ω, a decrease in the size of the structural unit leads to the increase of the unit-cell space occupied by the boundary layers; $\delta_{v,t}/L$ follows $\sqrt{a}$. Consequently, decreasing the structural size increases the viscous and thermal effects at a given value of normalized frequency.

The local theory that does not allow for the spatial dispersion always predicts a single wave propagating in the medium. For the local theory, the frequency-dependent local density $\rho(\omega)$ and local bulk modulus $\chi^{-1}(\omega)$ are given by Eqs. (5.2.30) and (5.2.33). The effective local phase velocity, that is calculated via local dispersion equation in Eq. (5.2.34), is given by the left equation in Eq. (5.2.35), and the effective local impedance is achieved by the right equation in Eq. (5.2.35).

Figure 5.4.1 shows the real and imaginary parts of the phase velocity plotted against the normalized frequency k_0L/π. Figure 5.4.2 shows the real and imaginary parts of the wavenumber plotted against k_0L/π. The real and imaginary parts of the phase velocity computed bytr nonlocal computation in Eq. (5.2.44) via Newton's method converge exactly to the real and imaginary parts of Bloch phase velocity, in Eq. (C.2.10). The frequency range starts at $k_0L/\pi = 0.05$ corresponding to $\lambda_0 = 40L$, and ends at $k_0L/\pi = 2$, where the wavelength in air is equal to the periodicity, *i.e.*, $\lambda_0 = L$. The effective wavelength, according to either nonlocal computation or direct Bloch-wave approach, is $\lambda \simeq 33L$ at the starting frequency, and is $\lambda \simeq L$ at the ending point of the frequency band. The frequency band covers short waves up to those with wavelengths as small as the periodicity $\lambda \simeq L$. This includes the region where band gaps would appear in absence of viscothermal losses. The local theory is valid up to the frequency $k_0L/\pi \simeq 0.3$, where the real part of the wavenumber is $\mathrm{Re}(k) \simeq 10^5[\mathrm{m}^{-1}]$ (see Figure 5.4.2).

As shown in Figures 5.4.1 and 5.4.2, nonlocal method accurately computes the dispersive phase velocity for the entire first and second Brillouin zones. The Brillouin zones are specified based on the values of the $\mathrm{Re}(k)$ obtained at a real frequency ω. The first Brillouin zone is defined as $0 < |\mathrm{Re}(k)| < \pi/L$, associated with normalized

frequency k_0L/π between $0 < k_0L/\pi < 1$. Regarding the second Brillouin zone $\pi/L < |\mathrm{Re}(k)| < 2\pi/L$, its corresponding frequency band lies between $1 < k_0L/\pi < 1.8$. The rapid variations around $k_0L/\pi = 1$ correspond to the location of the first band gap. This may be viewed as a Bragg cell resonance, which occurs when the length of the cell is around $\lambda/2$. Dissipative losses prevent perfect bandgaps from forming.

In contrast, phase velocities predicted by the local theory cease to be valid above a certain frequency. As it was mentioned in Sec. 5.2.2, this is because the validity of the effective-medium parameters generated by the local theory is bounded up to the frequencies satisfying the condition two conditions. First, the fluid motions remain incompressible on the microscale in Eq. (5.2.26) when determining the microscopic velocity pattern. Second, the pressure field remains uniform on the microscale in Eq. (5.2.27) when determining the excess temperature pattern. So the macroscopic pressure in the validity domain of the local theory can be simplified as the direct average of the microscopic pressure in the fluid $H = \langle p \rangle / \phi = P \approx p$.

These characteristics are illustrated in Figure 5.4.3. Figures 5.4.3(a) and 5.4.3(b) plot the microscopic pressure field normalized by its macroscopic part H, at two representative frequency points. Figures 5.4.3(c) and 5.4.3(d) plot the divergence of the microscopic velocity normalized by its macroscopic value at identical representative frequency points. Figures 5.4.3(a) and 5.4.3(c) are plotted at $k_0L/\pi = 0.1$, which is seated in the validity domain of local approach. Figures 5.4.3(b) and 5.4.3(d) are plotted at $k_0L/\pi = 1$, which belongs to a region of Bragg scattering and rapid variations of the microscopic field patterns – where the local description is in error. Here, the real parts of $(\boldsymbol{\nabla} \cdot \boldsymbol{v})/(\boldsymbol{\nabla} \cdot \boldsymbol{V})$ and p/H are plotted in order to depict non-complex values. Within the validity range of local theory, the microscopic velocity divergence and pressure are very close to their macroscopic values, as seen from the uniformity of Figures 5.4.3(a) and 5.4.3(c). On the contrary, when the frequency is in Bragg's regime, the microscopic velocity divergence and the pressure varies greatly. This invalidates the assumptions used in the local theory.

The frequency-dependent effective density $\rho[\omega, k_1(\omega)] = \rho_1(\omega)$, and effective bulk modulus $\chi^{-1}[\omega, k_1(\omega)] = \chi_1^{-1}(\omega)$, of the corresponding principal normal mode, are

then calculated by replacing $k = k_1(\omega)$ in the aforementioned excitation terms in Eqs. (5.2.37b) and (5.2.37c). Subsequently, the nonlocal impedance in (5.2.44) is computed. Figures 5.4.4(a)-5.4.4(c) show the nonlocal density, bulk modulus, and impedance, as well as those based on the local theory. The local theory describes correctly the effective parameters only in the frequency range up to $k_0 L/\pi \simeq 0.3$, where $\lambda_0 = 10L$, and $\lambda = 7L$, which covers only the lowest one third of the first Brillouin zone.

Figures 5.4.5 and 5.4.6 present the phase velocity for $\phi = 0.7$ and $\phi = 0.99$, respectively. We observe good agreement between the nonlocal computation and multiple scattering method. For the more concentrated medium ($\phi = 0.7$, $R = 3.1$ μm), the discrepancies between local theory and direct Bloch-wave approach predictions are larger and commence at lower frequency. The trend is the opposite for the less concentrated medium in Figure 5.4.6. It is well known that more concentrated phononic crystals exhibit wider band gaps [182]. The scattering phenomena also become more influential.

Although our analysis concerns a 2D phononic crystal, the present nonlocal approach and its equations presented therein permits to consider limited cases of three-dimensional medium, *e.g.*, with spherical inclusions, as long as the propagation is along an existing principal symmetry axis. We also restricted our study to the propagation along a principal symmetry axis. Here, Poynting-Schoch quantity $\langle \boldsymbol{pv} \rangle$ in Eq. (5.2.22) lies in the direction of $\langle \boldsymbol{v} \rangle$ and H becomes a scalar field. Generalization to arbitrary directions could be possible, but has not yet been explored. Such a generalization would extend the definition of the macroscopic fields, action-response problems, and constitutive operators. Contrary to local theory, where indeed this generalization can be easily performed by tensor analysis, nonlocal theory requires a more careful construction because the Fourier components of the constitutive kernels are $\boldsymbol{k}$-dependent.

5.5 Conclusion

We present a multiscale numerical model for dissipative phononic crystals with strong nonlocality, by combining a nonlocal multiscale homogenization theory [51], a general FEM-based PDE solver in 2D, and a numerical root-finding method to solve the nonlinear and nonlocal dispersion equation.

We describe the nonlocal effective medium properties of a two-dimensional dissipative phononic crystal made of periodic arrays of rigid and motionless cylinders embedded in a viscothermal fluid such as air. To investigate the macroscopic dissipative dynamics of the medium, the nonlocal and local approaches are presented in a unified formulation in analogy to electromagnetism. Both temporal and spatial dispersion effects are included in the constitutive relations. We solve the dispersion equation for the least-attenuated mode in the phononic crystal using the nonlocal theory and obtain the frequency-dependent effective wavenumbers as eigenvalues of the medium. We compare our nonlocal scheme with the local theory as well as an analytical reference method based on multiple scattering (direct Bloch-wave approach). The multiple scattering method is exact, but is limited to very simple geometries only.

Our nonlocal computation based on FEM accurately predicts the phase velocity in the entire first and second Brillouin zones, in good agreement with the reference multiple scattering approach. On the other hand, the local theory approxmimation is valid only for the lowest one third of the first Brillouin zone. We also discuss and illustrate the important role of the microscopic distribution of the velocity-divergence of the fluid as the micro-level origin of the macroscopic spatial dispersion, and present the resulting effective medium density and compressibility results.

We demonstrate numerically that solving these effective-medium equations closely reproduces the exact dispersion relations. However, there are several open questions. First, can one prove this analytically? Or, alternatively, given the exact dispersion relation $\omega(k)$ and eigenfunctions, which can be probably found with a similar computational cost as discussed in Section 1.1.3, is there a better effective-medium definition that exactly reproduces $\omega(k)$? Most importantly, are any of these nonlo-

cal homogenized approximations useful beyond reproducing the dispersion relation? Can they approximately reproduce *e.g.*, scattering coefficients from interfaces in the medium? This is true of the local homogenization at very long wavelengths, but it has been a persistent problem with attempts at short-wavelength homogenization [45, 192, 193, 201].

Looking forward, this work can be extended in several directions. First, it would be beneficial to test the nonlocal scheme on more generalized geometries and boundary conditions. Practical applications for acoustic metamaterials would benefit from the extension of the method to elastic media and 3D structures. It is also highly desirable to experimentally verify the effective medium parameters to see how useful the values can be when complicated boundary conditions are introduced.

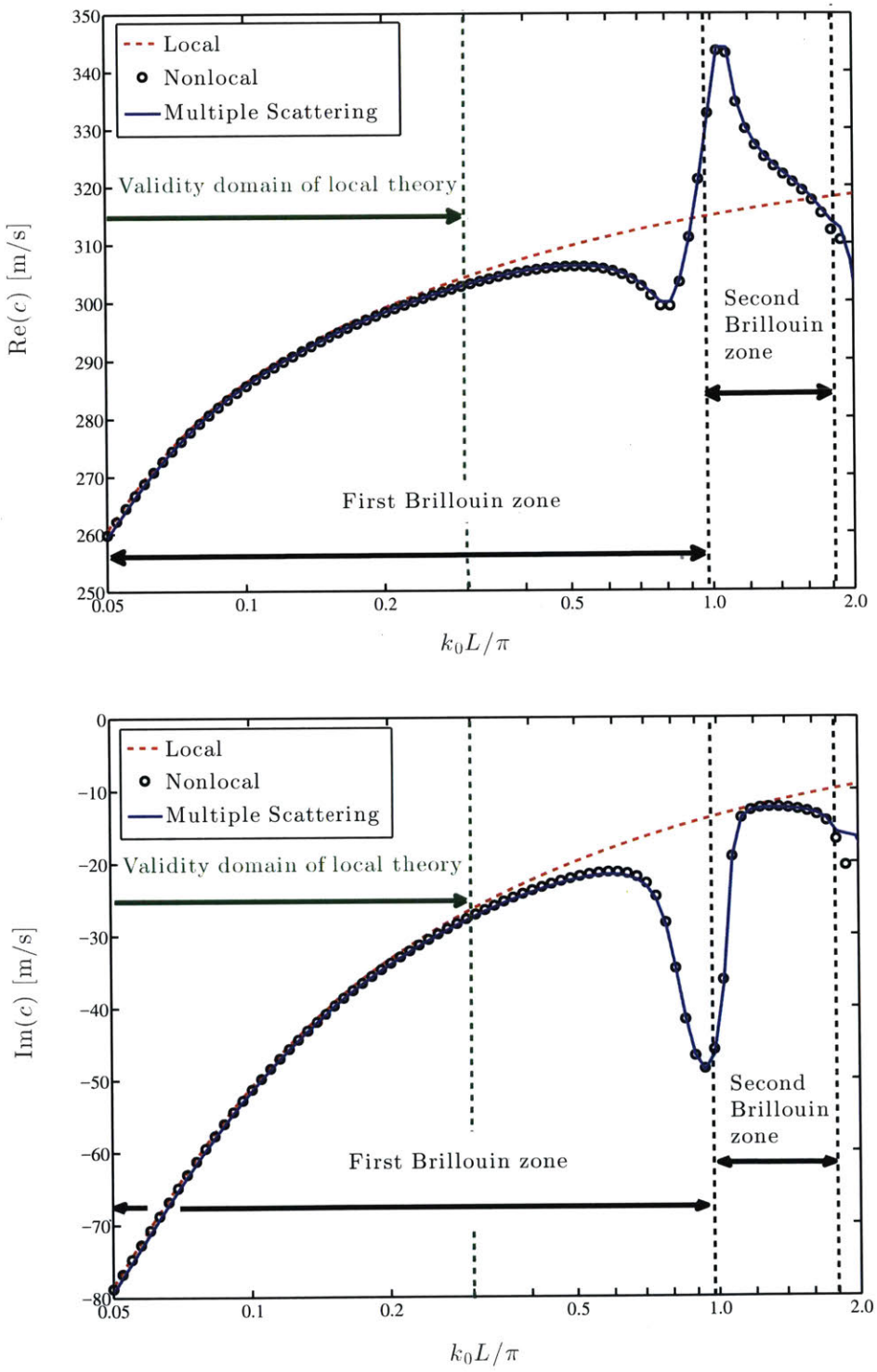

Figure 5.4.1: Real and imaginary parts of the phase velocities of the least attenuated mode for fluid filling fraction $\phi = 0.9$, computed using local theory approximation (red dashed), nonlocal FEM computation (black circles), and multiple scattering reference (blue). The frequency domain of the validity of the local theory is shown. The Brillouin zones are determined following the values of the real part of the wavenumber.

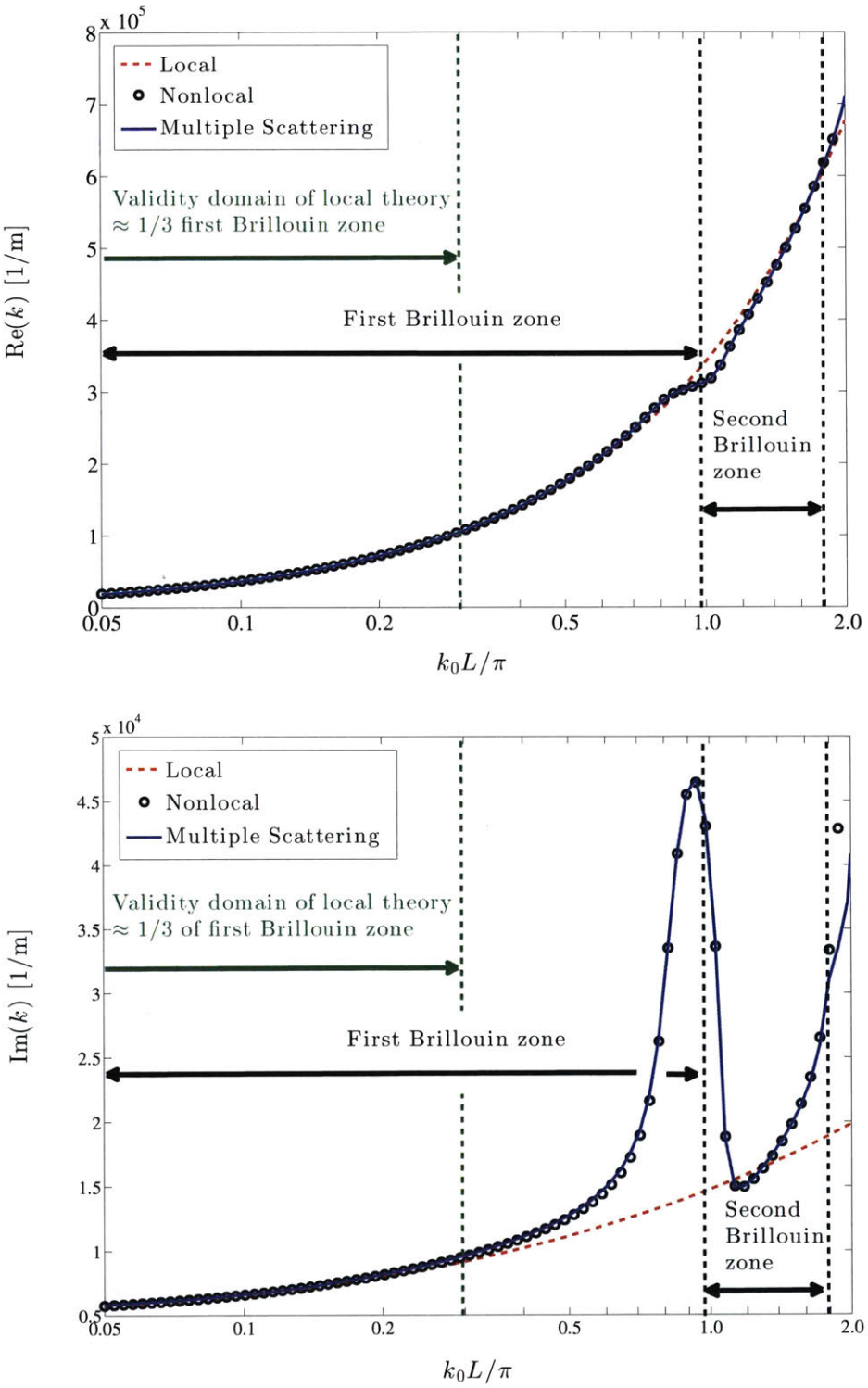

Figure 5.4.2: Real and imaginary parts of the wavevector of the least attenuated mode for fluid filling fraction $\phi = 0.9$, computed using local theory approximation (red dashed), nonlocal FEM computation (black circles), and multiple scattering reference (blue). The frequency domain of the validity of the local theory is shown. The Brillouin zones are determined following the values of the real part of the wavenumber.

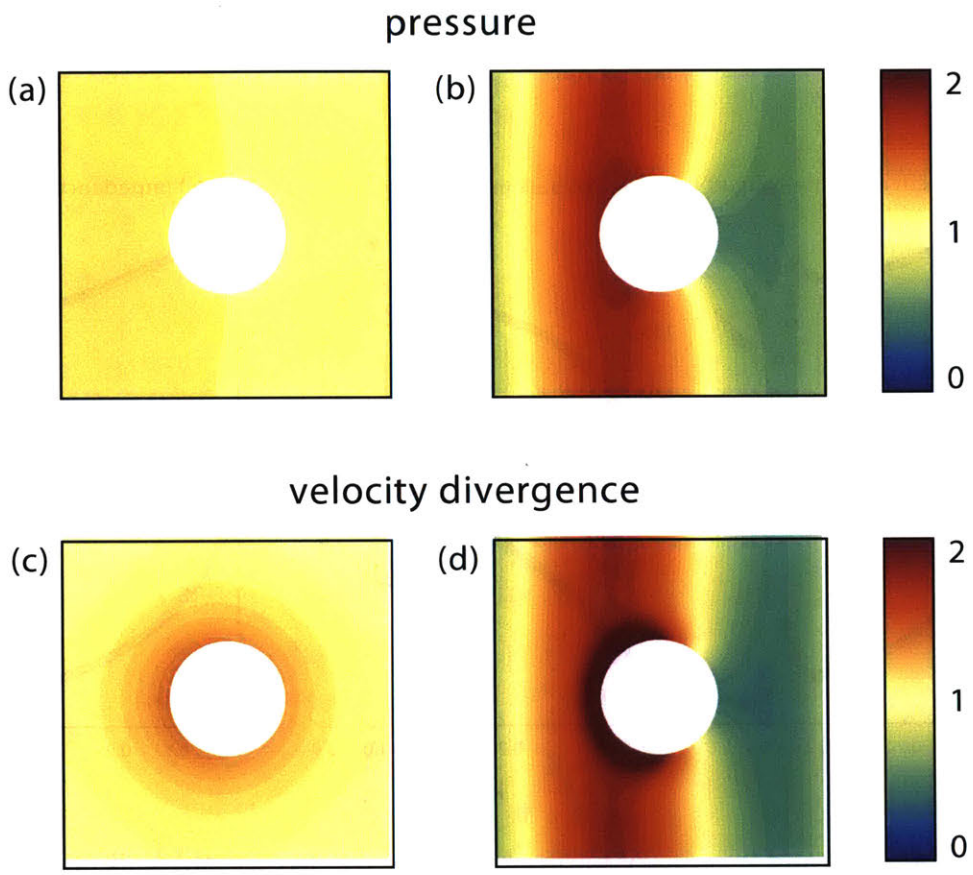

Figure 5.4.3: Pressure distribution inside the unit cell at (a) long-λ ($k_0 L/\pi = 0.1$) and short-λ ($k_0 L/\pi = 1.0$) excitation. Top: normalized velocity divergence at normalized frequency $k_0 L/\pi$ (a) $= 0.1$, and (b) short-wavelength, $k_0 L/\pi = 1.0$. Bottom: Normalized pressure at (a) long-wavelength, $k_0 L/\pi = 0.1$ and (b) short-wavelength, $k_0 L/\pi = 1.0$.

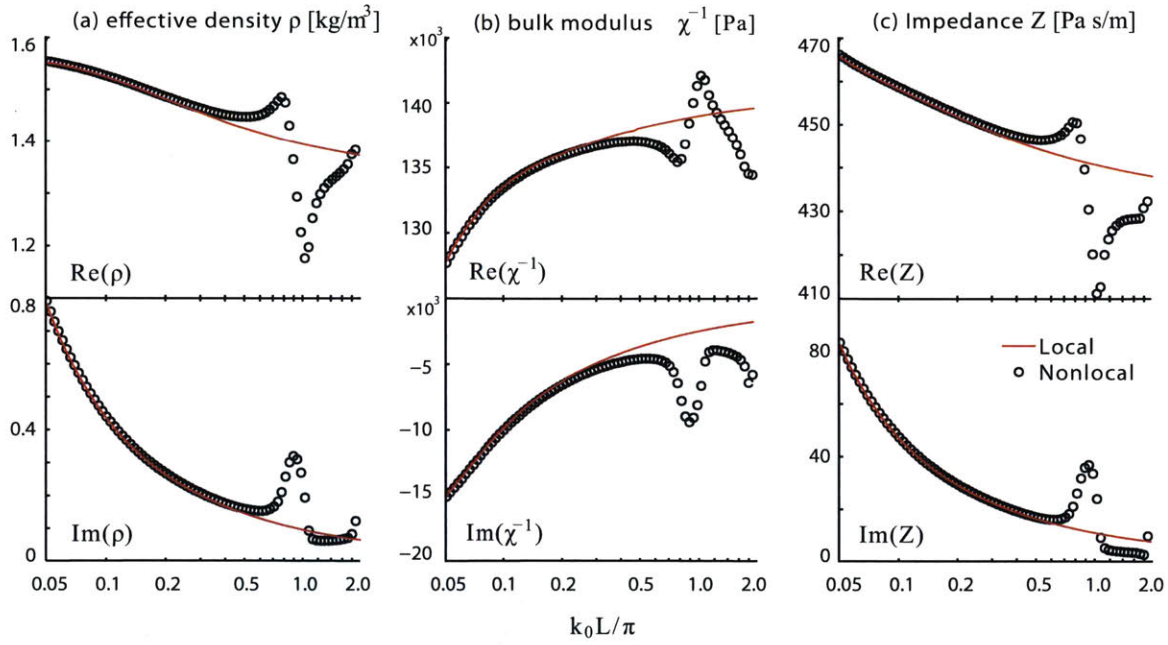

Figure 5.4.4: Real and imaginary parts of effective (a) density, (b) bulk modulus, and (c) wave impedance of the least attenuated wave according to local approximation, and exact nonlocal computation, for porosity $\phi = 0.9$.

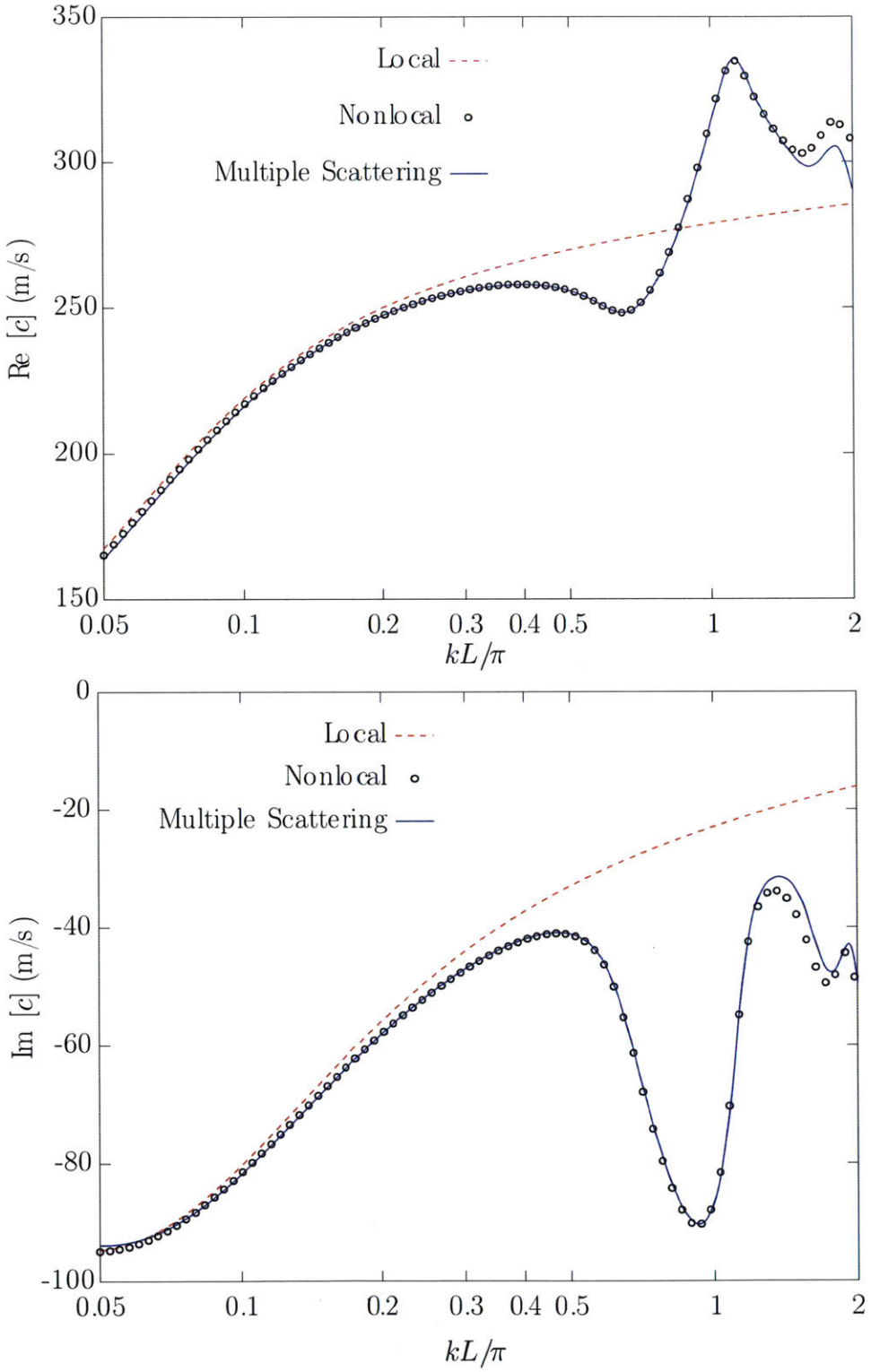

Figure 5.4.5: Real and imaginary parts of the phase velocities of the least attenuated mode for fluid filling fraction $\phi = 0.7$, computed using local theory approximation (red dashed), nonlocal FEM computation (black circles), and multiple scattering reference (blue).

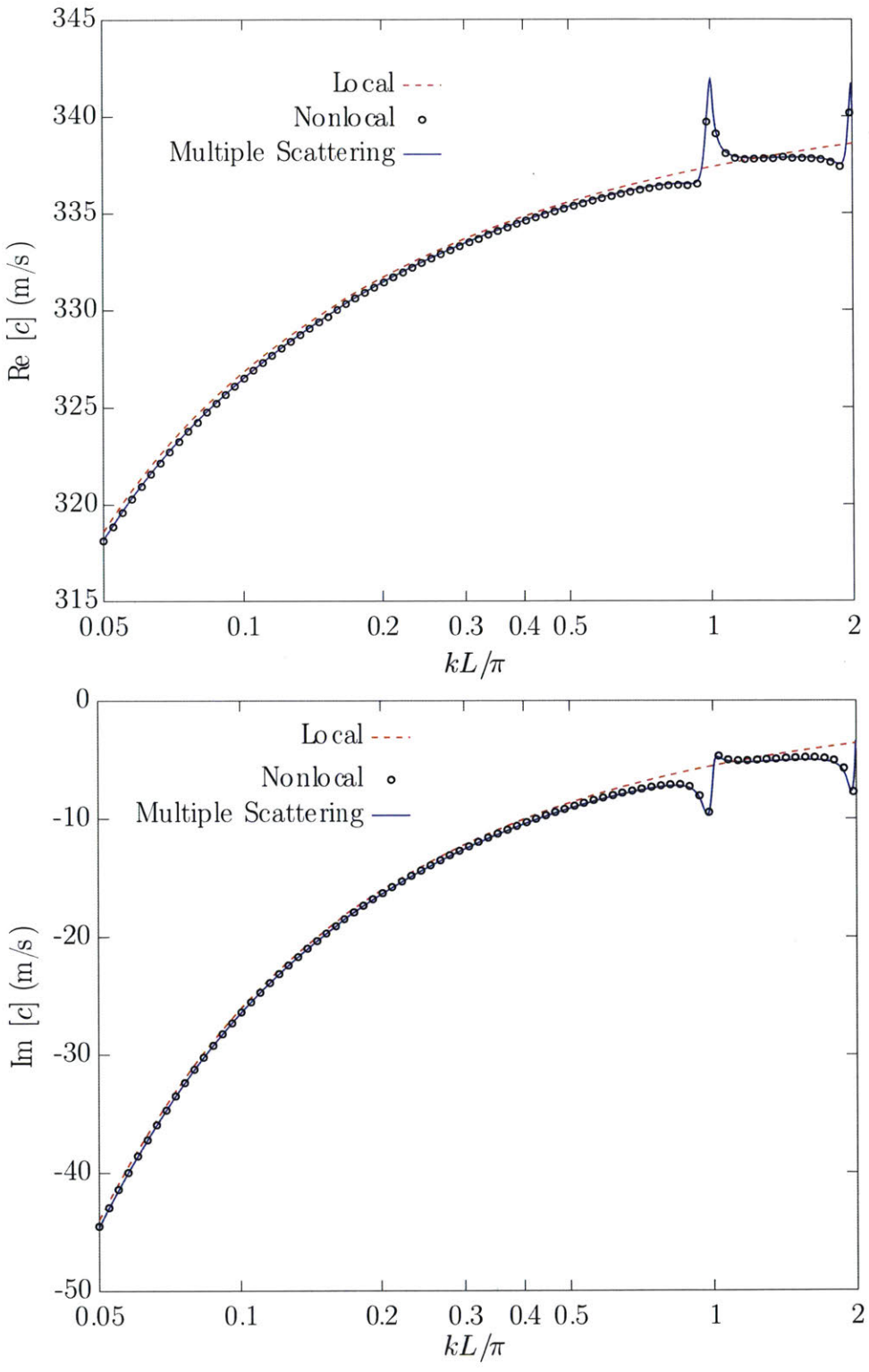

Figure 5.4.6: Real and imaginary parts of the phase velocities of the least attenuated mode for fluid filling fraction $\phi = 0.99$, computed using local theory approximation (red dashed), nonlocal FEM computation (black circles), and multiple scattering reference (blue).

Chapter 6

Summary

This thesis presents hybrid numerical methods for the design and analysis of optimal wavefronts and subwavelength structures in optics and acoustics. We focus on wave-matter interaction systems that enhance mechanical effects on the nanoscale, including: holographic optical tweezers in Chapter 3, broadband photonic crystal solar absorbers in Chapter 4, and nonlocal phononic crystal composite materials in Chapter 5. We tackle the practical challenges of exploring large numbers of design parameters for complex wave-engineering systems by offering computer-automated design frameworks that effectively combine the best computational software developed in physics, numerical analysis, and inverse design.

In Part I, we present computational inverse design methods for holographic optical tweezers. Chapter 2 analyzes the interesting physical phenomena of optical torque enhancement through multipolar plasmonic resonance. We model representative nanoparticles that scatter, absorb, and radiate light in various directions in space and analyze how radiation force or torque relates to multipolar plasmon resonance. Our FDTD numerical simulations suggest that the surface plasmon polariton-enhanced scattering can lead to a negative angular momentum conversion ratio, and hence produce an extraordinarily large torque. We show that torque induced by resonant scattering can contribute to 80% of the total optical torque in gold particles at multipolar resonance frequencies.

Next, Chapter 3 builds on the observations of Chapter 2 and investigates how

to maximize such unconventional optical forces or torques by varying the incident fields, from simple circular polarized plane waves to spatially modulated holographic illuminations. By combining a compact Bessel basis and a fast boundary element method, we achieve a 20-fold enhancement in torque per intensity, over a standard circular-polarized illumination, on a model plasmonic nanoparticle. We numerically demonstrate a 20-fold enhancement in optical torque per intensity on an example plasmonic nanoparticle, compared to a circularly polarized planewave. We analyze the optimization results for 2000 random initial configurations, discuss the tradeoff between robustness and enhancement, and compare the different effects of multipolar plasmon resonances on enhancing force or torque.

Previously, the major bottleneck for efficient wavefront design has been the cumbersome computation. We overcome this bottleneck with a compact cylindrical Bessel basis and a fast boundary element method. We are optimistic that such computational framework for 3D vector fields can be generalized and applied to other interesting design problems that involve three-dimensional wavefronts or vector fields. Looking forward, it would be very exciting to develop real-time numerical methods for wavefront modulation and combine them with experimental setups for holographic imaging and particle manipulation. Another important future direction is to derive fundamental upper bounds to wave-induced mechanical effects, such as radiation pressure, radiative heating, as well as induced thermophoretic and electrophoretic actuation effects.

In Part II, we present mode analysis and numerical parameter-testing strategies for periodic subwavelength structures in optics and acoustics. Chapter 4 presents the FDTD numerical analysis for a broadband metallic-dielectric photonic crystal (MDPhC) solar absorber developed and fabricated in Prof. Sang-Gook Kim's group at MIT [168]. Through numerical parameter-studies, we discuss the tunability and spectrum-selectivity of the MDPhC optical response. We analyze that the broadband absorption is due to a high density of optical cavity modes overlapped with surface plasmon polariton modes, and highlight the importance of the thin film coating layer in tuning the hybrid resonances. The MDPhC structure can be designed with various

alternative metals and dielectrics for various other applications that require a tunable electromagnetic dispersion. An interesting future direction for computation would be to combine full-wave optical simulations with deep-subwavelength modeling, such as density functional theory, for efficient multi-scale modeling of complex structures; *i.e.,* composite structures with multiple characteristic length scales due to atomically thin coatings or nanoparticle inclusions. Another meaningful direction forward would be to automate structural prototyping through topological shape optimization.

Chapter 5 develops a multiscale numerical model for dissipative phononic crystals with strong nonlocality, by combining (i) a nonlocal multiscale homogenization theory developed by Lafarge and Nemati [51], (ii) a general FEM-based PDE solver in 2D, and (iii) a numerical root-finding method for the nonlocal dispersion equation, based on Newton-Raphson method and complex contour integration method. We demonstrate numerically that solving our effective-medium equations closely reproduces the exact dispersion relations for the least-attenuated mode in the model phononic crystal. Our nonlocal computation accurately predicts the phase velocity in the entire first and second Brillouin zones, in good agreement with the reference multiple scattering approach, while the local theory approxmimation is valid only for the lowest one third of the first Brillouin zone. We also discuss and illustrate the important role of the microscopic distribution of the velocity-divergence of the fluid as the micro-level origin of the macroscopic spatial dispersion, and present the resulting effective medium density and compressibility results. Several open questions remain to be answered in the future. In particular, can nonlocal homogenization accurately reproduce not only the dispersion relation but also the reflection and transmission from the homogenized medium? It would be extremely useful to verify the nonlocal scheme using more generalized geometries and boundary conditions, and perform both numerical and experimental tests. Practical applications for acoustic metamaterials would also benefit from the extension of the method to elastic media and 3D geometries.

In summary, our work pushes to open the design space for optimal wavefronts and subwavelength structures by efficiently exploring high-dimensional parameter spaces via hybrid numerical techniques for PDEs and nonlinear systems. We hope

our numerical frameworks can be generalized and applied to useful design problems in wave engineering, to store *energy*, perform *work*, or transfer *heat* – in increasingly resourceful and sophisticated ways – above and beyond the nanometer scale.

Appendix

Appendix A

Material Property and Optical Extinction of Plasmonic Structures

This chapter is based on: Y. E. Lee, K. H. Fung, D. Jin, and N. X. Fang, "Optical torque from enhanced scattering by multipolar plasmonic resonance," Nanophotonics, Vol. 3(6): 343-440 (2014).

A.1 Material Property

The dielectric function of gold used in all our numerical simulations is plotted in Figure A.1.1. The experimental data from Palik [31] has been smoothly fitted. The imaginary part of the dielectric function is connected to the absorption of the material.

The optical response of a nanostructure is governed by both the material response and the geometrical structure. It is important to distinguish between the two, in order to clearly understand the mechanism behind the resonantly enhanced transfer of angular optical momentum. According to the results in Chapter 2, the enhanced optical torque from scattering is predominantly governed by the geometry of the nanoparticles, whereas that from absorption is nearly unaffected by the shape change. The absorptive behavior solely reflects the intrinsic response of the material. The same was found to be true for metallic particles made of other materials, such as silver and aluminum, for nanoparticles in the size range that supports multipolar plasmonic

resonance.

A.2 Extinction Spectra

The extinction, scattering, and absorption spectra of the gold nanoparticles are plotted in Figure A.2.1. This represents the strength of the combined response from the material, size, and shape of the nanoparticles. The cross sections are calculated using the total-field scattered-field (TFSF) source in the FDTD simulation, which is a standard treatment. [28] The polarization of the incident light does not change the optical response because of the simple particle geometry. Without loss of generality, a monochromatic, normally incident, linearly polarized plane wave is used as the source of excitation.

The optical response for the gold nanoparticles with the characteristic length of d=400nm is dominated by scattering, which means that the number of photons that are scattered is much greater than the number of photons absorbed. Nevertheless, the process of scattering has been longtime overlooked as a possible mechanism to create torque, since there are no means to significantly alter the angular momentum carried by the scattered field with conventional dielectrics and large particles.

The influence of the material response is prominent in the absorption cross section (red dotted curve), especially below the wavelength of 500nm. According to the three absorption cross sections, the amount of light absorbed is nearly the same for all three particles. While particles with the same material and size with varied shape show minimal difference in absorption, a variation in material or size creates large differences in absorption. [54] In other words, absorption is predominantly governed by the number of the charges on the metallic surface, rather than by a small change in their distribution.

It is worth highlighting the importance of the particle dimension by comparing the results from a 400nm particle and a 40nm particle. While both can exhibit plasmonic resonance, the nature of the localized surface plasmon resonance (LSPR) should be extremely different for the two cases. The optical response of the 40nm particle is

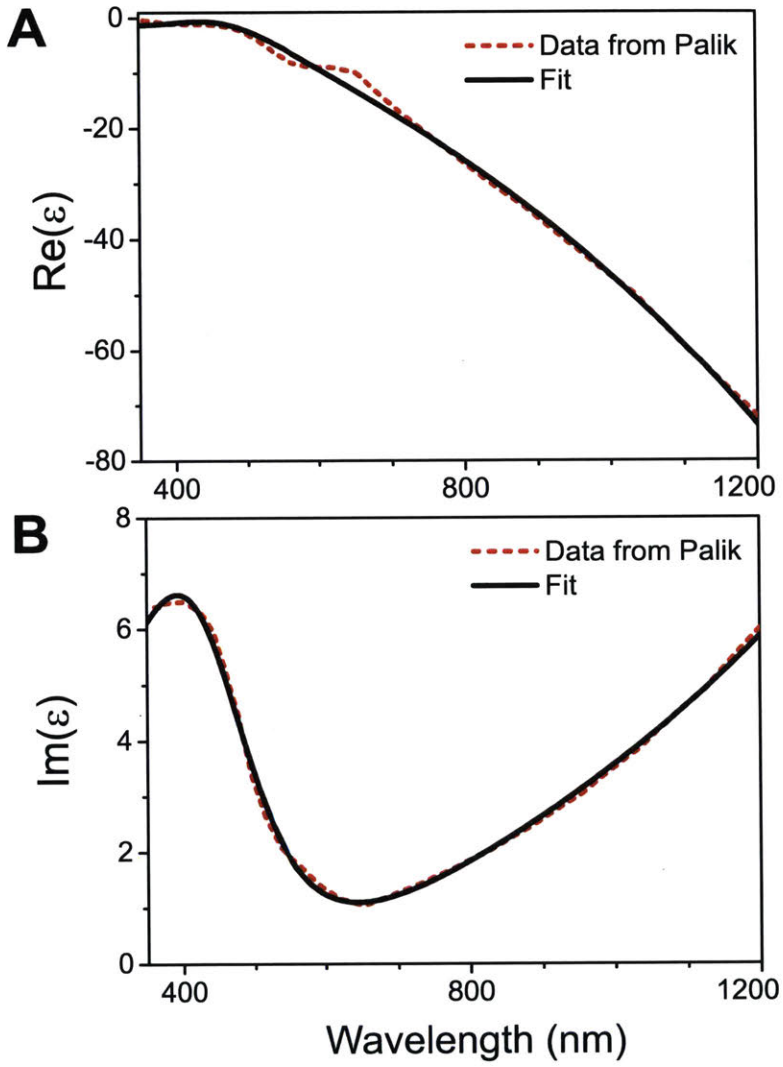

Figure A.1.1: The dielectric function of gold. Top: Real part of the dielectric function. Bottom: Imaginary part of the dielectric function. The dotted line is the smoothed experimental data from Palik, and the solid like is the fiting function used in FDTD.

almost entirely dominated by absorption, [99] unlike the 400nm particle in Figure A.2.1. While surface plasmon resonance can be excited when there is a surface between a metal and a dielectric, the characteristics of this can be extremely different depending on the size of the particles. [220]

In contrast, the scattering cross section (blue curve) shows a clear difference in each spectrum in Figure A.2.1, especially regarding the emergence of the small resonance peak near the wavelength of 500nm. The large peak above 900nm represents the dipole mode, and the small peak corresponds to the negative quadrupole mode for the triangle in Figure A.2.1(a), and to the negative hexapole mode for the square in Figure A.2.1(b). The circle in Figure A.2.1(c) does not support any higher-order multipolar resonance. The shape of the plasmonic particles determines the nature of scattering. [220] This is especially remarkable when the dimension of the particle is comparable to the wavelength of light, as the result of this letter indicates.

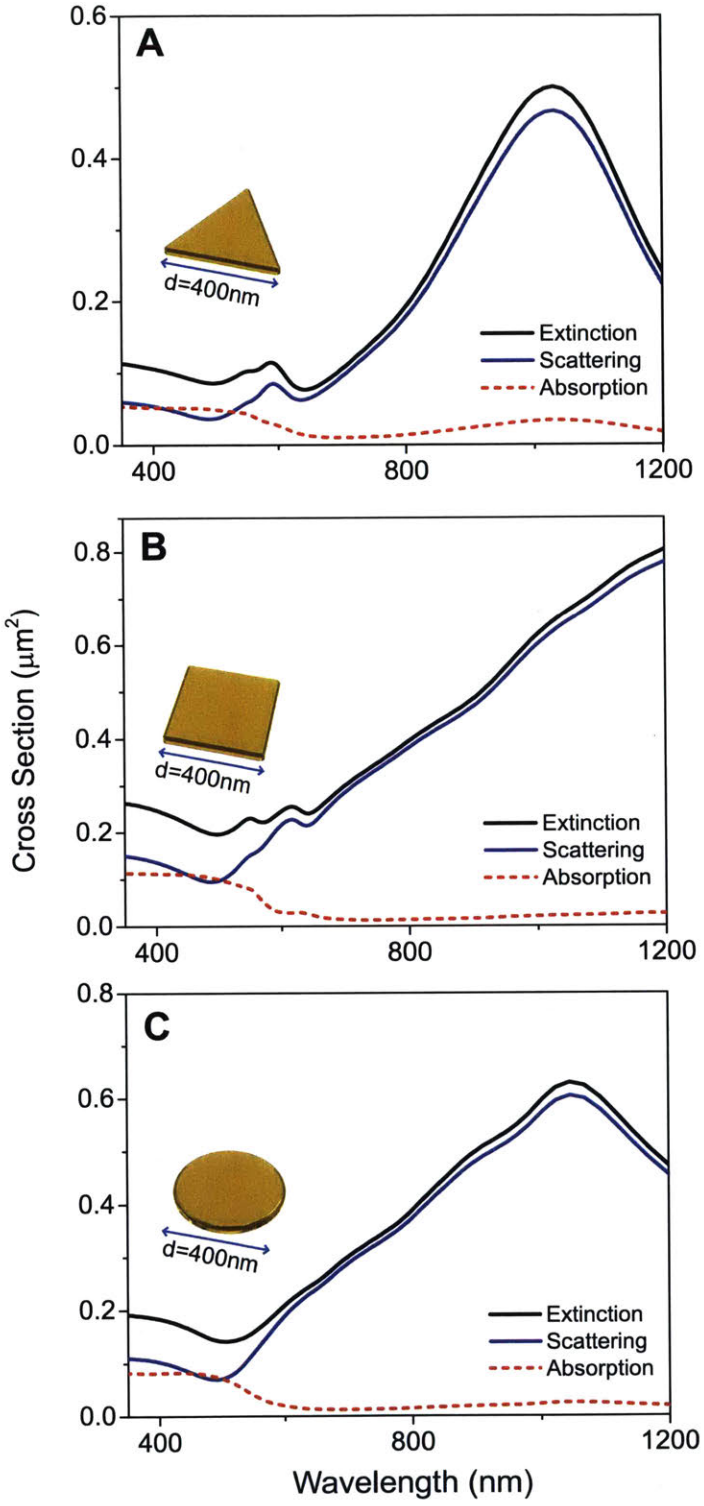

Figure A.2.1: The extinction (black), scattering (blue), and absorption (red dotted) spectra of the three characteristic geometries used in Chapter 2 are plotted as a function of wavelength. For all cases, the nanoparticle is made of gold; the characteristic lateral dimension is 400nm; and the thickness is 40nm. The dielectric environment is set as vacuum, with refractive index n=1.

Appendix B

Solutions of Vector Wave Equations in Cylindrical Coordinates

This chapter summarizes well-known equations for mathematically describing laser beams in cylindrical coordinates, based on [1, 18, 221, 109].

B.1 Curvilinear Coordinates

The orthonormal expansions of electromagnetic vector fields rely on the solutions of the vector wave equation in orthogonal curvilinear coordinates. A coordinate system composed of intersecting surfaces is defined as a curvilinear coordinate system. Further, a curvilinear coordinate system is orthogonal if the intersecting surfaces are all at right angles, and skew if not.

In any curvilinear coordinate system, we can define spatial elements as a function of (a) coordinate basis u_i (*e.g.*, ϕ); (b) orthonormal unit vector $\hat{\mathbf{u}}_i$ (*e.g.*, $\hat{\boldsymbol{\phi}}$); and (c) scale factor h_i ensuring that the quantity $h_i u_i$ have the unit of length (*e.g.*, $h_\phi = r$ for cylindrical coordinates), as summarized in Table B.1.1.

The differential vector is defined as $\mathrm{d}\mathbf{r} = h_i \mathrm{d}u_i \hat{\mathbf{u}}_i = h_1 \mathrm{d}u_1 \hat{\mathbf{u}}_1 + h_2 \mathrm{d}u_2 \hat{\mathbf{u}}_2 + h_3 \mathrm{d}u_3 \hat{\mathbf{u}}_3$ and the *scale factor* is defined as $h_i = \left| \frac{\partial \mathbf{r}}{\partial u_i} \right|$. The line element is defined as: $\mathrm{d}\mathbf{s}^2 =$

	Cartesian	Cylindrical	Spherical
$\hat{\mathbf{u}}_i$	$(\hat{\mathbf{x}}, \hat{\mathbf{y}}, \hat{\mathbf{z}})$	$\left(\hat{\mathbf{r}}, \hat{\boldsymbol{\phi}}, \hat{\mathbf{z}}\right)$	$\left(\hat{\mathbf{r}}, \hat{\boldsymbol{\theta}}, \hat{\boldsymbol{\phi}}\right)$
u_i	(x, y, z)	(r, ϕ, z)	(ρ, θ, ϕ)
h_i	$(1, 1, 1)$	$(1, r, 1)$	$(1, r, r\sin\theta)$

Table B.1.1: Spatial elements of orthogonal curvilinear coordinates.

$\mathrm{d}\mathbf{r} \cdot \mathrm{d}\mathbf{r} = h_i^2 \mathrm{d}u_i^2 = h_1^2 \mathrm{d}u_1^2 + h_2^2 \mathrm{d}u_2^2 + h_3^2 \mathrm{d}u_3^2$. The volume element is defined as:

$$\begin{aligned}
\mathrm{d}V =& \prod_i^n h_i \mathrm{d}u_i \\
=& h_1 h_2 h_3 \, \mathrm{d}u_1 \mathrm{d}u_2 \mathrm{d}u_3 \\
=& \begin{vmatrix} \partial_{u_1} x & \partial_{u_2} x & \partial_{u_3} x \\ \partial_{u_1} y & \partial_{u_2} y & \partial_{u_3} y \\ \partial_{u_1} z & \partial_{u_2} z & \partial_{u_3} z \end{vmatrix} \mathrm{d}u_1 \mathrm{d}u_2 \mathrm{d}u_3 \\
=& \left| \frac{\partial(x, y, z)}{(\partial u_1, \partial u_2, \partial u_3)} \right| \mathrm{d}u_1 \mathrm{d}u_2 \mathrm{d}u_3
\end{aligned}$$

where the determinant of the Jacobian matrix is used.

Spatial Derivatives in Orthogonal Curvilinear Coordinates

Gradient for a scalar field ψ in orthogonal curvilinear coordinates is expressed as:

$$\nabla\psi = \frac{1}{h_i} \frac{\partial \psi}{\partial u_i} \hat{\mathbf{u}}_i, \tag{B.1.1}$$

and the Laplacian is:

$$\nabla^2 \psi = \frac{1}{h_1 h_2 h_3} \left[\frac{\partial}{\partial u_1} \left(\frac{h_2 h_3}{h_1} \frac{\partial}{\partial u_1} \right) + \frac{\partial}{\partial u_2} \left(\frac{h_3 h_1}{h_2} \frac{\partial}{\partial u_2} \right) + \frac{\partial}{\partial u_3} \left(\frac{h_1 h_2}{h_3} \frac{\partial}{\partial u_3} \right) \right] \psi. \tag{B.1.2}$$

For a vector field $\mathbf{F} \equiv F_1 \hat{\mathbf{u}}_1 + F_2 \hat{\mathbf{u}}_2 + F_3 \hat{\mathbf{u}}_3$, divergence is defined and express as:

$$\boldsymbol{\nabla} \cdot \mathbf{F} = \lim_{V \to 0} \frac{\int_S \mathbf{F} \cdot \mathrm{d}A}{V} = \frac{1}{h_1 h_2 h_3} \left[\frac{\partial}{\partial u_1} (h_2 h_3 F_1) + \frac{\partial}{\partial u_2} (h_3 h_1 F_2) + \frac{\partial}{\partial u_3} (h_1 h_2 F_3) \right]. \tag{B.1.3}$$

The curl is defined as

$$(\boldsymbol{\nabla} \times \mathbf{F}) \cdot \hat{\mathbf{n}} \equiv \lim_{A \to 0} \frac{\oint_C \mathbf{F} \cdot \mathrm{ds}}{A} \tag{B.1.4}$$

and expressed as

$$\boldsymbol{\nabla} \times \mathbf{F} \equiv \frac{1}{h_1 h_2 h_3} \begin{vmatrix} h_1 \hat{\mathbf{u}}_1 & h_3 \hat{\mathbf{u}}_2 & h_3 \hat{\mathbf{u}}_3 \\ \frac{\partial}{\partial u_1} & \frac{\partial}{\partial u_2} & \frac{\partial}{\partial u_3} \\ h_1 F_1 & h_2 F_2 & h_3 F_3 \end{vmatrix}. \tag{B.1.5}$$

Lastly, the vector Laplacian can be expressed as:

$$\begin{aligned} \boldsymbol{\nabla}^2 \mathbf{F} &= \boldsymbol{\nabla} \cdot (\nabla \mathbf{F}) \\ &= \nabla(\boldsymbol{\nabla} \cdot \mathbf{F}) - \boldsymbol{\nabla} \times (\boldsymbol{\nabla} \times \mathbf{F}). \end{aligned} \tag{B.1.6}$$

B.2 Vector Wave Solutions for Electromagnetic Wave Scattering

The vector Helmholtz equation is: [1, 221]

$$\boldsymbol{\nabla}^2 \mathbf{C} + k^2 \mathbf{C} = 0, \tag{B.2.1}$$

where $\boldsymbol{\nabla}^2 \mathbf{C} = \boldsymbol{\nabla}\boldsymbol{\nabla} \cdot \mathbf{C} - \boldsymbol{\nabla} \times \boldsymbol{\nabla} \times \mathbf{C}$. Let the scalar function ψ be a member of a complete set of solutions of the scalar Helmholtz equation,

$$\boldsymbol{\nabla}^2 \psi + k^2 \psi = 0, \tag{B.2.2}$$

and let $\mathbf{a}$ be any constant vector of unit length. Three independent vector solutions of eq.B.2.1, $\mathbf{L}, \mathbf{M}, \mathbf{N}$ can be constructed from ψ as summarized in Table B.2.1.

An electromagnetic wave propagating in free space always satisfies eq.B.2.1, and therefore can be always represented as a linear combination of the characteristic vector functions $\mathbf{L}, \mathbf{M}, \mathbf{N}$. No coordinate is assumed yet. Conventionally, the electric and

	$\mathbf{L}$	$\mathbf{M}$	$\mathbf{N}$
construction:	$\mathbf{L} = \nabla\psi$	$\mathbf{M} = \nabla \times \mathbf{a}\psi$ $\mathbf{M} = \frac{1}{k}\nabla \times \mathbf{N}$ $\mathbf{M} = \mathbf{L} \times \mathbf{a}$	$\mathbf{N} = \frac{1}{k}\nabla \times \mathbf{M}$
properties:	$\nabla \times \mathbf{L} = 0$ $\nabla \cdot \mathbf{L} = \nabla^2\psi = -k^2\psi$	$\nabla \cdot \mathbf{M} = 0$ $\mathbf{L} \cdot \mathbf{M} = 0$	$\nabla \cdot \mathbf{N} = 0$

Table B.2.1: Characteristic vector wavefunctions.

magnetic fields are often expressed only in terms of $\mathbf{M}, \mathbf{N}$ and not of $\mathbf{L}$.

$$\mathbf{E} = -\sum_n (a_n \mathbf{M}_n + b_n \mathbf{N}_n) \tag{B.2.3}$$

$$\mathbf{H} = -\frac{k}{i\omega\mu}\sum_n (a_n \mathbf{N}_n + b_n \mathbf{M}_n) \tag{B.2.4}$$

Paraxial approximation of the wave equation

The wave equation **??** can be simplified if the wave is collimated along one direction (z). Let us specify the time difference and the direction of propagation as the following.

$$U(x, y, z, t) = u(x, y, z)e^{-i(kz-\omega t)} \tag{B.2.5}$$

Paraxial approximation states that $\partial^2 u/\partial z^2 = 0$, which gives the paraxial wave equation:

$$\frac{\partial^2 u}{\partial x^2} + \frac{\partial^2 u}{\partial y^2} = 2ik\frac{\partial u}{\partial z}. \tag{B.2.6}$$

B.3 Vector Cylindrical Wave Functions

A beam describes light that propagates in space and time with a confined spatial distribution in the radial direction. A beam is mathematically represented by the solution of the vector helmholtz equation in cylindrical coordinates. This section summarizes the analytical formulas of vector Bessel beams used in Chapter 3.

Let us define $\psi(\mathbf{r}, t)$ to be a simple plane wave solution:

$$\psi(\mathbf{r}, t) = \exp(i\mathbf{k} \cdot \mathbf{r} - i\omega t). \tag{B.3.1}$$

One way to construct $\mathbf{L}, \mathbf{M}, \mathbf{N}$ functions is to set$\mathbf{L}$ as a purely longitudinal wave. Then we obtain $\mathbf{L} = i\psi\mathbf{k}$, $\mathbf{M} = i\psi\mathbf{k} \times \mathbf{a}$, and $\mathbf{N} = \frac{1}{k}\psi(\mathbf{k} \times \mathbf{a}) \times \mathbf{k}$.

Beams with a Gaussian Envelope

A simple Gaussian beam can be expressed as:

$$E(r,z) = E_0 \frac{w_0}{w(z)} \exp\left(\frac{-r^2}{w(z)^2} - ikz - ik\frac{r^2}{2R(z)} + i\zeta(z)\right), \tag{B.3.2}$$

where the time dependence of $exp[i\omega t]$ is omitted.

r, z : radial, axial distance from center axis of the beam

$k = 2\pi/\lambda$: wavevector

$E_0 = |E(0,0)|$

$w(z)$: radius at which field amplitude drops to $1/e$ of the axial value.

- $w(z) = w_0\sqrt{1 + \left(\frac{z}{z_R}\right)^2}$
- $z_R = \frac{\pi w_0^2}{\lambda}$: Rayleigh range, $(w(\pm z_R) = \sqrt{2}w_0.)$
- $b = 2z_R = \frac{2\pi w_0^2}{\lambda}$: Beam depth of focus

$w_0 = w(0)$: waist size

$R(z) = z\left[1 + \left(\frac{z_R}{z}\right)^2\right]$: radius of curvature of beam's wavefronts

$\zeta(z) = \arctan\left(\frac{z}{z_R}\right)$: Gouy phase shift

Laguerre-Gaussian Beam

A Laguerre-Gaussian beam is cylindrically symmetric, and is a natural solution of the paraxial wave equation; written in cylindrical coordinates using Laguerre polynomials.

$$u(r,\phi,z) = \frac{C_{lp}^{LG}}{w(z)}\left(\frac{r\sqrt{2}}{w(z)}\right)^{|l|} \exp\left(-\frac{r^2}{w^2(z)}\right) L_p^{|l|}\left(\frac{2r^2}{w^2(z)}\right) \exp\left(ik\frac{r^2}{2R(z)}\right) e^{il\phi} e^{[i(2p+|l|+1)\zeta(z)]} \tag{B.3.3}$$

- l : azimuthal index
- p : radial index, $p \geq 0$
- C_{lp}^{LG} : normalization constant
- L_p^l : generalized Laguerre Polynomials
- Recurrence relation: $L_{k+1}(x) = \frac{(2k+1-x)L_k(x) - kL_{k-1}(x)}{k+1}$
- Closed form: $L_n(x) = \sum_{k=0}^{n} \binom{n}{k} \frac{(-1)^k}{k!} x^k$
- $z_{\mathrm{R}} = \frac{\pi w_0^2}{\lambda}$: Rayleigh range, $(w(\pm z_{\mathrm{R}}) = \sqrt{2} w_0.$)
- $b = 2z_{\mathrm{R}} = \frac{2\pi w_0^2}{\lambda}$: Beam depth of focus

Hermite-Gaussian Beam

Hermite Gaussian beams have a horizontal-vertical divide in the intensity profile, and is not radially symmetric.

$$u_n(x,z) = \left(\frac{2}{\pi}\right)^{1/4} \left(\frac{1}{2^n n! w_0} \frac{q_0}{q(z)}\right)^{1/2} \left[\frac{q_0}{q_0^*} \frac{q^*(z)}{q(z)}\right]^{n/2} H_n\left(\frac{\sqrt{2}x}{w(z)}\right) \exp\left[-i\frac{kx^2}{2q(z)}\right] \tag{B.3.4}$$

where the complex beam parameter $q(z)$ is defined as $q(z) = z + q_0 = z + iz_{\mathrm{R}}$.

- For $q(z)$, there is a following relationship:

$$\frac{1}{q(z)} = \frac{1}{R(z)} - i\frac{\lambda}{\pi w^2(z)}.$$

- We use the physicists' Hermite polynomial instead of the probabilists' version.

$$H_n(x) = (-1)^n e^{x^2} \frac{d^n}{dx^n} e^{-x^2} = \left(2x - \frac{d}{dx}\right)^n \cdot 1$$

- Hermite function in 1D:

$$\psi_n(x) = \left(2^n n! \sqrt{\pi}\right)^{-\frac{1}{2}} e^{-\frac{x^2}{2}} H_n(x) = (-1)^n \left(2^n n! \sqrt{\pi}\right)^{-\frac{1}{2}} e^{\frac{x^2}{2}} \frac{d^n}{dx^n} e^{-x^2}.$$

Bessel Beam

The amplitude of a Bessel beam is described as the Bessel function of the 1st kind. Bessel functions are known as cylinder functions or cylindrical harmonics because they appear in the solution to Laplace's equation in cylindrical coordinates.

- Bessel's D.E.: $x^2\frac{d^2y}{dx^2} + x\frac{dy}{dx} + (x^2 - \alpha^2)y = 0$
- $J_{-n}(x) = (-1)^n J_n(x)$.
- Another definition of Bessel function can be obtained from the Bessel's integrals: $J_n(x) = \frac{1}{\pi}\int_0^\pi \cos(n\tau - x\sin(\tau))\,d\tau$, or $J_n(x) = \frac{1}{2\pi}\int_{-\pi}^\pi e^{i(n\tau - x\sin(\tau))}\,d\tau$.

A Bessel beam is defined using the following parameters.

- Beam aperture angle $\alpha = \tan^{-1}(k_z/k_t)$
- Beam propagation direction $\hat{n} = \mathbf{k}/k$
- Beam center (x_0, y_0, z_0)

The scalar generating function for a Bessel beam describes the amplitude distribution of Bessel beams:

$$\psi_m(r, \phi, z) = J_m(k_t r)\exp(im\phi + ik_z z), \tag{B.3.5}$$

where J_m is the mth-order Bessel function

$$J_m(x) = \sum_{n=0}^{\infty} \frac{(-1)^n}{n!\,\Gamma(n+m+1)}\left(\frac{x}{2}\right)^{2n+m} \tag{B.3.6}$$

with $\Gamma(z)$ being the Gamma function. By taking the arbitrary constant vector $\mathbf{a}$ is the unit vector in z direction, we obtain the following vector cylindrical harmonic wave functions.

$$\mathbf{M}_m = \frac{k_t}{2}\{i(J_{m-1} + J_{m+1})\hat{r} - (J_{m-1} - J_{m+1})\hat{\phi}\}e^{ik_z z + im\phi} \tag{B.3.7a}$$

$$\mathbf{N}_m = \frac{k_t}{2k}\{ik_z(J_{m-1} - J_{m+1})\hat{r} - k_z(J_{m-1} + J_{m+1})\hat{\phi} + 2k_t J_m \hat{z}\}e^{ik_z z + im\phi} \tag{B.3.7b}$$

Appendix C

Explicit Action-response Equations for Acoustic Nonlocal Theory

This chapter is based on: N. Nemati, Y. E. Lee, D. Lafarge, A. Duclos, and N. X. Fang, "Nonlocal dynamics of dissipative phononic fluids," Phys. Rev. B., Accepted for publication on 10 May 2017

C.1 Explicit Action-response Equations

The variables used in this chapter are defined in Chapter (5). To obtain the nonlocal effective density $\rho(\omega, k)$, we solve the following PDEs involving only the amplitude fields of the form $p(\omega, k, \boldsymbol{r})$ in $p(t, x) = p(\omega, k, \boldsymbol{r})e^{-i\omega t + ikx}$, and so on for the fields $\boldsymbol{v}$, b, and τ.

$$i\omega b = \boldsymbol{\nabla}.\boldsymbol{v} - ikv_x \tag{C.1.1a}$$

$$-i\omega\rho_0\boldsymbol{v} = -\boldsymbol{\nabla}p - ikp\boldsymbol{e}_x + \eta\boldsymbol{\nabla}^2\boldsymbol{v} + 2ik\eta\frac{\partial \boldsymbol{v}}{\partial x} - \eta k^2\boldsymbol{v} + \left(\zeta + \frac{1}{3}\eta\right)\boldsymbol{\nabla}(\boldsymbol{\nabla}.\boldsymbol{v}) \tag{C.1.1b}$$

$$+ik\left(\zeta + \frac{1}{3}\eta\right)(\boldsymbol{\nabla}.\boldsymbol{v})\boldsymbol{e}_x + ik\left(\zeta + \frac{1}{3}\eta\right)\boldsymbol{\nabla}v_x - \left(\zeta + \frac{1}{3}\eta\right)k^2v_x\boldsymbol{e}_x - ik\boldsymbol{e}_x\mathcal{P}_0$$

$$-i\omega\rho_0c_p\tau = -i\omega\beta_0T_0p + \kappa\boldsymbol{\nabla}^2\tau + 2ik\kappa\partial_x\tau - k^2\kappa\tau \tag{C.1.1c}$$

$$\gamma\chi_0p = b + \beta_0\tau \tag{C.1.1d}$$

The boundary condition is:

$$\boldsymbol{v} = 0,\ \tau = 0 \qquad \text{on } \partial\mathcal{V}. \tag{C.1.2}$$

To compute the nonlocal effective bulk modulus $\chi^{-1}(\omega, k)$, we solve

$$\begin{aligned}
i\omega b &= \boldsymbol{\nabla}.\boldsymbol{v} + ikv_x && \text{(C.1.3a)}\\
-i\omega\rho_0\boldsymbol{v} &= -\boldsymbol{\nabla}p - ikp\boldsymbol{e}_x + \eta\boldsymbol{\nabla}^2\boldsymbol{v} + 2ik\eta\frac{\partial \boldsymbol{v}}{\partial x} - \eta k^2\boldsymbol{v} + \left(\zeta + \frac{1}{3}\eta\right)\boldsymbol{\nabla}(\boldsymbol{\nabla}.\boldsymbol{v}) && \text{(C.1.3b)}\\
&\quad +ik\left(\zeta + \frac{1}{3}\eta\right)(\boldsymbol{\nabla}.\boldsymbol{v})\boldsymbol{e}_x + ik\left(\zeta + \frac{1}{3}\eta\right)\boldsymbol{\nabla}v_x - \left(\zeta + \frac{1}{3}\eta\right)k^2 v_x\boldsymbol{e}_x\\
-i\omega\rho_0 c_p\tau &= -i\omega\beta_0 T_0 p + \kappa\boldsymbol{\nabla}^2\tau + 2ik\kappa\frac{\partial\tau}{\partial x} - k^2\kappa\tau - i\omega\beta_0 T_0\mathcal{P}_0 && \text{(C.1.3c)}\\
\gamma\chi_0 p &= b + \beta_0\tau && \text{(C.1.3d)}
\end{aligned}$$

in $\mathcal{V}_f$, subject to

$$\boldsymbol{v} = 0,\ \tau = 0 \qquad \text{on } \partial\mathcal{V}. \tag{C.1.4}$$

C.2 Direct Bloch-wave approach

Here, we aim to obtain the phase velocity of the least attenuated Bloch wave propagating in the 2D fluid/solid reference phononic crystal illustrated in Figure 5.1.1, solving directly the source-free microscopic equations in Eq. (5.2.2)-(5.2.7). Achieving the Bloch wavenumber $k_B(\omega)$ as eigenvalue of the medium, through direct Bloch-wave approach, is fundamentally different from the way we obtain this quantity based on local and nonlocal theories, via Eq. (5.2.34), and Eq. (5.2.43). These theories *define* in an appropriate manner, the effective susceptibilities of the media (effective density, bulk modulus), that concern macroscopic response of a medium to an applied field. Within these theories, procedures are established to determine the way in which the effective density and bulk modulus can be obtained based on micro level 'action-response' problems. Once the effective parameters are obtained, the effective

wavenumbers can be achieved, thus, in an *indirect* fashion. In contrast, as direct Bloch-wave approach is not based on a macroscopic theory it cannot by itself *define*, independently, the effective susceptibilities of the material.

For the simple fluid/solid geometry illustrated in Figure 5.1.1 a precise and relatively simple calculation of the possible Bloch wavenumbers $k_n(\omega)$ is feasible by the multiple scattering approach [222]. We sketch here the generalization of the multiple scattering approach developed in [223] for a lossless host fluid and the same geometry to the present case of a viscothermal fluid. The fluid motion corresponding to the source-free equations in Eq. (5.2.2)-(5.2.7), can be described in terms of three velocity potentials: the acoustic potential ϕ^a, entropic potential ϕ^e and vorticity potential $\boldsymbol{\psi}$ such that

$$\boldsymbol{v} = \boldsymbol{\nabla}\left(\phi^a + \phi^e\right) + \boldsymbol{\nabla} \times \boldsymbol{\psi} \tag{C.2.1}$$

The vorticity potential $\boldsymbol{\psi}$ has just one component, which is directed along the z-axis and is denoted by ϕ^v. In harmonic regime, three independent Helmholtz equations

$$\left[\boldsymbol{\nabla}^2 + (k^\alpha)^2\right]\phi^\alpha = 0, \qquad \alpha = a, e, v \tag{C.2.2}$$

must be satisfied in $\mathcal{V}^f$, where $(k^\alpha)^2$, $\alpha = a, e, v$, are the squared wavenumbers associated with acoustic, thermal and viscous waves, respectively. The former two $(k^a)^2$ and $(k^e)^2$ are the opposite-sign of the small and large solutions $\lambda_1 \equiv \lambda^a$ and $\lambda_2 \equiv \lambda^e$ of Kirchhoff-Langevin's dispersion equation (see Eq. (14) in [198]), and the latter is $(k^v)^2 \equiv i\omega/\nu$, where $\nu = \eta/\rho_0$ is the kinematic viscosity. It is easy to express the excess temperature in terms of potentials, for instance, by using Eqs. (C.2.1) and (C.2.2), as well as Eq. (12c) in [198]:

$$\frac{\beta_0 \tau}{\gamma - 1} = \left(\frac{\kappa}{\rho_0 c_v} + \frac{i\omega}{\lambda^a}\right)^{-1}\phi^a + \left(\frac{\kappa}{\rho_0 c_v} + \frac{i\omega}{\lambda^e}\right)^{-1}\phi^e \tag{C.2.3}$$

The boundary conditions at the solid-fluid interface for the potentials arise from the

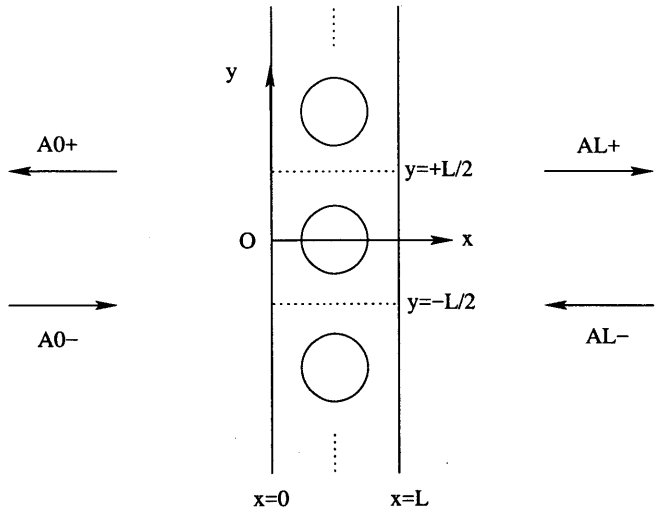

Figure C.2.1: A schematic of wave sscattering by one row infinite number of rigid cylinders. The incoming and outgoing waves in $+x$ and $-x$ directions are labeled with arrows. The periodicity of one unit cell is L.

fact that the displacement $\boldsymbol{u}$ and excess temperature fields vanish on $\partial\mathcal{V}$

$$\boldsymbol{u} = \mathbf{0}, \qquad \tau = 0 \tag{C.2.4}$$

These boundary conditions establish the relationship between the potentials, such that a wave carried by one potential is scattered in the three types of waves through interacting with the solid cylinders.

We are not concerned with the terms of minor importance related to the intrinsic bulk fluid attenuation. Thus, as a simplification we set $-\lambda^a \equiv (k^a)^2 = (\omega/c_0)^2$, that is, we neglect the damping of the acoustic mode. After straightforward calculation using the thermodynamic identity $\gamma - 1 = T_0\beta_0^2 c_0^2/c_p$, we obtain: $\tau = (T_0\beta_0/c_p)i\omega\phi^a + (\rho_0 c_p/\beta_0\kappa)\phi^e$.

Considering one row containing an infinite number of cylinders, as is shown in Figure C.2.1, we expand the potentials in terms of right and left going plane waves

$$\phi_0^\alpha(\boldsymbol{r}) = \sum_{n=-\infty}^{\infty} \left(A_{0n}^{+\alpha} e^{i\boldsymbol{k}_n^\alpha \cdot \boldsymbol{r}} + A_{0n}^{-\alpha} e^{-i\boldsymbol{k}_n^\alpha \cdot \boldsymbol{r}}\right)$$

$$\phi_L^\alpha(\boldsymbol{r}) = \sum_{n=-\infty}^{\infty} \left(A_{Ln}^{+\alpha} e^{i\boldsymbol{k}_n^\alpha \cdot (\boldsymbol{r}-L\boldsymbol{e}_x)} + A_{Ln}^{-\alpha} e^{-i\boldsymbol{k}_n^\alpha \cdot (\boldsymbol{r}-L\boldsymbol{e}_x)}\right)$$

The incoming or outgoing of the four types of amplitudes A are illustrated in Figure C.2.1. The index α refers to the type a, e, or v of potential field. It is clear that the periodicity of the potential fields with respect to y-coordinates implies that for each n the y-component of the wavevectors $\boldsymbol{k}_n^\alpha$ must be $k_{ny}^\alpha = 2\pi n/L$, thus $(k^\alpha)^2 = (k_{nx}^\alpha)^2 + (2\pi n/L)^2$. Another symmetry consideration of the problem is based on the fact that we are interested only with the solutions leading to a fluid motion symmetric around each cylinder. This restriction implies that the fields ϕ^a and ϕ^e are even functions, and ϕ^v an odd function, of y coordinates. Thus, regarding the terms in the above equations, after combining the up and down components n and $-n$, there will appear a y-dependence in the form of $\cos(2\pi ny/L)$ for acoustic and entropic potentials, and in the form of $\sin(2\pi ny/L)$ for vorticity potential. To account explicitly for this symmetry in the notation, we replace the above equations by the following condensed form of the potentials

$$\phi_0^\alpha(\boldsymbol{r}) = \sum_{n=0}^{\infty} \mathcal{C}_n^\alpha(y) \left(A_{0n}^{+\alpha} e^{ik_{nx}^\alpha x} + A_{0n}^{-\alpha} e^{-ik_{nx}^\alpha x}\right)$$

$$\phi_L^\alpha(\boldsymbol{r}) = \sum_{n=0}^{\infty} \mathcal{C}_n^\alpha(y) \left(A_{Ln}^{+\alpha} e^{ik_{nx}^\alpha (x-L)} + A_{Ln}^{-\alpha} e^{-ik_{nx}^\alpha (x-L)}\right)$$

$$\text{where} \quad \mathcal{C}_n^\alpha(y) = \begin{cases} \cos(2\pi ny/L), & \alpha = a, e \\ \sin(2\pi ny/L), & \alpha = v \end{cases}$$

Also, we note that with each n, α, and ω, we may associate a characteristic incidence angle θ_n^α, such that $k^\alpha \sin(\theta_n^\alpha) = 2\pi n/L$, and $k^\alpha \cos(\theta_n^\alpha) = k_{nx}^\alpha$. For the acoustic type $\alpha = a$, this angle is real when the frequency is such that $2\pi n/(k^\alpha L) < 1$. It is complex and equal to $\pi/2 - i\xi$ at higher frequencies, with $\xi > 0$ ensuring that $\mathrm{Im}(k_{nx}^\alpha) > 0$. For the entropic and vorticity types, this angle is complex, which is chosen to satisfy

$\mathrm{Im}(k_{nx}^{\alpha}) > 0$.

The first step in the calculation is to obtain the reflection and transmission properties of the row of cylinders, or the following scattering matrix, which relates the outgoing waves to the incoming ones

$$\begin{pmatrix} \boldsymbol{A}_0^- \\ \boldsymbol{A}_L^+ \end{pmatrix} = \begin{pmatrix} \boldsymbol{T} & \boldsymbol{R} \\ \boldsymbol{R} & \boldsymbol{T} \end{pmatrix} \begin{pmatrix} \boldsymbol{A}_L^- \\ \boldsymbol{A}_0^+ \end{pmatrix} \tag{C.2.7}$$

$$\text{where} \quad \boldsymbol{A}_0^- = \begin{pmatrix} \boldsymbol{A}_0^{-a} \\ \boldsymbol{A}_0^{-e} \\ \boldsymbol{A}_0^{-v} \end{pmatrix}, \qquad \boldsymbol{A}_L^+ = \begin{pmatrix} \boldsymbol{A}_L^{+a} \\ \boldsymbol{A}_L^{+e} \\ \boldsymbol{A}_L^{+v} \end{pmatrix}$$

and so on for the vectors $\boldsymbol{A}_0^+$ and $\boldsymbol{A}_L^-$. Each of the vectors $\boldsymbol{A}_L^{+\alpha}$, $\boldsymbol{A}_0^{+\alpha}$, $\boldsymbol{A}_L^{-\alpha}$, and $\boldsymbol{A}_0^{-\alpha}$ contains the whole ensemble of plane wave amplitudes with $\alpha = a, e, v$, each of which is indexed by n. The reflection and transmission matrices $\boldsymbol{R}$ and $\boldsymbol{T}$, respectively, thus have elements of the type $R_{pn}^{\alpha\beta}$ and $T_{pn}^{\alpha\beta}$, where the indexes on the right refer to incoming waves and those on the left to outgoing waves. The presence of different elements results from the interactions and transformations of different kinds of potentials into one another, via boundary conditions in Eq. (C.2.4).

To compute $\boldsymbol{R}$ and $\boldsymbol{T}$, and thereby construct the scattering matrix, the analysis of the scattering problem is divided in different elementary parts, that are combined in the end. At this point, reflection and transmission properties of one row are entirely determined. Now, we consider an infinite number of rows separated by the distance L (Figure 5.1.1). We make use of the concept of scattering matrix introduced for an arbitrary row, and apply the Bloch condition for this case of periodic medium. We have

$$\begin{pmatrix} \boldsymbol{A}_L^+ \\ \boldsymbol{A}_L^- \end{pmatrix} = e^{ik_B L} \begin{pmatrix} \boldsymbol{A}_0^+ \\ \boldsymbol{A}_0^- \end{pmatrix} \tag{C.2.8}$$

where k_B denotes the Bloch wavenumber to be determined. The use of scattering-matrix relation Eq. (C.2.7) and the Bloch condition Eq. (C.2.8) leads to the following

eigenvalue problem

$$\begin{pmatrix} \boldsymbol{T} & \boldsymbol{R} \\ \boldsymbol{0} & \boldsymbol{I} \end{pmatrix} \begin{pmatrix} \boldsymbol{A}_0^+ \\ \boldsymbol{A}_L^- \end{pmatrix} = e^{ik_B L} \begin{pmatrix} \boldsymbol{I} & \boldsymbol{0} \\ \boldsymbol{R} & \boldsymbol{T} \end{pmatrix} \begin{pmatrix} \boldsymbol{A}_0^+ \\ \boldsymbol{A}_L^- \end{pmatrix} \tag{C.2.9}$$

where $\boldsymbol{0}$ and $\boldsymbol{I}$ are the zero and identity matrices, respectively.

Since at this stage the reflection and transmission matrices $\boldsymbol{R}$ and $\boldsymbol{T}$ are known, we are able to solve the above eigenvalue problem numerically. In this manner we get the complex eigenvalues $\mu = e^{ik_B L}$ that determine the possible Bloch wavenumbers k_B. For each eigenvalue μ there must be an eigenvalue μ^{-1} corresponding to the opposite sign of k_B, *i.e.,* the reversed direction of propagation. We restrict the solutions to forward propagation by imposing $|\mu| < 1$ and $\mathrm{Im}(k_B) > 0$. Note that the real part of the wavenumber is defined only modulo $2\pi/L$. Customarily, this indeterminacy issue is resolved by requiring that $-\pi/L < \mathrm{Re}(k_B) < \pi/L$, *i.e.,* the wavenumber is chosen to lie in the first Brillouin zone. With each frequency ω there might be associated, in the first Brillouin zone, different mode solutions $k_{B,n}$, $n = 1, 2, 3, ...$, labeled by ascending order of the values of $\mathrm{Im}(k_{B,n})$, and characterized by complex phase velocities

$$c_n(\omega) = \frac{\omega}{k_{B,n}(\omega)} \tag{C.2.10}$$

Here, however, we study the least attenuated mode $n = 1$, propagating in the positive x direction, and find it convenient to express its wavenumber $k_B \equiv k_{B,1}(\omega)$ as a continuous function of frequency, that becomes zero when the frequency tends to zero. The wavenumber $k_B(\omega)$ that is defined in this manner, will not always remain in the first Brillouin zone. As it will be shown in the next section, when the frequency increases sufficiently, the real part of the wavenumber may be found in the interval $[\pi/L, 2\pi/L]$ (or upper), which means that it passes into the second (or higher) Brillouin zone. The same convention will be applied regarding the selection and presentation of the wavenumbers in nonlocal computation, where, obviously, the same issues arise.

Appendix D

List of Acronyms

- 1d, 2d, 3d: one-, two-, three-dimensional
- ALD: atomic layer deposition
- BEM: boundary element method
- BOBYQA: bound optimization by quadratic approximation
- CAD/CAM: computer-aided design/manufacturing
- CMP: chemical mechanical polishing
- COBYLA: constrained optimization by linear approximation
- CP: circularly polarized, circular polarization
- CVD: chemical vapor deposition
- DMD: digital mirror display
- FDFD: finite-difference frequency domain
- FDTD: finite-difference time domain
- FEM: finite element method
- FIB: focused ion beam
- FIR: far infrared
- FOM: figure of merit
- FTIR: fourier transform infrared

- IR: infrared
- MAPhC: metallic-air photonic crystal
- MDPhC: metallic-dielectric photonic crystal
- NA: numerical aperture
- NEP: nonlinear eigenvalue problem
- NIR: near infrared
- PDE: partial differential equation
- PW: planewave
- SEM: scanning electron microscopy
- SLM: spatial light modulator
- SPP: surface plasmon polariton
- STPV: solar-thermophotovoltaic
- UV: ultraviolet
- UV-VIS-NIR: ultraviolet-visible-near infrared
- VCWF: vector cylindrical-harmonic wavefunction
- VIS: visible (spectrum)
- VSWF: vector spherical-harmonic wavefunction

Bibliography

[1] J.D. Jackson, *Classical Electrodynamics.* Wiley New York, 3 ed.

[2] J. A. Stratton, *Electromagnetic theory.* John Wiley & Sons.

[3] M. F. Modest, *Radiative heat transfer.* Academic press.

[4] A. D. Pierce, *Acoustics: an introduction to its physical principles and applications*, vol. 20. McGraw-Hill New York.

[5] K. L. Kelly, E. Coronado, L. L. Zhao, and G. C. Schatz, "The optical properties of metal nanoparticles: the influence of size, shape, and dielectric environment," vol. 107, no. 3, pp. 668–677.

[6] C. J. Murphy, T. K. Sau, A. M. Gole, C. J. Orendorff, J. Gao, L. Gou, S. E. Hunyadi, and T. Li, "Anisotropic metal nanoparticles: Synthesis, assembly, and optical applications," vol. 109, no. 29, pp. 13857–13870.

[7] Y. Xia and N. J. Halas, "Shape-controlled synthesis and surface plasmonic properties of metallic nanostructures," vol. 30, no. 5, pp. 338–348.

[8] C. L. Nehl, H. Liao, and J. H. Hafner, "Optical properties of star-shaped gold nanoparticles," vol. 6, no. 4, pp. 683–688.

[9] H. Wang, Y. Wu, B. Lassiter, C. L. Nehl, J. H. Hafner, P. Nordlander, and N. J. Halas, "Symmetry breaking in individual plasmonic nanoparticles," vol. 103, no. 29, pp. 10856–10860.

[10] S. Zeng, K. T. Yong, I. Roy, X. Q. Dinh, X. Yu, and F. Luan, "A review on functionalized gold nanoparticles for biosensing applications," vol. 6, no. 3, pp. 491–506.

[11] O. Miller, C. Hsu, M. Reid, W. Qiu, B. DeLacy, J. Joannopoulos, M. Soljačić, and S. Johnson, "Fundamental limits to extinction by metallic nanoparticles," vol. 112, no. 12, p. 123903.

[12] J. D. Joannopoulos, S. G. Johnson, J. N. Winn, and R. D. Meade, *Photonic crystals: molding the flow of light.* Princeton university press.

[13] S. A. Maier, *Plasmonics: fundamentals and applications.* Springer Science & Business Media.

[14] N. Fang, D. Xi, J. Xu, M. Ambati, W. Srituravanich, C. Sun, and X. Zhang, "Ultrasonic metamaterials with negative modulus," vol. 5, no. 6, pp. 452–456.

[15] N. R. Heckenberg, R. McDuff, C. P. Smith, and A. G. White, "Generation of optical phase singularities by computer-generated holograms," vol. 17, no. 3, pp. 221–223.

[16] J. E. Curtis, B. A. Koss, and D. G. Grier, "Dynamic holographic optical tweezers," vol. 207, no. 1, pp. 169–175.

[17] R. Di Leonardo, F. Ianni, and G. Ruocco, "Computer generation of optimal holograms for optical trap arrays," vol. 15, no. 4, pp. 1913–1922.

[18] Q. Zhan, "Cylindrical vector beams: from mathematical concepts to applications," vol. 1, no. 1, pp. 1–57.

[19] H. Chen, J. Hao, B.-F. Zhang, J. Xu, J. Ding, and H.-T. Wang, "Generation of vector beam with space-variant distribution of both polarization and phase," vol. 36, no. 16, pp. 3179–3181.

[20] I. Dolev, I. Epstein, and A. Arie, "Surface-plasmon holographic beam shaping," vol. 109, no. 20, p. 203903.

[21] S. A. Schulz, T. Machula, E. Karimi, and R. W. Boyd, "Integrated multi vector vortex beam generator," vol. 21, no. 13, pp. 16130–16141.

[22] C.-F. Chen, C.-T. Ku, Y.-H. Tai, P.-K. Wei, H.-N. Lin, and C.-B. Huang, "Creating optical near-field orbital angular momentum in a gold metasurface," vol. 15, no. 4, pp. 2746–2750.

[23] D. P. Bertsekas, *Nonlinear programming.* Athena scientific Belmont.

[24] S. G. Johnson, *The NLopt nonlinear-optimization package.*

[25] M. T. Homer Reid and S. G. Johnson, "Efficient computation of power, force, and torque in BEM scattering calculations,"

[26] F. Hecht, "New development in FreeFem++," vol. 20, no. 3, pp. 251–266.

[27] Y.-l. Xu, "Electromagnetic scattering by an aggregate of spheres," vol. 34, no. 21, pp. 4573–4588.

[28] "Lumerical solutions, inc. http://www.lumerical.com/tcad-products/fdtd/."

[29] Y. K. E. Lee, "Light-induced torque at multipolar plasmon resonance," Master's thesis.

[30] L. D. Landau and E. M. Lifshitz, *Fluid mechanics.* Pergamon press London.

[31] E. D. Palik, *Handbook of optical constants of solids*, vol. 3. Academic press.

[32] K. Yee, "Numerical solution of initial boundary value problems involving maxwell's equations in isotropic media," vol. 14, no. 3, pp. 302–307.

[33] A. Taflove and S. C. Hagness, *Computational Electrodynamics: The Finite-Difference Time-Domain Method.* Artech House, Boston, MA, USA, 3 ed.

[34] O. C. Zienkiewicz, R. L. Taylor, and R. L. Taylor, *The finite element method*, vol. 3. McGraw-hill London.

[35] W. C. Chew, M. S. Tong, and B. Hu, "Integral equation methods for electromagnetic and elastic waves," vol. 3, no. 1, pp. 1–241.

[36] R. F. Harrington and J. L. Harrington, *Field computation by moment methods.* Oxford University Press.

[37] W. Zhang, C. T. Chan, and P. Sheng, "Multiple scattering theory and its application to photonic band gap systems consisting of coated spheres," vol. 8, no. 3, pp. 203–208.

[38] J. H. Bruning and Y. T. Lo, "Multiple scattering of EM waves by spheres part i–multipole expansion and ray-optical solutions," vol. 19, no. 3, pp. 378–390.

[39] R. Sainidou, N. Stefanou, I. Psarobas, and A. Modinos, "A layer-multiple-scattering method for phononic crystals and heterostructures of such," vol. 166, no. 3, pp. 197–240.

[40] L. N. Trefethen and D. Bau III, *Numerical linear algebra*, vol. 50. Siam.

[41] F. Tisseur and K. Meerbergen, "The quadratic eigenvalue problem," vol. 43, no. 2, pp. 235–286.

[42] V. Mehrmann and H. Voss, "Nonlinear eigenvalue problems: A challenge for modern eigenvalue methods," vol. 27, no. 2, pp. 121–152.

[43] M. G. Silveirinha, "Metamaterial homogenization approach with application to the characterization of microstructured composites with negative parameters," vol. 75, no. 11, p. 115104.

[44] A. N. Norris, A. Shuvalov, and A. Kutsenko, "Analytical formulation of three-dimensional dynamic homogenization for periodic elastic systems," in *Proc. R. Soc. A*, vol. 468, pp. 1629–1651, The Royal Society.

[45] M. Yang, G. Ma, Y. Wu, Z. Yang, and P. Sheng, "Homogenization scheme for acoustic metamaterials," vol. 89, no. 6.

[46] M. Born and E. Wolf, *Principles of optics: electromagnetic theory of propagation, interference and diffraction of light.* Elsevier.

[47] V. M. Agranovich and V. L. Ginzburg, *Spatial dispersion in crystal optics and the theory of excitons.* Interscience New York.

[48] P. Belov, R. Marques, S. Maslovski, I. Nefedov, M. Silveirinha, C. Simovski, and S. Tretyakov, "Strong spatial dispersion in wire media in the very large wavelength limit," vol. 67, no. 11, p. 113103.

[49] Y. E. Lee, K. H. Fung, D. Jin, and N. X. Fang, "Optical torque from enhanced scattering by multipolar plasmonic resonance," vol. 3, no. 6, pp. 343–440.

[50] M. J. Powell, "A fast algorithm for nonlinearly constrained optimization calculations," in *Numerical analysis*, pp. 144–157, Springer.

[51] D. Lafarge and N. Nemati, "Nonlocal maxwellian theory of sound propagation in fluid-saturated rigid-framed porous media," vol. 50, no. 6, pp. 1016–1035.

[52] J. C. Maxwell, *A Treatise on Electricity and Magnetism*, vol. 1. Oxford, Clarendon Press.

[53] J. H. Poynting, "On the transfer of energy in the electromagnetic field," vol. 175, pp. 343–361.

[54] C. F. Bohren and D. R. Huffman, *Absorption and scattering of light by small particles*. Wiley-VCH Verlag GmbH & Co. KGaA, Weinheim.

[55] J. R. Arias-Gonzalez and M. Nieto-Vesperinas, "Optical forces on small particles: attractive and repulsive nature and plasmon-resonance conditions," vol. 20, no. 7, pp. 1201–1209.

[56] J. Chen, J. Ng, Z. Lin, and C. Chan, "Optical pulling force," vol. 5, no. 9, pp. 531–534.

[57] A. Novitsky, C.-W. Qiu, and H. Wang, "Single gradientless light beam drags particles as tractor beams," vol. 107, no. 20, p. 203601.

[58] S. Sukhov and A. Dogariu, "Negative nonconservative forces: Optical "tractor beams" for arbitrary objects," vol. 107, no. 20, p. 203602.

[59] A. Ashkin, "Acceleration and trapping of particles by radiation pressure," vol. 24, no. 4, pp. 156–159.

[60] D. G. Grier, "A revolution in optical manipulation," vol. 424, no. 6950, pp. 810–816.

[61] S. Franke-Arnold, L. Allen, and M. Padgett, "Advances in optical angular momentum," vol. 2, no. 4, pp. 299–313.

[62] M. Padgett and R. Bowman, "Tweezers with a twist," vol. 5, no. 6, pp. 343–348.

[63] J. Poynting, "The wave motion of a revolving shaft, and a suggestion as to the angular momentum in a beam of circularly polarised light," vol. 82, no. 557, pp. 560–567.

[64] R. A. Beth, "Mechanical detection and measurement of the angular momentum of light," vol. 50, no. 2, p. 115.

[65] L. Allen, M. Beijersbergen, R. Spreeuw, and J. Woerdman, "Orbital angular momentum of light and the transformation of laguerre-gaussian laser modes," vol. 45, no. 11, pp. 8185–8189.

[66] L. Allen, S. M. Barnett, and M. J. Padgett, *Optical angular momentum.* CRC Press.

[67] N. Simpson, K. Dholakia, L. Allen, and M. Padgett, "Mechanical equivalence of spin and orbital angular momentum of light: an optical spanner," vol. 22, no. 1, pp. 52–54.

[68] V. Bingelyte, J. Leach, J. Courtial, and M. Padgett, "Optically controlled three-dimensional rotation of microscopic objects," vol. 82, no. 5, pp. 829–831.

[69] M. Friese, T. Nieminen, N. Heckenberg, and H. Rubinsztein-Dunlop, "Optical alignment and spinning of laser-trapped microscopic particles," vol. 394, no. 6691, pp. 348–350.

[70] Y. Arita, M. Mazilu, and K. Dholakia, "Laser-induced rotation and cooling of a trapped microgyroscope in vacuum," vol. 4.

[71] A. La Porta and M. D. Wang, "Optical torque wrench: angular trapping, rotation, and torque detection of quartz microparticles," vol. 92, no. 19, p. 190801.

[72] Z.-P. Luo, Y.-L. Sun, and K.-N. An, "An optical spin micromotor," vol. 76, no. 13, p. 1779.

[73] E. Higurashi, H. Ukita, H. Tanaka, and O. Ohguchi, "Optically induced rotation of anisotropic micro-objects fabricated by surface micromachining," vol. 64, no. 17, pp. 2209–2210.

[74] P. Galajda and P. Ormos, "Complex micromachines produced and driven by light," vol. 78, no. 2, p. 249.

[75] M. Khan, A. K. Sood, F. L. Deepak, and C. N. R. Rao, "Nanorotors using asymmetric inorganic nanorods in an optical trap," vol. 17, no. 11, pp. S287–S290.

[76] S. Parkin, T. A. Nieminen, V. L. Loke, N. R. Heckenberg, and H. Rubinsztein-Dunlop, "Integrated optomechanical microelements," vol. 15, no. 9, pp. 5521–5530.

[77] J. Chen, J. Ng, K. Ding, K. H. Fung, Z. Lin, and C. T. Chan, "Negative optical torque," vol. 4, p. 06386.

[78] P. M. Hansen, V. K. Bhatia, N. Harrit, and L. Oddershede, "Expanding the optical trapping range of gold nanoparticles," vol. 5, no. 10, pp. 1937–1942.

[79] L. Tong, V. D. Miljkovic´, and M. Ka¨ll, "Alignment, rotation, and spinning of single plasmonic nanoparticles and nanowires using polarization dependent optical forces," vol. 10, no. 1, pp. 268–273.

[80] P. H. Jones, F. Palmisano, F. Bonaccorso, P. G. Gucciardi, G. Calogero, A. C. Ferrari, and O. M. Maragò, "Rotation detection in light-driven nanorotors," vol. 3, no. 10, pp. 3077–3084.

[81] M. Liu, T. Zentgraf, Y. Liu, G. Bartal, and X. Zhang, "Light-driven nanoscale plasmonic motors," vol. 5, no. 8, pp. 570–573.

[82] W. L. Barnes, A. Dereux, and T. W. Ebbesen, "Surface plasmon subwavelength optics," vol. 424, no. 6950, pp. 824–830.

[83] A. Lehmuskero, R. Ogier, T. Gschneidtner, P. Johansson, and M. Ka¨ll, "Ultrafast spinning of gold nanoparticles in water using circularly polarized light," vol. 13, no. 7, pp. 3129–3134.

[84] L. Novotny, R. X. Bian, and X. S. Xie, "Theory of nanometric optical tweezers," vol. 79, no. 4, pp. 645–648.

[85] M. Righini, G. Volpe, C. Girard, D. Petrov, and R. Quidant, "Surface plasmon optical tweezers: tunable optical manipulation in the femtonewton range," vol. 100, no. 18, p. 186804.

[86] K. Wang, E. Schonbrun, P. Steinvurzel, and K. B. Crozier, "Trapping and rotating nanoparticles using a plasmonic nano-tweezer with an integrated heat sink," vol. 2, p. 469.

[87] A. A. E. Saleh and J. A. Dionne, "Toward efficient optical trapping of sub-10-nm particles with coaxial plasmonic apertures," vol. 12, no. 11, pp. 5581–5586.

[88] W.-Y. Tsai, J.-S. Huang, and C.-B. Huang, "Selective trapping or rotation of isotropic dielectric micro-particles by optical near field in a plasmonic archimedes spiral," p. 140106122927003.

[89] L. Novotny and N. van Hulst, "Antennas for light," vol. 5, no. 2, pp. 83–90.

[90] K. D. Ko, A. Kumar, K. H. Fung, R. Ambekar, G. L. Liu, N. X. Fang, and K. C. Toussaint, "Nonlinear optical response from arrays of au bowtie nanoantennas," vol. 11, no. 1, pp. 61–65.

[91] L. Huang, X. Chen, H. Mühlenbernd, G. Li, B. Bai, Q. Tan, G. Jin, T. Zentgraf, and S. Zhang, "Dispersionless phase discontinuities for controlling light propagation," vol. 12, no. 11, pp. 5750–5755.

[92] N. Yu, F. Aieta, P. Genevet, M. A. Kats, Z. Gaburro, and F. Capasso, "A broadband, background-free quarter-wave plate based on plasmonic metasurfaces," vol. 12, no. 12, pp. 6328–6333.

[93] E. K. Payne, K. L. Shuford, S. Park, G. C. Schatz, and C. A. Mirkin, "Multipole plasmon resonances in gold nanorods," vol. 110, no. 5, pp. 2150–2154.

[94] E. R. Encina and E. A. Coronado, "Plasmonic nanoantennas: Angular scattering properties of multipole resonances in noble metal nanorods," vol. 112, no. 26, pp. 9586–9594.

[95] E.-A. You, W. Zhou, J. Y. Suh, M. D. Huntington, and T. W. Odom, "Polarization-dependent multipolar plasmon resonances in anisotropic multiscale au particles," vol. 6, no. 2, pp. 1786–1794.

[96] J. A. Fan, K. Bao, C. Wu, J. Bao, R. Bardhan, N. J. Halas, V. N. Manoharan, G. Shvets, P. Nordlander, and F. Capasso, "Fano-like interference in self-assembled plasmonic quadrumer clusters," vol. 10, no. 11, pp. 4680–4685.

[97] B. Hopkins, W. Liu, A. E. Miroshnichenko, and Y. S. Kivshar, "Optically isotropic responses induced by discrete rotational symmetry of nanoparticle clusters," vol. 5, no. 14, pp. 6395–6403.

[98] M. Rahmani, E. Yoxall, B. Hopkins, Y. Sonnefraud, Y. Kivshar, M. Hong, C. Phillips, S. A. Maier, and A. E. Miroshnichenko, "Plasmonic nanoclusters with rotational symmetry: polarization-invariant far-field response vs changing near-field distribution," vol. 7, no. 12, pp. 11138–11146.

[99] J. E. Millstone, S. Park, K. L. Shuford, L. Qin, G. C. Schatz, and C. A. Mirkin, "Observation of a quadrupole plasmon mode for a colloidal solution of gold nanoprisms," vol. 127, no. 15, pp. 5312–5313.

[100] M. Rang, A. C. Jones, F. Zhou, Z.-Y. Li, B. J. Wiley, Y. Xia, and M. B. Raschke, "Optical near-field mapping of plasmonic nanoprisms," vol. 8, no. 10, pp. 3357–3363.

[101] P. Chaturvedi, K. H. Hsu, A. Kumar, K. H. Fung, J. C. Mabon, and N. X. Fang, "Imaging of plasmonic modes of silver nanoparticles using high-resolution cathodoluminescence spectroscopy," vol. 3, no. 10, pp. 2965–2974.

[102] T. A. Nieminen, T. Asavei, V. L. Loke, N. R. Heckenberg, and H. Rubinsztein-Dunlop, "Symmetry and the generation and measurement of optical torque," vol. 110, no. 14, pp. 1472–1482.

[103] J. P. Torres and L. Torner, *Twisted Photons: Applications of Light with Orbital Angular Momentum.* Wiley New York.

[104] P. L. Marston and James H. Crichton, "Radiation torque on a sphere caused by a circularly-polarized electromagnetic wave," vol. 30, no. 5, p. 2508.

[105] K. Dholakia, P. Reece, and M. Gu, "Optical micromanipulation," vol. 37, no. 1, pp. 42–55.

[106] R. Agarwal, K. Ladavac, Y. Roichman, G. Yu, C. M. Lieber, and D. G. Grier, "Manipulation and assembly of nanowires with holographic optical traps," vol. 13, no. 22, pp. 8906–8912.

[107] E. Karimi, B. Piccirillo, E. Nagali, L. Marrucci, and E. Santamato, "Efficient generation and sorting of orbital angular momentum eigenmodes of light by thermally tuned q-plates," vol. 94, no. 23, p. 231124.

[108] M. G. Gustafsson, "Surpassing the lateral resolution limit by a factor of two using structured illumination microscopy," vol. 198, no. 2, pp. 82–87.

[109] D. L. Andrews, *Structured light and its applications: An introduction to phase-structured beams and nanoscale optical forces.* Academic Press.

[110] M. Liu, N. Ji, Z. Lin, and S. Chui, "Radiation torque on a birefringent sphere caused by an electromagnetic wave," vol. 72, no. 5, p. 056610.

[111] J. Chen, N. Wang, L. Cui, X. Li, Z. Lin, and J. Ng, "Optical twist induced by plasmonic resonance," vol. 6, p. 27927.

[112] A. Lehmuskero, Y. Li, P. Johansson, and M. Käll, "Plasmonic particles set into fast orbital motion by an optical vortex beam," vol. 22, no. 4, pp. 4349–4356.

[113] W. Singer, S. Bernet, N. Hecker, and M. Ritsch-Marte, "Three-dimensional force calibration of optical tweezers," vol. 47, no. 14, pp. 2921–2931.

[114] A. R. Gersborg and O. Sigmund, "Maximizing opto-mechanical interaction using topology optimization," vol. 87, no. 9, pp. 822–843.

[115] F. Hajizadeh and S. N. S Reihani, "Optimized optical trapping of gold nanoparticles," vol. 18, no. 2, pp. 551–559.

[116] I. M. Tolić-Nørrelykke, K. Berg-Sørensen, and H. Flyvbjerg, "MatLab program for precision calibration of optical tweezers," vol. 159, no. 3, pp. 225–240.

[117] M. Polin, K. Ladavac, S.-H. Lee, Y. Roichman, and D. Grier, "Optimized holographic optical traps," vol. 13, no. 15, pp. 5831–5845.

[118] E. Martín-Badosa, M. Montes-Usategui, A. Carnicer, J. Andilla, E. Pleguezuelos, and I. Juvells, "Design strategies for optimizing holographic optical tweezers set-ups," vol. 9, no. 8, p. S267.

[119] S. Bianchi and R. Di Leonardo, "Real-time optical micro-manipulation using optimized holograms generated on the GPU," vol. 181, no. 8, pp. 1444–1448.

[120] T. Čižmár, O. Brzobohaty, K. Dholakia, and P. Zemánek, "The holographic optical micro-manipulation system based on counter-propagating beams," vol. 8, no. 1, pp. 50–56.

[121] T. T. Tao Tao, J. L. Jing Li, Q. L. Qian Long, and X. W. Xiaoping Wu, "3d trapping and manipulation of micro-particles using holographic optical tweezers with optimized computer-generated holograms," vol. 9, no. 12, pp. 120010–120013.

[122] C. P. Lapointe, T. G. Mason, and I. I. Smalyukh, "Towards total photonic control of complex-shaped colloids by vortex beams," vol. 19, no. 19, pp. 18182–18189.

[123] J. Rosen, B. Salik, and A. Yariv, "Pseudo-nondiffracting beams generated by radial harmonic functions," vol. 12, no. 11, pp. 2446–2457.

[124] K. Volke-Sepulveda, V. Garcés-Chávez, S. Chávez-Cerda, J. Arlt, and K. Dholakia, "Orbital angular momentum of a high-order bessel light beam," vol. 4, no. 2, p. S82.

[125] M. H. Reid and S. G. Johnson, "Efficient computation of power, force, and torque in BEM scattering calculations," vol. 63, no. 8, pp. 3588–3598.

[126] R. E. Hamam, A. Karalis, J. D. Joannopoulos, and M. Soljačić, "Coupled-mode theory for general free-space resonant scattering of waves," vol. 75, no. 5.

[127] D.-H. Kwon and D. M. Pozar, "Optimal characteristics of an arbitrary receive antenna," vol. 57, no. 12, pp. 3720–3727.

[128] I. Liberal, Y. Ra'di, R. Gonzalo, I. Ederra, S. A. Tretyakov, and R. W. Ziolkowski, "Least upper bounds of the powers extracted and scattered by bi-anisotropic particles," vol. 62, no. 9, pp. 4726–4735.

[129] M. Friese, T. Nieminen, N. Heckenberg, and H. Rubinsztein-Dunlop, "Optical torque controlled by elliptical polarization," vol. 23, no. 1, pp. 1–3.

[130] O. D. Miller, A. G. Polimeridis, M. T. Homer Reid, C. W. Hsu, B. G. DeLacy, J. D. Joannopoulos, M. Soljačić, and S. G. Johnson, "Fundamental limits to optical response in absorptive systems," vol. 24, no. 4, pp. 3329–3364.

[131] A. Jesacher, A. Schwaighofer, S. Fürhapter, C. Maurer, S. Bernet, and M. Ritsch-Marte, "Wavefront correction of spatial light modulators using an optical vortex image," vol. 15, no. 9, pp. 5801–5808.

[132] S. Boyd and L. Vandenberghe, *Convex optimization*. Cambridge university press.

[133] A. Mutapcic, S. Boyd, A. Farjadpour, S. G. Johnson, and Y. Avniel, "Robust design of slow-light tapers in periodic waveguides," vol. 41, no. 4, pp. 365–384.

[134] E. Yablonovitch, "Inhibited spontaneous emission in solid-state physics and electronics," vol. 58, no. 20, p. 2059.

[135] S.-y. Lin, J. Fleming, D. Hetherington, B. Smith, R. Biswas, K. Ho, M. Sigalas, W. Zubrzycki, S. Kurtz, and J. Bur, "A three-dimensional photonic crystal operating at infrared wavelengths," vol. 394, no. 6690, pp. 251–253.

[136] J. Fleming, S. Lin, I. El-Kady, R. Biswas, and K. Ho, "All-metallic three-dimensional photonic crystals with a large infrared bandgap," vol. 417, no. 6884, pp. 52–55.

[137] F. O'Sullivan, I. Celanovic, N. Jovanovic, J. Kassakian, S. Akiyama, and K. Wada, "Optical characteristics of one-dimensional si/ si o 2 photonic crystals for thermophotovoltaic applications," vol. 97, no. 3, p. 033529.

[138] M. Ghebrebrhan, P. Bermel, Y. Yeng, I. Celanovic, M. Soljačić, and J. Joannopoulos, "Tailoring thermal emission via q matching of photonic crystal resonances," vol. 83, no. 3, p. 033810.

[139] Y. Shen, D. Ye, I. Celanovic, S. G. Johnson, J. D. Joannopoulos, and M. Soljačić, "Optical broadband angular selectivity," vol. 343, no. 6178, pp. 1499–1501.

[140] T. F. Krauss, R. M. De La Rue, and S. Brand, "Two-dimensional photonic-bandgap structures operating at near-infrared wavelengths," vol. 383, no. 6602, p. 699.

[141] A. Mekis, J. Chen, I. Kurland, S. Fan, P. R. Villeneuve, and J. Joannopoulos, "High transmission through sharp bends in photonic crystal waveguides," vol. 77, no. 18, p. 3787.

[142] S. G. Johnson, S. Fan, P. R. Villeneuve, J. D. Joannopoulos, and L. Kolodziejski, "Guided modes in photonic crystal slabs," vol. 60, no. 8, p. 5751.

[143] S. Fan and J. Joannopoulos, "Analysis of guided resonances in photonic crystal slabs," vol. 65, no. 23, p. 235112.

[144] O. Painter, R. Lee, A. Scherer, A. Yariv, J. O'brien, P. Dapkus, and I. Kim, "Two-dimensional photonic band-gap defect mode laser," vol. 284, no. 5421, pp. 1819–1821.

[145] J. Vučković, M. Lončar, H. Mabuchi, and A. Scherer, "Design of photonic crystal microcavities for cavity QED," vol. 65, no. 1, p. 016608.

[146] D. Englund, D. Fattal, E. Waks, G. Solomon, B. Zhang, T. Nakaoka, Y. Arakawa, Y. Yamamoto, and J. Vučković, "Controlling the spontaneous emission rate of single quantum dots in a two-dimensional photonic crystal," vol. 95, no. 1, p. 013904.

[147] H. Gersen, T. Karle, R. Engelen, W. Bogaerts, J. Korterik, N. Van Hulst, T. Krauss, and L. Kuipers, "Real-space observation of ultraslow light in photonic crystal waveguides," vol. 94, no. 7, p. 073903.

[148] M. F. Yanik and S. Fan, "Stopping light all optically," vol. 92, no. 8, p. 083901.

[149] M. Notomi, K. Yamada, A. Shinya, J. Takahashi, C. Takahashi, and I. Yokohama, "Extremely large group-velocity dispersion of line-defect waveguides in photonic crystal slabs," vol. 87, no. 25, p. 253902.

[150] H. Kosaka, T. Kawashima, A. Tomita, M. Notomi, T. Tamamura, T. Sato, and S. Kawakami, "Superprism phenomena in photonic crystals," vol. 58, no. 16, p. R10096.

[151] [U+FFFD] Notomi, "Theory of light propagation in strongly modulated photonic crystals: Refractionlike behavior in the vicinity of the photonic band gap," vol. 62, no. 16, p. 10696.

[152] M. Lukin and A. Imamoğlu, "Controlling photons using electromagnetically induced transparency," vol. 413, no. 6853, pp. 273–276.

[153] C. E. Kennedy, *Review of mid-to high-temperature solar selective absorber materials*, vol. 1617. National Renewable Energy Laboratory Golden, Colo, USA.

[154] H. Sai, H. Yugami, Y. Kanamori, and K. Hane, "Solar selective absorbers based on two-dimensional w surface gratings with submicron periods for high-temperature photothermal conversion," vol. 79, no. 1, pp. 35–49.

[155] S.-Y. Lin, J. Moreno, and J. Fleming, "Three-dimensional photonic-crystal emitter for thermal photovoltaic power generation," vol. 83, no. 2, pp. 380–382.

[156] T. V. Teperik, F. J. Garcia de Abajo, A. G. Borisov, M. Abdelsalam, P. N. Bartlett, Y. Sugawara, and J. J. Baumberg, "Omnidirectional absorption in nanostructured metal surfaces," vol. 2, no. 5, pp. 299–301.

[157] J. N. Munday and H. A. Atwater, "Large integrated absorption enhancement in plasmonic solar cells by combining metallic gratings and antireflection coatings," vol. 11, no. 6, pp. 2195–2201.

[158] K. Aydin, V. E. Ferry, R. M. Briggs, and H. A. Atwater, "Broadband polarization-independent resonant light absorption using ultrathin plasmonic super absorbers," vol. 2, p. 517.

[159] X. Liu, T. Tyler, T. Starr, A. F. Starr, N. M. Jokerst, and W. J. Padilla, "Taming the blackbody with infrared metamaterials as selective thermal emitters," vol. 107, no. 4, p. 045901.

[160] C. Wu, B. Neuner III, J. John, A. Milder, B. Zollars, S. Savoy, and G. Shvets, "Metamaterial-based integrated plasmonic absorber/emitter for solar thermo-photovoltaic systems," vol. 14, no. 2, p. 024005.

[161] Y. X. Yeng, M. Ghebrebrhan, P. Bermel, W. R. Chan, J. D. Joannopoulos, M. Soljačić, and I. Celanovic, "Enabling high-temperature nanophotonics for energy applications," vol. 109, no. 7, pp. 2280–2285.

[162] Y. Cui, K. H. Fung, J. Xu, H. Ma, Y. Jin, S. He, and N. X. Fang, "Ultrabroadband light absorption by a sawtooth anisotropic metamaterial slab," vol. 12, no. 3, pp. 1443–1447.

[163] C. M. Watts, X. Liu, and W. J. Padilla, "Metamaterial electromagnetic wave absorbers," vol. 24, no. 23.

[164] K. A. Arpin, M. D. Losego, A. N. Cloud, H. Ning, J. Mallek, N. P. Sergeant, L. Zhu, Z. Yu, B. Kalanyan, and G. N. Parsons, "Three-dimensional self-assembled photonic crystals with high temperature stability for thermal emission modification," vol. 4.

[165] V. Rinnerbauer, S. Ndao, Y. X. Yeng, W. R. Chan, J. J. Senkevich, J. D. Joannopoulos, M. Soljačić, and I. Celanovic, "Recent developments in high-temperature photonic crystals for energy conversion," vol. 5, no. 10, p. 8815.

[166] V. Rinnerbauer, S. Ndao, Y. Xiang Yeng, J. J. Senkevich, K. F. Jensen, J. D. Joannopoulos, M. Soljačić, I. Celanovic, and R. D. Geil, "Large-area fabrication of high aspect ratio tantalum photonic crystals for high-temperature selective emitters," vol. 31, no. 1, p. 011802.

[167] J. B. Chou, Y. X. Yeng, A. Lenert, V. Rinnerbauer, I. Celanovic, M. Soljačić, E. N. Wang, and S.-G. Kim, "Design of wide-angle selective absorbers/emitters with dielectric filled metallic photonic crystals for energy applications," vol. 22, no. 101, pp. A144–A154.

[168] J. B. Chou, Y. X. Yeng, Y. E. Lee, A. Lenert, V. Rinnerbauer, I. Celanovic, M. Soljačić, N. X. Fang, E. N. Wang, and S.-G. Kim, "Enabling ideal selective solar absorption with 2d metallic dielectric photonic crystals," vol. 26, no. 47, pp. 8041–8045.

[169] H.-J. Lee, K. Smyth, S. Bathurst, J. Chou, M. Ghebrebrhan, J. Joannopoulos, N. Saka, and S.-G. Kim, "Hafnia-plugged microcavities for thermal stability of selective emitters," vol. 102, no. 24, p. 241904.

[170] J. B. Chou and S.-G. Kim, "Metallic dielectric photonic crystals and methods of fabrication," Dec 2016.

[171] A. Lenert, D. M. Bierman, Y. Nam, W. R. Chan, I. Celanović, M. Soljačić, and E. N. Wang, "A nanophotonic solar thermophotovoltaic device," vol. 9, no. 2, pp. 126–130.

[172] T. J. Seok, A. Jamshidi, M. Eggleston, and M. C. Wu, "Mass-producible and efficient optical antennas with CMOS-fabricated nanometer-scale gap," vol. 21, no. 14, pp. 16561–16569.

[173] X. Liu, X. Deng, P. Sciortino, M. Buonanno, F. Walters, R. Varghese, J. Bacon, L. Chen, N. O'Brie, and J. J. Wang, "Large area, 38 nm half-pitch grating fabrication by using atomic spacer lithography from aluminum wire grids," vol. 6, no. 12, pp. 2723–2727.

[174] Y.-K. Choi, T.-J. King, and C. Hu, "A spacer patterning technology for nanoscale CMOS," vol. 49, no. 3, pp. 436–441.

[175] Y. Wang, "Study on the photoelectric hot electrons generation and transport with metallic-semiconductor photonic crystals," phdthesis.

[176] J. B. Chou, X.-H. Li, Y. Wang, D. P. Fenning, A. Elfaer, J. Viegas, M. Jouiad, Y. Shao-Horn, and S.-G. Kim, "Surface plasmon assisted hot electron collection in wafer-scale metallic-semiconductor photonic crystals," vol. 24, no. 18, pp. A1234–A1244.

[177] X.-H. Li, J. B. Chou, W. L. Kwan, A. M. Elsharif, and S.-G. Kim, "Effect of anisotropic electron momentum distribution of surface plasmon on internal photoemission of a schottky hot carrier device," vol. 25, no. 8, pp. A264–A273.

[178] D. Chanda, K. Shigeta, T. Truong, E. Lui, A. Mihi, M. Schulmerich, P. V. Braun, R. Bhargava, and J. A. Rogers, "Coupling of plasmonic and optical cavity modes in quasi-three-dimensional plasmonic crystals," vol. 2, p. 479.

[179] K. Park, "The extreme values of reflectivity and the conditions for zero reflection from thin dielectric films on metal," vol. 3, no. 7, pp. 877–881.

[180] M. Sigalas and E. N. Economou, "Band structure of elastic waves in two dimensional systems," vol. 86, no. 3, pp. 141–143.

[181] M. S. Kushwaha, P. Halevi, L. Dobrzynski, and B. Djafari-Rouhani, "Acoustic band structure of periodic elastic composites," vol. 71, no. 13, p. 2022.

[182] Y. Pennec, J. O. Vasseur, B. Djafari-Rouhani, L. Dobrzyński, and P. A. Deymier, "Two-dimensional phononic crystals: Examples and applications," vol. 65, no. 8, pp. 229–291.

[183] P. A. Deymier, "Introduction to phononic crystals and acoustic metamaterials," in *Acoustic metamaterials and phononic crystals*, pp. 1–12, Springer.

[184] M. Maldovan, "Sound and heat revolutions in phononics," vol. 503, no. 7475, pp. 209–217.

[185] M. I. Hussein, M. J. Leamy, and M. Ruzzene, "Dynamics of phononic materials and structures: Historical origins, recent progress, and future outlook," vol. 66, no. 4, p. 040802.

[186] R. Martinezsala, J. Sancho, J. V. Sánchez, V. Gómez, J. Llinares, F. Meseguer, and others, "Sound-attenuation by sculpture," vol. 378, no. 6554, pp. 241–241.

[187] J. Sánchez-Pérez, D. Caballero, R. Martinez-Sala, C. Rubio, J. Sánchez-Dehesa, F. Meseguer, J. Llinares, and F. Gálvez, "Sound attenuation by a two-dimensional array of rigid cylinders," vol. 80, no. 24, p. 5325.

[188] Z. Liu, X. Zhang, Y. Mao, Y. Zhu, Z. Yang, C. T. Chan, and P. Sheng, "Locally resonant sonic materials," vol. 289, no. 5485, pp. 1734–1736.

[189] Y. Pennec, B. D. Rouhani, H. Larabi, A. Akjouj, J. Gillet, J. Vasseur, and G. Thabet, "Phonon transport and waveguiding in a phononic crystal made up of cylindrical dots on a thin homogeneous plate," vol. 80, no. 14, p. 144302.

[190] M. Aspelmeyer, T. J. Kippenberg, and F. Marquardt, "Cavity optomechanics," vol. 86, no. 4, p. 1391.

[191] Y. Wu, Y. Lai, and Z.-Q. Zhang, "Effective medium theory for elastic metamaterials in two dimensions," vol. 76, no. 20, p. 205313.

[192] T. Geng, S. Zhuang, J. Gao, and X. Yang, "Nonlocal effective medium approximation for metallic nanorod metamaterials," vol. 91, no. 24, p. 245128.

[193] N. Nemati, A. Kumar, D. Lafarge, and N. X. Fang, "Nonlocal description of sound propagation through an array of helmholtz resonators," vol. 343, no. 12, pp. 656–669.

[194] D. Lafarge, P. Lemarinier, J. F. Allard, and V. Tarnow, "Dynamic compressibility of air in porous structures at audible frequencies," vol. 102, no. 4, pp. 1995–2006.

[195] L. D. Landau, E. M. Lífshíts, and L. Pitaevskii, *Electrodynamics of continuous media*, vol. 8. Pergamon press Oxford.

[196] V. M. Agranovich, V. L. Ginzburg, and V. L. Ginzburg, *Spatial dispersion in crystal optics and the theory of excitons.* Interscience New York, 1966.

[197] C. Boutin and F. X. Becot, "Theory and experiments on poro-acoustics with inner resonators," vol. 54, pp. 76–99.

[198] N. Nemati and D. Lafarge, "Check on a nonlocal maxwellian theory of sound propagation in fluid-saturated rigid-framed porous media," vol. 51, no. 5, pp. 716–728.

[199] G. W. Milton and J. R. Willis, "On modifications of newton's second law and linear continuum elastodynamics," in *Proceedings of the Royal Society of London A: Mathematical, Physical and Engineering Sciences*, vol. 463, pp. 855–880, The Royal Society.

[200] S. Nemat-Nasser and A. Srivastava, "Overall dynamic constitutive relations of layered elastic composites," vol. 59, no. 10, pp. 1953–1965.

[201] D. Torrent, Y. Pennec, and B. Djafari-Rouhani, "Resonant and nonlocal properties of phononic metasolids," vol. 92, no. 17, p. 174110.

[202] A. Srivastava and S. Nemat-Nasser, "Overall dynamic properties of three-dimensional periodic elastic composites," in *Proc. R. Soc. A*, vol. 468, pp. 269–287, The Royal Society.

[203] I. Prigogine, "Introduction to thermodynamics of irreversible processes,"

[204] S. R. De Groot and P. Mazur, *Non-equilibrium thermodynamics.* Courier Corporation.

[205] H. A. Lorentz, "The fundamental equations for electromagnetic phenomena in ponderable bodies deduced from the theory of electrons," vol. 5, pp. 254–266.

[206] D. L. Johnson, J. Koplik, and R. Dashen, "Theory of dynamic permeability and tortuosity in fluid-saturated porous media," vol. 176, pp. 379–402.

[207] M. Avellaneda and S. Torquato, "Rigorous link between fluid permeability, electrical conductivity, and relaxation times for transport in porous media," vol. 3, no. 11, pp. 2529–2540.

[208] C. Boutin and C. Geindreau, "Estimates and bounds of dynamic permeability of granular media," vol. 124, no. 6, pp. 3576–3593.

[209] R. Burridge and J. B. Keller, "Poroelasticity equations derived from microstructure," vol. 70, no. 4, pp. 1140–1146.

[210] M.-Y. Zhou and P. Sheng, "First-principles calculations of dynamic permeability in porous media," vol. 39, no. 16, p. 12027.

[211] E. Polizzi, "A high-performance numerical library for solving eigenvalue problems: FEAST solver v2. 1 user's guide,"

[212] J. Asakura, T. Sakurai, H. Tadano, T. Ikegami, and K. Kimura, "A numerical method for nonlinear eigenvalue problems using contour integrals," vol. 1, no. 0, pp. 52–55.

[213] W.-J. Beyn, "An integral method for solving nonlinear eigenvalue problems," vol. 436, no. 10, pp. 3839–3863.

[214] T. Sakurai, Y. Futamura, and H. Tadano, "Efficient parameter estimation and implementation of a contour integral-based eigensolver," vol. 7, no. 3, pp. 249–270.

[215] H. Gao, T. Matsumoto, T. Takahashi, and H. Isakari, "Eigenvalue analysis for acoustic problem in 3d by boundary element method with the block sakurai–sugiura method," vol. 37, no. 6, pp. 914–923.

[216] T. J. Ypma, "Historical development of the newton–raphson method," vol. 37, no. 4, pp. 531–551.

[217] R. D. Doolittle, H. Überall, and P. Uginčius, "Sound scattering by elastic cylinders," vol. 43, no. 1, pp. 1–14.

[218] C. M. Bender and S. A. Orszag, *Advanced mathematical methods for scientists and engineers I: Asymptotic methods and perturbation theory.* Springer Science & Business Media.

[219] J. Allard and N. Atalla, *Propagation of sound in porous media: modelling sound absorbing materials 2e.* John Wiley & Sons.

[220] P. K. Jain, D. Ghosh, R. Baer, E. Rabani, and A. P. Alivisatos, "Near-field manipulation of spectroscopic selection rules on the nanoscale," vol. 109, no. 21, pp. 8016–8019.

[221] G. J. Gbur, *Mathematical methods for optical physics and engineering.* Cambridge University Press.

[222] A. Duclos, D. Lafarge, and V. Pagneux, "Transmission of acoustic waves through 2d phononic crystal: visco-thermal and multiple scattering effects," vol. 45, no. 1, p. 11302.

[223] Y.-Y. Chen and Z. Ye, "Acoustic attenuation by two-dimensional arrays of rigid cylinders," vol. 87, no. 18, p. 184301.